Univerza
v Ljubljani
Fakulteta
za gradbeništvo
in geodezijo

STEFANO CAPRINOZZI

POTRESNI ODZIV JEKLENIH REZERVOARJEV S PLAVAJOČIMI STREHAMI

DOKTORSKA DISERTACIJA

SEISMIC RESPONSE OF STEEL TANKS WITH FLOATING ROOFS

DOCTORAL DISSERTATION

INTERDISCIPLINARNI DOKTORSKI ŠTUDIJSKI PROGRAM
GRAJENO OKOLJE

Ljubljana, 2021

Univerza
v Ljubljani
Fakulteta
za gradbeništvo
in geodezijo

Doktorand
STEFANO CAPRINOZZI

POTRESNI ODZIV JEKLENIH REZERVOARJEV S PLAVAJOČIMI STREHAMI

Doktorska disertacija

SEISMIC RESPONSE OF STEEL TANKS WITH FLOATING ROOFS

Doctoral dissertation

Ljubljana, julij 2021

Univerza
v Ljubljani
Fakulteta
za gradbeništvo
in geodezijo

Mentor: prof. Matjaž Dolšek, UL FGG.

Somentor: izr. prof. dr. Fabrizio Paolacci, UNIROMA3.

Komisija za spremljanje doktorskega študenta/-tke:

prof. dr. Boštjan Brank, UL FGG,

izr. prof. dr. Primož Može, UL FGG,

doc. dr. Iztok Peruš, UM FGPA.

Podpisani študent Stefano Caprinozzi, vpisna številka 26700234, avtor pisnega zaključnega dela študija z naslovom: Potresni odziv jeklenih rezervoarjev s plavajočimi strehami

IZJAVLJAM

1. *Obkrožite eno od variant a) ali b)*

   a) da je pisno zaključno delo študija rezultat mojega samostojnega dela;

   b) da je pisno zaključno delo študija rezultat lastnega dela več kandidatov in izpolnjuje pogoje, ki jih Statut UL določa za skupna zaključna dela študija ter je v zahtevanem deležu rezultat mojega samostojnega dela;

2. da je tiskana oblika pisnega zaključnega dela študija istovetna elektronski obliki pisnega zaključnega dela študija;

3. da sem pridobil/-a vsa potrebna dovoljenja za uporabo podatkov in avtorskih del v pisnem zaključnem delu študija in jih v pisnem zaključnem delu študija jasno označil/-a;

4. da sem pri pripravi pisnega zaključnega dela študija ravnal/-a v skladu z etičnimi načeli in, kjer je to potrebno, za raziskavo pridobil/-a soglasje etične komisije;

5. soglašam, da se elektronska oblika pisnega zaključnega dela študija uporabi za preverjanje podobnosti vsebine z drugimi deli s programsko opremo za preverjanje podobnosti vsebine, ki je povezana s študijskim informacijskim sistemom članice;

6. da na UL neodplačno, neizključno, prostorsko in časovno neomejeno prenašam pravico shranitve avtorskega dela v elektronski obliki, pravico reproduciranja ter pravico dajanja pisnega zaključnega dela študija na voljo javnosti na svetovnem spletu preko Repozitorija UL;

7. [za zaključna dela na 3. stopnji študija, sestavljena iz člankov] da sem od založnikov, na katere sem predhodno izključno prenesel/-la materialne avtorske pravice na člankih, pridobil/-a potrebna soglasja za vključitev člankov v tiskano in elektronsko obliko disertacije. Soglasja UL omogočajo neodplačno, neizključno, prostorsko in časovno neomejeno hranjenje avtorskega dela v elektronski obliki in reproduciranje ter dajanje disertacije na voljo javnosti na svetovnem spletu preko Repozitorija UL;

8. da dovoljujem objavo svojih osebnih podatkov, ki so navedeni v pisnem zaključnem delu študija in tej izjavi, skupaj z objavo pisnega zaključnega dela študija.

V Ljubljani, 12.7.2021

Podpis študenta:

ERRATA

Page	Line	Error	Correction

ACKNOWLEDGEMENTS

Words are not enough to properly describe what these past three years abroad mean to me. During this incredible journey, I met people who largely enriched me from a human and scientific point of view. Thank you Professor Matjaž Dolšek, for the precious advices and your support provided during my doctoral studies. You did not simply teach me the principles of research, but you stimulated in me critical thinking in order to let me better understand and improve my knowledge: this is the most precious value that a teacher should have. Special greetings also go to Professor Fabrizio Paolacci, who helped me with discovering new technical and scientific aspects, which improved my knowledge. A thought also goes to my valuable colleagues at Fakulteta za Gradbeništvo in Geodezijo (FGG). Mirko, Jure, Anže, Aleš and Nuša, everything could have been much more challenging without you. Thanks to the VCE (Vienna) for hosting me during my secondment. You showed me different valuable realities. Many thanks to all the early-stage researchers (ESRs), which ensured a lot of happy times across Europe. Furthermore, thanks to Marie Skłodowska-Curie Actions (MSCA), which allowed me establishing a high-skilled network and, most important several never-ending international friendships. Thanks also to the Italian community in Ljubljana, which delighted my staying in the country. You are too much to be listed. However, you'll never be forgotten. Thanks to all the people that have been with me and mostly to those who haven't because they let me appreciate more who preferred to remain instead of leave.

Thank you Francesca for sharing with me this adventure. You are too important to be included in the previous text, you deserve your part in the Thesis as you had in the time we spent together.

Finally, thanks to my family for being beside me even if hundreds of kilometres away. You were there, you are here, and you'll be everywhere with me.

BIBLIOGRAFSKO – DOKUMENTACIJSKA STRAN IN IZVLEČEK

UDK:	**624.014.2:624.953:624.042.7(043)**
Avtor:	**Stefano Caprinozzi**
Mentor:	**prof. Matjaž Dolšek, Ph. D.**
Somentor:	**izr. prof. Fabrizio Paolacci, Ph. D.**
Naslov:	**Potresni odziv jeklenih rezervoarjev s plavajočimi strehami**
Tip dokumenta:	**Doktorska disertacija**
Obseg in oprema:	**-**
Ključne besede:	**jekleni rezervoarji, petrokemična tovarna, analiza potresne ranljivosti, analiza tveganja, odločitveni model, naravno-tehnološki dogodki, plavajoča streha, potresna miza, poenostavljen model, model s končnimi elementi**

Izvleček

Nedavni močni potresi so razkrili, da jekleni rezervoarji za tekočino niso imuni na naravno-tehnološke nezgode. Glaven problem predstavlja potencialno uhajanje nevarnih snovi iz rezervoarjev, kar je bil predmet raziskav, predstavljenih v doktorski disertaciji. Najprej je preučevana zmogljivost poenostavljenega modela dvignjenega rezervoarja, ki ni skladen s standardom in se je porušili med potresom v Kocaeliju. Na primeru tega rezervoarja in različice, ki je skladna s trenutno veljavnim standardom, so nato preverjene tri mere potresne zmogljivosti. Potresno tveganje se izkaže za bolj celovito mero potresne zmogljivosti, vendar je računsko zahtevna mera, medtem ko je konvencionalna mera potresne zmogljivosti dobro uveljavljena, vendar lahko vodi do pristranskega odločanja. Ta ugotovitev je narekovala razvoj računsko učinkovitega poenostavljenega modela prostostoječega rezervoarja s plavajočo streho, ki je bil preverjen s poudarkom na simulaciji prelivanja tekočine preko stene rezervoarja. Za preverjanje poenostavljenega modela so uporabljeni eksperimentalni rezultati na potresni mizi in rezultati simulacij na osnovi podrobnega modela s končnimi elementi. Zmogljivost poenostavljenega modela za analize tveganja se nato demonstrira s potresno analizo ranljivost in tveganja prostostoječega širokega rezervoarja s plavajočo streho. Ugotovljeno je bilo, da je tveganje za prelivanje tekočine visoko, medtem ko je bilo tveganje za izlitje tekočine zaradi okvare stene rezervoarja približno en velikostni red nižje. Uvedena metodologija za oceno potresnega tveganja upošteva letno spremembo stopnje polnjenja rezervoarja in je tudi učinkovito orodje za obvladovanje tveganja za izgube zadrževanja tekočine, če se uporabi za določitev sprejemljive stopnje napolnjenosti rezervoarjev ob upoštevanju ciljnega tveganja.

BIBLIOGRAPHIC – DOCUMENTALISTIC INFORMATION AND ABSTRACT

UDC:	**624.014.2:624.953:624.042.7(043)**
Author:	**Stefano Caprinozzi**
Supervisor:	**Prof. Matjaž Dolšek, Ph. D.**
Co-supervisor:	**Assoc. Prof. Fabrizio Paolacci, Ph. D.**
Title:	**Seismic response of steel tanks with floating roofs**
Document type:	**Doctoral Dissertation**
Notes:	**-**
Keywords:	**Steel storage tanks, Petrochemical plant, Seismic fragility analysis, Risk analysis, Decision models, Natech event, Floating roof, Shaking table test, Simplified model, Finite element model**

Abstract

Recent major earthquakes revealed that liquid steel storage tanks are not immune to Natech accidents. The main issue is the potential leakage of hazardous material from the storage tank, which was also the subject of research presented in the thesis. Firstly, the capability of the tank simplified model is investigated by means of a non-code-conforming elevated tank that collapsed during the Kocaeli earthquake. Then three available seismic performance metrics are applied to the non-code-conforming elevated tank and its code-conforming variant. The risk-based performance metric is found comprehensive but computationally demanding, while the conventional performance metric is well established, but it may lead to biased decision-making. This finding implied the development of a computationally efficient simplified model of the unanchored liquid storage tank with a floating roof. The developed simplified model is validated by focusing on simulating liquid overtopping observed from the shaking table test results and refined finite element model. The capability of the simplified model is then demonstrated by means of the seismic fragility and risk analysis of the unanchored broad storage tank with a floating roof. The risk for liquid overtopping is observed high, while the risk for leakage due to tank wall failure is about one magnitude lower. The introduced methodology for seismic risk assessment also accounts for the annual variation of the tank's filling level. It is an efficient tool for loss-of-containment risk management if applied for determination of the risk-based tolerable tank's filling level of the storage tanks.

TABLE OF CONTENT

LIST OF FIGURES

LIST OF TABLES

Abbreviations

ALE arbitrary Lagrangian-Eulerian
C capacity
CC consequence class
CF coefficient function
CS conditional spectrum
D demand
DCH ductility class high
EDP engineer demand parameter
EFB elephant's foot buckling
EOS equation of state
ESF equation solver function
FE finite element
GM ground motion
GMPE ground motion prediction equation
IDA incremental dynamic analysis
IM seismic intensity measure
LOC loss of containment
LS limit state
LUF lowest usable frequency
MCE maximum credible earthquake
MCE_G maximum credible earthquake without adjustments to target risk
MCE_R maximum credible earthquake with adjustment to target collapse risk
MF matrix function
MSA multiple stripes analysis
Natech natural-technological
NC near collapse
PGA peak ground acceleration
RF run function
RN reference node
SSA single stripe analysis
UHS uniform hazard spectrum
USD United States Dollars
3D three dimensions

Symbols

$\boldsymbol{\beta}$ standard deviation of the natural logarithms of the IM which causes the exceedance of the LS

γ aspect ratio

γ_{cr} shear deformation for the first crack

γ_I importance factor

γ_u shear deformation corresponding to the 80% drop of the maximum shear force

γ_y shear deformation corresponding to the maximum shear force

$\boldsymbol{\epsilon_i}$ *i-th* root of the first derivative of the Bessel function of the first kind of order one

$\boldsymbol{\varepsilon_{rr}}$ radial strain tensor components of the floating roof deck in polar coordinates

$\boldsymbol{\varepsilon_{\theta\theta}}$ angular strain tensor components of the floating roof deck in polar coordinates

$\boldsymbol{\varepsilon_{r\theta}}$ deviatoric strain tensor components of the floating roof deck in polar coordinates

ζ damping ratio

$\boldsymbol{\lambda}$ rate of exceedance of the selected limit state

$\boldsymbol{\lambda_{j,p}}$ frequency parameter

$\boldsymbol{\mu_F}$ friction coefficient

$\boldsymbol{\mu_V}$ dynamic viscosity

$\boldsymbol{\mu}$ is the median value of the IM that causes the exceedance of LS

$\boldsymbol{\nu}$ Poisson's ratio

$\boldsymbol{\xi_i}$ is the *i-th* interpolation function

$\boldsymbol{\rho}$ fluid density

$\boldsymbol{\rho_r}$ density of floating roof material

$\boldsymbol{\sigma_{rr}}$ radial stress tensor components of the floating roof deck in polar coordinates

$\boldsymbol{\sigma_{\theta\theta}}$ angular stress tensor components of the floating roof deck in polar coordinates

$\boldsymbol{\sigma_{r\theta}}$ deviatoric stress tensor components of the floating roof deck in polar coordinates

$\boldsymbol{\sigma_c}$ calculated compressive stress

$\boldsymbol{\varphi}$ combination coefficient

$\boldsymbol{\Gamma_0}$ the Grüneisen ratio of the material

$\boldsymbol{\theta}$ angular polar coordinate

$\boldsymbol{\phi}$ potential function of the fluid

$\mathbf{a_{g,R}}$ design PGA

$\boldsymbol{dt}$ ground motion acceleration history time-sampling interval

$\boldsymbol{g}$ gravity acceleration

$\boldsymbol{h}$ floating roof thickness

$\boldsymbol{h_c}$ convective mass height

$\boldsymbol{h_e}$ wave height

$\boldsymbol{h_e}$ equivalent thickness of the floating

$\boldsymbol{h_i}$ impulsive mass height

$\boldsymbol{im}$ value of random variable

$\boldsymbol{j}$ nodal circumference number

$\boldsymbol{k}$ slope of the linear approximation of the hazard function in the log-domain

$\boldsymbol{k_0}$ intercept slope of the linear approximation of the hazard function in the log-domain

$\boldsymbol{k_i}$ stiffness corresponding to the impulsive mass

$\boldsymbol{k_c}$ stiffness corresponding to the convective mass

$\mathbf{m}$ mass

$\boldsymbol{m_c}$ convective mass

$\boldsymbol{m_i}$ impulsive mass

$\boldsymbol{n_{GM}}$ total number of the selected ground motions

$\boldsymbol{n_j}$ is the number of ground motions at intensity *j*

$\boldsymbol{n_{LS}}$ ground motions that cause the exceedance of the LS

$\boldsymbol{p}$ nodal diameter number

$\boldsymbol{r}$ radial polar coordinate

$\boldsymbol{s}$ the slope of the EOS curve

$\boldsymbol{t}$ thickness of the shell ring under consideration

$\boldsymbol{t_s}$ thickness of bottom shell course

$\boldsymbol{w}$ vertical floating roof displacement

$\boldsymbol{w_a}$ uplifting force in annular region

$\boldsymbol{w_{int}}$ calculated design uplift load due to product pressure per unit of circumferential length

$\boldsymbol{w_t}$ tank and roof weight per unit of circumferential length

$\boldsymbol{x_j}$ is the seismic intensity at stripe *j*

$\boldsymbol{\dot{x}_g}$ ground velocity due to the ground motion

$\ddot{\boldsymbol{x}}_{\boldsymbol{g}}$ ground motion acceleration history
$\boldsymbol{z}$ vertical coordinate for the fluid
z_j is the number of ground motions exceeding LS at stripe j, and

$\boldsymbol{A_i}$ *i-th* considered filling level
$\boldsymbol{A_i(t)}$ time-dependent modal amplitude
$\boldsymbol{A_v}$ vertical earthquake acceleration
$\boldsymbol{B_i(t)}$ time-dependent coefficient
$\boldsymbol{C_0}$ the reference speed of sound in the medium
D tank diameter
$\boldsymbol{D_{j,p}}$ amplitude parameter
E Young's modulus
$\boldsymbol{E_{j,p}}$ mode shape parameter
F fluid Lagrangian
$\boldsymbol{F_c}$ limit compressive stress
$\boldsymbol{F_y}$ minimum specified yield strength of bottom annulus
G specific gravity
$\boldsymbol{H_t}$ tank height
H fluid height
H(im) hazard function of the site of interest
I number of considered interpolation functions
J anchorage ratio
$\boldsymbol{J_1}$ Bessel function of the first kind of order one
M magnitude
$\boldsymbol{M_{rw}}$ overturning moment of the steel storage tank
$\boldsymbol{P_{fi}}$ represents the annual rate of exceeding the LS of i-th considered filling level
$\boldsymbol{P_{f,IM,LS}}$ probability of exceeding a limit state for a given seismic intensity level
$\boldsymbol{P_{f,LS}}$ probability of exceeding a limit state for a given period of one year
Pos angular coordinate ranging from 0 to 2π
R source-to-site distance
R tank's radius
$\boldsymbol{R_f}$ roof floating roof flexural stiffness
RPos radial coordinate from 0 to floating roof radius R
$\boldsymbol{S_a}$ spectral acceleration
$\boldsymbol{S_v}$ floating roof surface
T kinetic energy of the floating roof
$\boldsymbol{T_c}$ convective period
$\boldsymbol{T_i}$ impulsive period
$\boldsymbol{T_{NCR}}$ near-collapse (mean) return period
U strain energy of the floating roof

1 INTRODUCTION

Liquid storage tanks are essential units of industrial plants, which provide vital services for the everyday functionality of cities and communities. However, their response to rare natural events is not yet well understood, and thus its safety is still questionable. It was realized that floating roofs of storage tanks do not prevent the leakage of hazardous material during major seismic events, which can trigger fire, explosion, toxic dispersion and other adverse effects on the built environment. It is thus necessary to investigate the behaviour of storage tanks with floating roofs, which is the main objective of the proposed research.

In the first part of the research, conventional and risk-based performance metrics was investigated to get an insight into the decision-making about the seismic safety of liquid storage tanks. This was followed by studying the seismic behaviour of steel liquid storage tanks with floating roofs. A refined finite element model (FE) was developed using finite element analysis software (e.g. Abaqus). In addition, a simplified model for the seismic response of a floating roof of liquid storage was also introduced. Both models were then, to some extend, validated by results of shake table tests performed within the project INDUSE-2-SAFETY (CEA, 2017). In the second part of the thesis, seismic fragility and risk analysis of the floating roof of steel storage tanks are examined by utilizing the simplified model with the emphasis on evaluating seismic safety against loss of content due to failures of the floating roof.

1.1 Motivation and description of the problem

Industrial facilities are extremely important for providing the functionality of the built environment and societal well-being, but some recent earthquakes, tsunamis and floods triggered so-called natural-technological (Natech) events, highlighted the vulnerability of industrial facilities (Lanzano et al., 2015). Furthermore, the increased environmental attention and the uncertainties related to future economic losses generated demand for research and development aimed at improving the knowledge regarding the performance of complex industrial systems. However, special attention should be devoted to infrequent events, such as major earthquakes, for which the stakeholders cannot develop perception based on experiences. In such cases, the risk and resilience metrics can be used for establishing an appropriate perception of stakeholders.

Concerning industrial facilities and tank farms in which a large number of hazardous substances are present, many severe accidents were reported as a consequence of seismic events (Lindell & Perry, 1996; Young et al., 2004). Industrial accidents caused by seismic events may trigger additional adverse events such as blast waves, toxic releases, fire radiation, hazardous content spilling or leakages. Therefore, it is necessary to predict the seismic behaviour of industrial plant units better. The improved knowledge about the seismic performance of industrial plants will contribute to the improvement of risk evaluation, which is of fundamental concern to be addressed (Antonioni et al., 2007) for well-informed decision making. The liquid storage tanks are certainly not immune to Natech events but represent a crucial component of modern petrochemical plants. The most problematic is that these particular components of petrochemical plants are usually filled with hazardous liquids. Therefore, the leakage of the content must be prevented with high reliability to avoid environmental disasters, human injuries and to ensure a reasonable level of resilience of the built environment.

In the past adverse events, it was observed that the most common failures of steel storage tanks are related to the tank wall (i.e. elephant's foot buckling or diamond-shaped buckling), the potential anchorages and the supporting structure, and the failure of a floating roof (Hatayama et al., 2004). Those phenomena of storage tanks have been investigated with many different types of models (Malhotra & Veletsos, 1994; Malhotra, 1995; Malhotra et al., 2000; Bakalis et al., 2017). However, only a few studies include consideration of the effect of a roof, mostly a fixed roof (Fan et al., 2018; Kummari et al., 2018; Taniguchi et al., 2018). Nevertheless, roofs are in most cases not fixed to the tank, which means that during strong ground motion, the sloshing of the liquid surface interacts with the bottom surface of the floating roof, causing vertical displacement, which is not uniformly distributed all over the roof surface. The nonlinear effect of the roof itself or large relative displacement between the roof edge and the tank wall may also occur. Consideration of the second-order effect may enable investigations of loss of sealing of a floating roof. This can be the major cause of the leakage of the tank's content (Shabani & Golzar, 2012). In this respect, appropriate tools capable of quantifying the dynamic interaction between these two surfaces are needed because only a few studies addressed this issue (Matsui, 2007; Matsui, 2017). However, the detailed structural analysis based on the use of refined finite element calculations is computationally demanding even for the building structures (Fabbrocino et al., 2005). The computational complexity in the case of liquid storage tanks increases significantly if such complex simulations are applied to a tank farm of an oil refinery, for which the consideration of domino effects may not be negligible. The simulation of the seismic response of tank farm becomes even more complex when it is applied for seismic risk assessment, which requires numerous simulations for different levels of seismic actions represented by a hazard-consistent set of ground motions (Corritore et al., 2017). Therefore, new simplified models of liquid storage tanks, which can be easily used in risk studies, have to be developed.

In addition to appropriate models, it is necessary to develop decision models and performance objectives that will allow for well-informed decision-making about the seismic safety of structures. The conventional performance metric is based on the estimation of demand and capacity. The demand usually corresponds to a design earthquake (CEN, 2004) associated with a given mean annual return period. The effects of all other possible earthquakes, which can occur at the site of the infrastructure during its lifetime, are therefore neglected in the design. For instance, (Vathi et al., 2017) used such performance metrics for the evaluation of the seismic performance of liquid storage tanks. In the report about the Izmit earthquake, Sezen & Whittaker (2006) evaluated the seismic performance of the investigated facilities using the conventional approach. However, more general decision models for the evaluation of seismic safety account for the risk-based metrics. One possibility is to define the performance objective by the acceptable probability of exceedance of a designated limit state (LS) given a defined seismic scenario. Another option is to determine an acceptable probability of exceedance of a designated limit state for a given period as proposed in the new draft of EC 8-1 (CEN, 2019) and ANS 2.26 (American Nuclear Society et al., 2004). A similar approach was used for the risk-based design of building structures by (Lazar Sinković et al., 2016). However, the risk-based performance metrics imply seismic fragility analysis of the examined structure, which is already often used to assess the seismic performance of such units (Salzano et al., 2003; Phan et al., 2016).

The above-descrived issues were investigated gradually. Firstly, the seismic behaviour of the liquid storage tanks using conventional and risk-based performance metrics was examined. A study involves an existing elevated storage tank, which was damaged during the Izmit earthquake and its variant of the code-conforming tank. It provides insight into the decision-making about the seismic safety of storage tanks when evaluated by the conventional and risk-based performance metrics. Simplified models of tanks were used at this stage of the research, while the effect of a floating roof was neglected. The objective of the next stage of the research was to investigate the seismic behaviour of liquid storage tanks with floating roofs. For this purpose, refined finite element models and simplified numerical models were developed and validated by experimental shaking table tests, which were performed in past projects (CEA, 2017). Finally, the simplified models of liquid storage tanks with consideration of the effects of floating roofs were used to investigate the seismic safety of such tanks by fragility and risk analysis.

1.2 Literature review

Steel storage tanks are commonly used in the oil/gas and chemical industries to store a wide variety of liquids such as oil, gasoline, diesel, ammonia or other hazardous material. In general, storage tanks are very susceptible to damage caused by earthquakes due to their flexibility and sloshing effects of the contained liquid (Razzaghi & Eshghi, 2004). Numerous liquid storage tanks have been severely damaged during major earthquakes (Manos & Clough, 1985; NIST, 1995). Several failure modes may occur due to the floating roof, leading to the loss of containment. Floating roofs are installed mainly to reduce the evaporative loss of the stored content and, consequently, to reduce the probability of vapour cloud generation (El-Samanody et al., 2016).

Several types of floating roofs are available on the market. They can be classified into different groups depending on the floating roofs' position within the tank and the construction approaches adopted for the floating roof itself. Indeed, the floating roofs can be defined as either external or internal, whereas the floating roof is used on a free-top steel storage tank or in a tank equipped with a fixed roof. In the latter case, the floating roof is installed in closed tank. Depending on the adopted construction approach, the following types of roofs can be distinguished (Figure 1):

- single deck with supporting trusses and no pontoon (Figure 1 (a));
- single deck with annular pontoon (Figure 1 (b));
- single deck with annular and central pontoon (Figure 1 (c));
- single deck with annular pontoon and inner pontoons (Figure 1 (d));
- double deck with reinforcing structures in between (Figure 1 (e)).

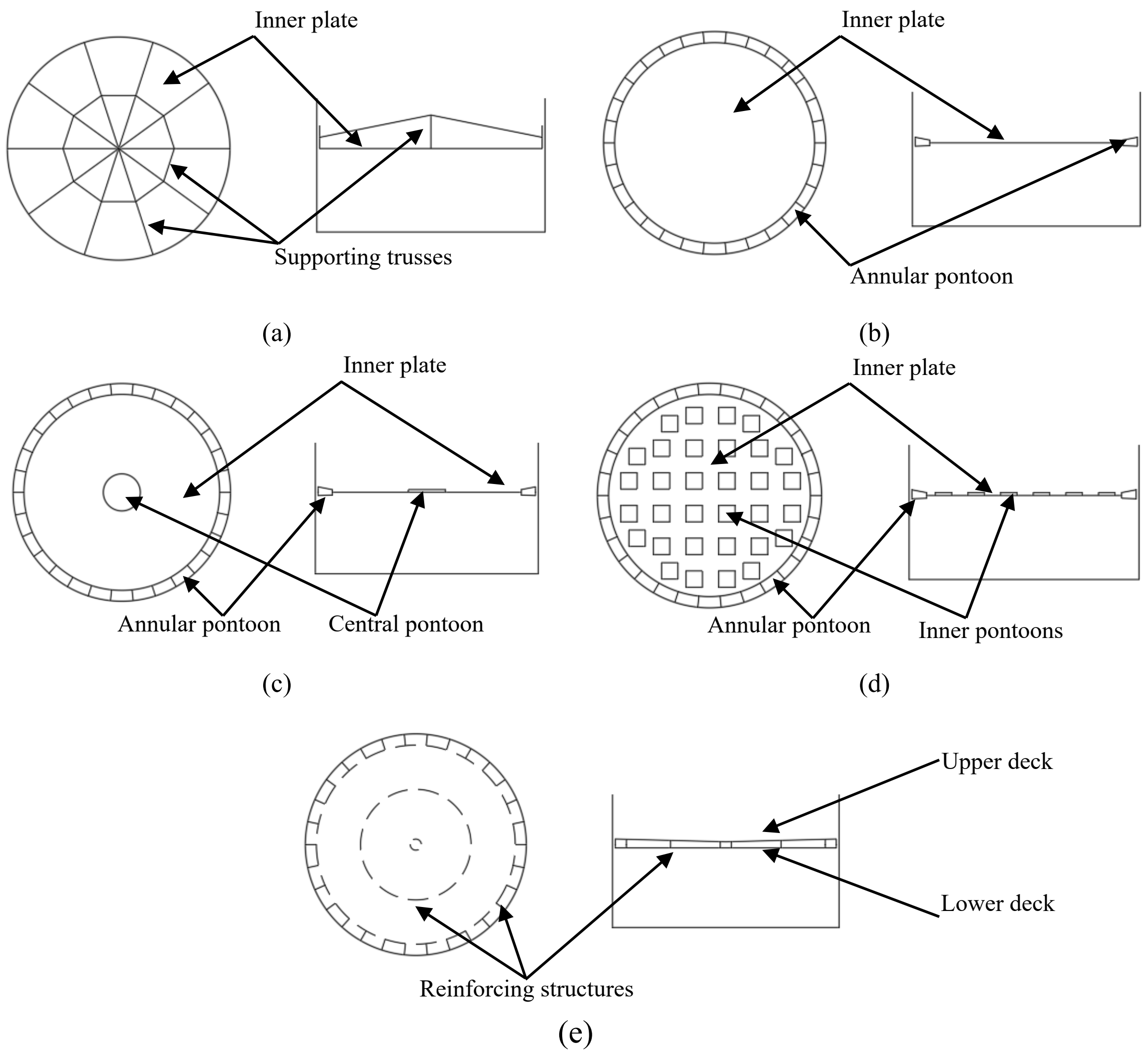

Figure 1: Types of external floating roofs (a) single deck with supporting trusses and no pontoon, (b) single deck with annular pontoon, (c) single deck with annular and central pontoon, (d) single deck with annular pontoon and inner pontoons and (e) double deck with reinforcing structures in between.

However, in the Thesis, only the single deck floating roof with an annular pontoon is addressed (Figure 1 (b)). For brevity, it this type of floating roof is termed simply as floating roof.

The floating of the roof is controlled by an annular pontoon sealed through a rubber gasket, which is in direct contact with the inner surface of the tank wall. On the top surface of the roof itself, several fittings (e.g. the rim sealing anchors) are installed to control the performance of the roof to provide draining of the water and exhausting of vapours (Pasley & Clark, 2000). Such floating roofs of cylindrical steel tanks can slide upward and downward depending on the filling level.

Analytical investigations and empirical evidence proved that the presence of the floating roof hardly influences the first sloshing mode, while the roof stiffness has a relevant impact on the higher-mode effects (Sakai et al., 1984). Morita et al. (2018) realized that a linear vibration mode could approximate the sloshing wave if the ratio between the maximum sloshing wave height of the first sloshing mode and the tank diameter is up to 0.15. However, if the sloshing wave height increases and the sloshing becomes nonlinear, the linear approximation of the sloshing wave may not be valid because it may cause underestimation of wave height. In this respect, many authors proposed correction coefficients and procedures for evaluating the sloshing wave height. Such corrections factors were calculated by using nonlinear analysis and were validated by experimental and analytical evidence (Sago et al., 2018). However, sloshing response is influenced by the type of floating roof, which is, however, often neglected in the model.

Several authors investigated the dynamic behaviour of tanks and their content without considering the effect of the floating roof. Simplified and refined models of tanks were developed. Several works by Malhotra (Malhotra & Veletsos, 1994; Malhotra, 1995; Malhotra et al., 2000), investigated the seismic behaviour of steel storage tanks. The scholars proposed models for the base uplifting and the dynamic response of the content, which was decomposed into two parts: the so-called impulsive response and the convective response. Several approaches were developed for the simulation of the impulsive and convective response of the tank content. The simplest model consists of two vertical cantilevers with lumped masses at one end and fixed at the base. The results of Malhotra's studies were presented in tables, which can be used to calculate the stiffness, masses and damping of the cantilevers based on the content height, density and geometrical properties of tanks. Later on, the so-called joystick model has been proposed by Bakalis (Bakalis et al., 2017) aimed at improving the base uplift. The model (see Figure 2) consists of a beam-column element that carries the impulsive mass, and it is supported by sufficiently rigid beams radially placed, which in turn rest on point/edge springs. The authors used nonlinear elastic material to idealize the uplift resistance of the edge springs, while the properties of the elastic element that connects the fluid mass to the base are estimated using an equivalent stiffness. In their model, the equivalent stiffness has to be selected, given the impulsive mass and height, capable of reproducing the fundamental (impulsive) period. The convective mass has been neglected in this model because its non-relevance in the overall response of the structure. Furthermore, the model can be used to simulate unanchored and anchored tanks both by redefining the supporting springs to simulate the anchors. An alternative to simplified models is refined finite element models of tanks (Virella et al., 2006; Buratti & Tavano, 2013). The refined models can be used to investigate the response of tank components, but such models are extremely computationally demanding, which may not be suitable for seismic risk studies.

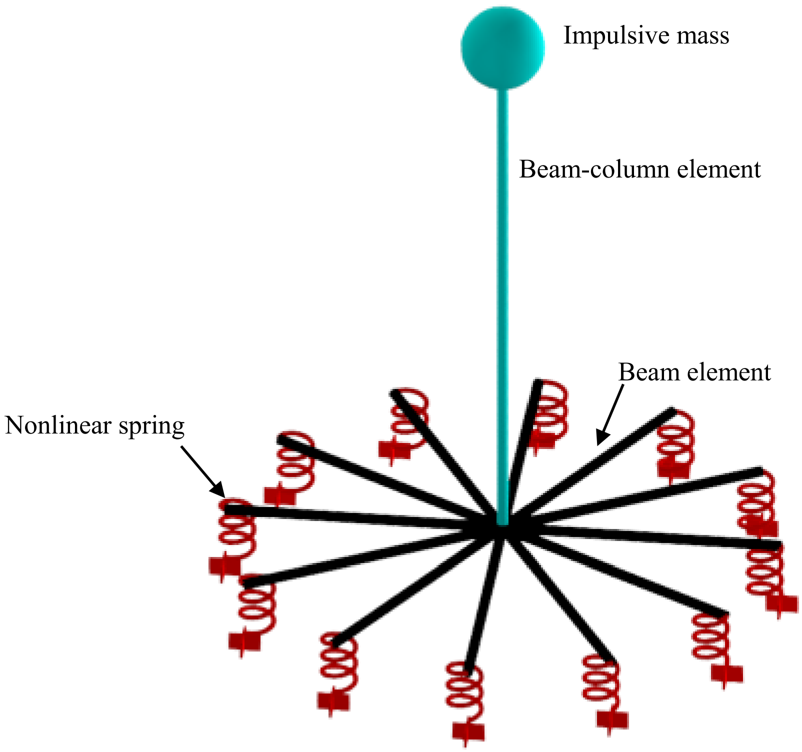

Figure 2: Steel storage tank joystick model.

Seismic performance assessment of tanks has been investigated by considering different performance metrics. In the last years, seismic risk assessment becomes increasingly popular. The authors investigated different failure modes. Attention has been paid to the wall-related damages such as elephant's foot buckling, diamond shape buckling or the base uplifting, anchors failures and loss of containment due to cracks in a tank wall or nozzle failures (Phan et al., 2017; Kummari et al., 2018). However, the authors focused primarily on tank wall failures and the consequent loss of content, while the effect of the floating roof failures was neglected. Such an approach was also used by Bakalis & Vamvatsikos (2018), who proposed a seismic vulnerability estimation procedure for tank farms. In the study, they demonstrated the proposed procedure by evaluating the seismic vulnerability of tanks, which are usually equipped with a floating roof, but they neglected failure modes associated with the roof failure. Caputo & Corritore (2018) assessed the performance of steel storage tanks with particular emphasis on the loss of content. The authors proposed an interesting approach that makes it possible to link damage and loss of containment directly. However, the effect of the loss of content due to large roof deformation was not taken into account. In the past experimental campaigns on steel storage tanks (De Angelis et al., 2010) relevant data were acquired. Shaking table tests of base-isolated tanks were performed by considering recorded and artificial ground motions. The results showed the effectiveness of the tested insulating devices in reducing the total pressure on the tank wall generated by the earthquake but, on the contrary, a low increase of the oscillation amplitude of the liquid surface, consequently of the floating roof, has been observed. The reason for this opposite behaviour lies in the fact that the vibration period of the impulsive component of pressure is generally in the order of few tenths of seconds. This implies high effectiveness of the base isolation system, while the period of convective component usually ranges in the order of a few seconds or more. In this respect, consideration of the effect of a floating roof in the seismic performance assessment of base-isolated liquid storage tanks become even more important (De Angelis et al., 2010).

Seismic risk assessment of loss of containment due to large vertical displacement of the floating roof has been disregarded mostly for the scarcity of numerical models capable to efficiently and sufficiently predict the seismic behaviour of the floating roof itself. Finite element (FE) models represent an alternative to simplified models. Due to the rapid development of computers, FE models are now frequently used for research purposes. These models have the advantage of allowing the direct modelling of floating roofs to evaluate their seismic response (Yamauchi et al., 2006; Kozak et al., 2010; Goudarzi, 2015). However, performing seismic analyses of tanks with FE models is still extremely computationally demanding. Thus such models are not suitable for seismic risk analyses that require hundreds of simulations. Scholars developed simplified linear-elasitc or non-linear models (Sakai et al., 1984; Matsui, 2007; Shabani & Golzar, 2012; Shabani, 2013). However, the seismic risk assessment with respect to loss of containment due to large vertical displacement of the floating roof was not yet addressed by simplified models. In this respect, the Thesis research tried to address the lack of seismic risk assessment using simplified models, such as the non-linear simplified model introduced by Shabani et al. (Shabani & Golzar, 2012).

1.3 Hypothesis and expected results

The research focused on verifying the following hypotheses:

- Seismic response of storage tanks equipped with a floating roof can be simulated with sufficient accuracy by utilizing a simplified model which takes into account the combined effects due to the dynamic interaction of the coupled roof-content system and the effects of the content on the tank itself.

- Current systems of tank floating roofs do not provide sufficient seismic safety against loss of content due to failures of the roof. Most common floating roof failures concern the sinking of the roof itself due to cracks in the deck or large displacements, buckling of the main plate due to the second-order effects and loss of content due to overtopping or fluid spilling. In all the cases, relevant are the consequences in terms of economic losses and adverse environmental impact.

The first hypothesis was verified by using the simplified model and different performance metrics for predicting seismic behaviour of a storage tank equipped with the floating roof (see Chapter 2, for the performance metrics, Chapter 3 for the floating roof simplified model and Chapter 4 for the validation of the latter one). The simplified model for the steel storage tank comprised of an available stick model concerning the impulsive content part. It was used for simulating impulsive response in the tank, while the effect of the floating roof was evaluated based on an analytical model presented in Chapter 3. The latter simplified model is based on the application of Hamilton's variational principle without and with consideration of the second-order effects (Shabani & Golzar, 2012; Shabani, 2013). The simplified model was validated by a refined finite element model (FE) developed in Abaqus (Dassault Systemes, 2019), which accounted for the frictional contact between the base and shaking table, the dynamic viscosity of the liquid, the steel-liquid interaction and materials property (e.g. the equation of state which relates pressure, temperature, and volume of the fluid). The accuracy of both models was validated using experimental results from the shake table test (CEA, 2017).

The second hypothesis was verified by seismic risk studies (see Chapters 5 and 6). For this purpose, the simplified model was used to assess the seismic fragility and risk of selected tanks equipped with a floating roof.

The expected results and the scientific contribution of the research, which were foreseen in the proposal for the topic of a doctoral dissertation, were:

1. A simplified model of liquid storage tanks with consideration of the effect of a floating roof will be developed. Such a model could be used for risk assessment which requires many simulations.

2. Improved knowledge of the seismic performance of liquid storage tanks will be provided with an emphasis on the simulation of the interaction between the liquid surface and the floating roof by a refined numerical model, which will be validated by the results of shake table tests.

3. An insight into the failure modes of a floating roof and proposals for limit states related to the failure of floating roofs will be provided.

4. A method for a seismic fragility and risk analysis of liquid storage tanks equipped with floating roofs will be proposed.

5. The seismic safety for current systems of floating roofs will be quantified.

The expected results and scientific contributions as foreseen in the proposal for the topic of the thesis are addressed in the following Chapters. Indeed, the simplified model of the tank is discussed in Chapter 3 and validated in Chapter 4. Moreover, in Chapter 4, the refined FE model is also presented and validated. Therefore, expected results and scientific contributions 1) and 2) are addressed in Chapters 3 and 4.

In Chapter 5, a discussion concerning the major consequences of loss of containment (LOC) in the process industries is provided. It resulted that one of the most hazardous LOC sources concerns the floating roof, and, more in detail, the sloshing appeared to be the most relevant. In this respect, attention was paid mostly to the LOC due to the floating roof overtopping. The definition of an appropriate limit state for the floating roof is not straightforward. Thus, in Chapter 5, a real steel storage tank equipped with a single deck floating roof is analysed. The description of the facility is presented, and a discussion concerning the definition of a proper limit state is provided, which addresses the expected result 3). The selected limit state is then used as a structural capacity for the following performance analyses.

The last two Chapters of the Thesis (Chapter 5 and 6) address the expected result 4) and 5). More in detail, the fragility analysis of the steel storage tank wall and the floating roof with particular effort on the investigation and the suitability of the simplified model previously introduced is addressed in the last part of Chapter 5. Furthermore, besides the simplified model, the EC 8-4 (CEN, 2006) formulation for the sloshing wave height was used, aiming to test its reliability concerning the case in which the presence of the floating roof was accounted. Later on, in Chapter 6, the conventional and the two risk-based performance metrics are used to assess the performances and the safety of the steel storage tank equipped with a single deck floating roof assumed as a case study. Furthermore, a risk mitigation strategy based on the probability of occurrence of the several possible filling levels is presented.

1.4 Thesis content

The thesis comprises eight Chapters, starting by an Introduction. The second Chapter, which comprises of four sections, presents the seismic performance assessment of code conforming and non-code conforming supporting structure of elevated tanks using three different performance metrics and the corresponding decision models. The investigated non-code conforming elevated tank is a replica of a tank that collapsed during the Kocaeli earthquake. The code conforming supporting structure of the tank was designed following Eurocode 8 provisions. The seismic performance assessment, which is focused on the supporting structure, is based on non-linear response history analysis by considering several filling levels of the tank. In section 2.1, the ground motion selection process is presented and discussed, focusing on the decision model to be used. Subsequently, in section 2.2, the conventional decision model is introduced. It accounts for the demand-to-capacity ratio given the seismic design action, while the conditional risk-based decision model and the risk-based decision model are presented in section 2.3. They account for the probability of exceedance of a designated limit state for a given design seismic action and the probability of exceedance of a designated limit state for a given period of time, respectively. Finally, in section 2.4, a discussion concerning the present Chapter is provided.

In Chapter 3, the mathematical formulation of the simplified model for the simulation of seismic response of a floating roof of liquid storage tanks and its step-by-step implementation using a software tool developed in Matlab (MathWorks, 2012) is presented. The model is based on five assumptions: tank walls and bottom plate are rigid; fluid is inviscid, incompressible and irrotational; rocking of the tank does not occur; the perfect contact between roof and fluid surface and seismic response of floating roof is linear elastic. Under this premises, the so-called Lagrangian of the coupled system floating roof-fluid was developed. Based on the Hamiltonian's variational principle, the equation of motion of the floating roof was then derived.

The Chapter 4 presents the experimental test conducted on a scaled steel storage tank equipped with a floating roof. It comprises four sections. The first section, 4.1, presents the experimental test, which was conducted on a shake table (CEA, 2017), aiming to investigate different phenomena that may occur during the earthquake. Authors (CEA, 2017) of the shake table test spent particular effort in the test mock-up, acquiring useful data concerning even the vertical displacement of the floating roof. As a part of this thesis, the data were post-processed and analysed. Subsequently, in section 4.2, a refined FE element model of the tested specimen was introduced, developed and described. Later on, in section 4.3, the experimental data were used to validate both simplified and refined FE models providing a comparison in terms of vertical displacement of floating roof and fluid provided by the simplified and refined FE models and experimental data. Furthermore, a parametric study was conducted on the simplified model to establish the most relevant parameters adopted in the formulation. Finally, in section 4.4, a discussion concerning the Chapter is provided.

The Chapter 5 introduces a real steel storage tank equipped with a single deck floating roof, which was selected as a case study. Firstly, in 5.1, the case study is presented and described, showing the location, the geometrical and mechanical properties, besides the main characteristics of the floating roof. Subsequently, in 5.2, a refined FE model is described, developed and presented. At the same time, a simplified model based on the one introduced in Chapter 3 is coded. Both numerical models were validated, and results compared. In section 5.3, a simplified model capable of simulating the seismic steel storage tank wall behaviour is presented and developed. This is followed by ground motion selection, with particular attention to the use of the selected ground motion and the definition of appropriate limit states. Indeed, in section 5.4, ground motions were selected for the study of the floating roof while, in section 5.5, focusing on the steel storage tank wall failures. The same occurred for the definition of the limit states of interest, which were presented in section 5.4 and 5.5 for content overtopping due to large floating roof vertical displacement and tank wall failure due to buckling phenomena, respectively. Section 5.6 presents the fragility analysis of the investigated steel storage tank with respect to the overtopping due to large vertical displacements of the floating roof and steel storage tank wall failure due to buckling phenomena. Finally, in section 5.7, a discussion of the Chapter is provided.

In Chapter 6, which is composed of three sections, the seismic performance and risk assessment of the selected tank is presented using the performance metric introduced in Chapter 2. In section 6.1, the conventional performance metric is adopted to assess the seismic performance of the investigated steel storage tank concerning the content overtopping due to large floating roof vertical displacement and tank wall failure due to buckling phenomena. In section 6.2, the risk-based decision models were used. Furthermore, in the last part of section 6.2, a risk mitigation strategy which accounted for the probability of having different filling levels was introduced and discussed. Finally, in section 6.3, the Chapter's content is discussed.

In the final part of the Thesis, the Chapter 7, all the findings were resumed, and the conclusions presented. The Thesis concludes with a list of references.

2 EVALUATION OF SEISMIC PERFORMANCE METRICS IN THE CASE OF STEEL STORAGE TANKS

In this Chapter, three performance metrics for the seismic performance assessment of the structures are investigated. In addition to the conventional performance metric, which involves a demand-to-capacity ratio for a given level of ground-motion intensity, the conditional risk-based and risk-based performance metrics are considered. Performance metrics are applied to an existing non-code-conforming elevated steel storage tank that collapsed during the Kocaeli earthquake and its code-conforming variant, designed according to Eurocode provisions. Because the focus is the evaluation of the available performance metrics, the case study does not refer to the tank with a floating roof.

2.1 Description of investigated elevated tanks, numerical models and limit states

The existing (i.e. non-code-conforming) and the code-conforming tanks and their supporting structures are introduced. The first example is an elevated steel storage tank located in Turkey. It was constructed in the 90s following the construction procedure of that period. Such a tank with a high filling level collapsed in 1999 due to the Kocaeli earthquake, while tanks with lower filling level did not collapse. A decade later, Eurocode standards were released. The supporting structure of the non-code-conforming elevated steel storage tank did not fulfil the requirements of the newest code. For comparison, a code-conforming support structure was designed according to Eurocode 8 provisions for a code-conforming tank with the same height and diameter as the non-code-conforming tank. It is assumed that both tanks are at the location of the existing tank.

2.1.1 Non-code conforming tank

The non-code-conforming elevated steel storage tank is presented in Figure 3. The tank was located in Izmit, Kocaeli county, which is a high seismicity region in Turkey. It collapsed on August 17, 1999, when an Mw = 7.4 earthquake struck the Kocaeli region. The earthquake affected millions of people and caused more than 15 billion USD in damage (Girgin, 2011). The area affected by the event is one of the most industrialised regions in Turkey. A total of 48% of all heavily damaged structures caused by the earthquake were observed in this region (Özmen, 2000), which also includes the collapse of the supporting reinforced concrete structure of the investigated tank (Figure 3).

Figure 3: View on the non-code-conforming elevated steel storage tank that collapsed during the earthquake (Sezen & Whittaker, 2006).

The non-code-conforming tank was practically new when the earthquake hit. The tank was built in 1995 and consisted of two concentric stainless-steel walls, the outer with an outside diameter of 14.6 m and the inner with an outside diameter of 12.8 m. The gap between the walls was filled with insulation. The tank was supported on a reinforced concrete slab with a diameter of 14.6 m and a thickness of 1.07 m. The slab was supported by sixteen reinforced concrete columns with a diameter of 500 mm. The height of the columns was 2.5 m. Each column was reinforced with sixteen, 16 mm diameter longitudinal bars and 8 mm diameter stirrups at 100 mm with yielding stress of 420 MPa (Phan et al., 2017). The overall height of the tank was about 16 m.

2.1.2 Code conforming tank

The supporting structure of the code-conforming elevated tank was improved. Columns were designed according to Eurocode 8 for the ductility class high (DCH). The new code required increasing the column diameter from 50 cm to 70 cm. Concrete C30/37 and steel S500C were used for the columns. The resulting cross-section of the columns and the corresponding longitudinal and transverse reinforcement are presented in Figure 4.

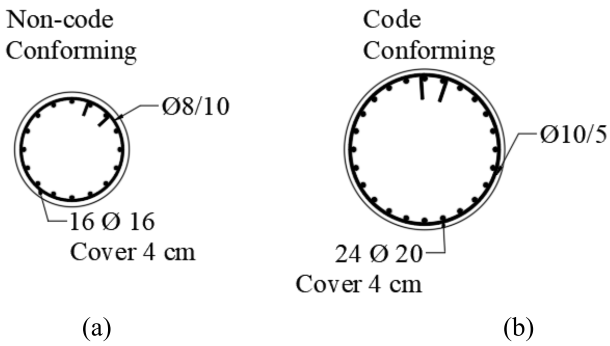

Figure 4: Cross-section of the columns of supporting structure of (a) non-code-conforming elevated tank, 50 cm of diameter and (b) code-conforming elevated tank, 70 cm of diameter.

Note that in the design, loads were combined with the basic load combinations (actions for permanent or transient design situations) according to EN 1990:2002 6.4.3.2. The effects of the contents shall be considered in the variable loads for two tank filling levels: empty or full, as prescribed in EC 8-4 (CEN, 2006). The seismic design action was defined according to EC 8-1 (CEN, 2004) by considering return period T_{NCR} = 475 years because the investigated tank is classified as a structure of ordinary importance. The design peak ground acceleration (PGA) was then obtained from the Kocaeli seismic hazard function (Figure 5) using the results of SHARE project by Woessnert et al. (Woessner et al., 2015). The resulting PGA for the return period of 475 years is 0.5 g.

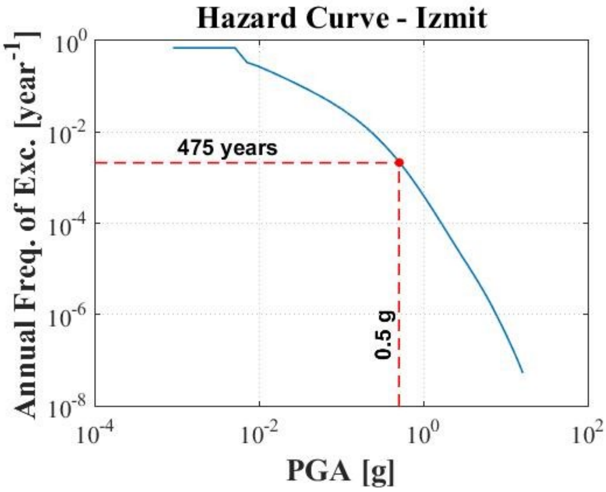

Figure 5: Seismic hazard function for Kocaeli based on SHARE project.

A soil type A was assumed. The importance factor γ_I was considered unitary because it was related to a ‘medium risk to life and local economic or social consequences of failure belong to Class II’ as prescribed by the code EC 8-4 (CEN, 2006). The supporting structure was classified as the ‘Moment resisting frames’. Hence, the initial value of the behaviour factor was assumed to be 4.95 for DCH. This value of the behaviour factor was, according to the provisions of EC 8-4, multiplied by 0.7 (CEN, 2006), which resulted in a final behaviour factor of 3.47. The seismic demand was estimated based on the seismic combination considering the recommended value of φ =1 for a full tank and φ = 0 for an empty tank. Because the importance factor γ_I = 1, the design peak ground acceleration $a_{g,R}$ = 0.5 g, which corresponds to the return period of 475 years. Note that the content of the tank was liquid with a density of 1150 kg/m^3 and, for the present study, the height of the content was assumed to vary from 90% to 0% of the tank height. During the Kocaeli earthquake, two tanks were filled to 85% and the remaining tank was filled to 25%.

The presented structural models emphasise the model of the columns of the supporting structure, which are the most vulnerable components of the tanks. The steel tank is thus modelled by a 3D finite element stick model (Figure 6). This latter is a simplified but computationally efficient numerical model. It comprises lumped masses, as presented in Figure 6, which are connected to the supporting structure by cantilevers that have similar dynamic characteristics and can be observed in the tanks due to the impulsive and convective response. The tank mass is rigidly connected. Supporting columns and cantilevers used to connect lumped impulsive and convective masses to the support structure are modelled employing beam elements. The columns' heads and the centre of the reinforced concrete slab are connected rigidly (Figure 6). Three nodes circled in yellow in Figure 6 are rigidly connected to simulate the thickness of the slab. The slab mass is considered in the central node.

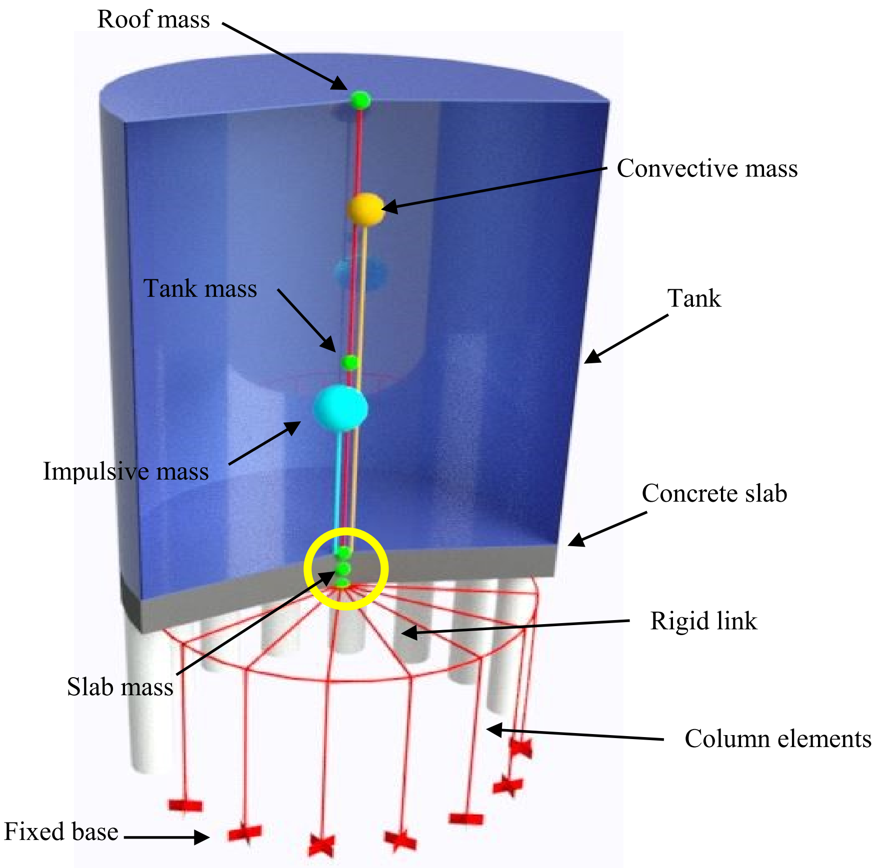

Figure 6: The 3D model of the elevated tank comprising column elements and the rigid links to simulate the support structure, the independent cantilevers used to connect impulsive and convective masses, and the tank and roof masses rigidly connected to the slab nodes with the slab mass at the middle.

The model is consistent with the EC 8-4 provisions (CEN, 2006). Note that the code provides a simplified approach for the modelling of the tank-liquid system concerning fixed-base, cylindrical tanks. However, these provisions can be used even for modelling the elevated tanks because they are fixed to the rigid slab of the supporting structure.

The insulating material between the external and internal walls was neglected because its mass and stiffness have a minor effect on the seismic response of the supporting structure. The mass of the tank and the roof were rigidly connected to the slab, while the lumped masses of the content were connected to the slab by linear elastic cantilevers with appropriate constants. Lumped masses representing the content were decomposed to the impulsive mass, m_i, and the convective mass, m_c, which were connected by linear elastic cantilevers with stiffness equal to k_i and k_c, respectively. Impulsive and convective masses were calculated according to the tabled values provided in EC 8-4, Table A.2, (CEN, 2006). Table 1 presents a resume of masses, elevation, and stiffness of the connection, from 90% filling level (14.4 m) to 20% filling level (3.2 m). Tank and roof masses were 38 t and 6 t, respectively, while the support structure mass was 364 t.

In addition to the mass and the stiffness of the cantilevers, which are used to simulate the convective and impulsive response of the tank, it is necessary to define the model for the viscous damping. In this respect, according to the provisions of EC 8-1 and EC 8-4 (CEN, 2004; CEN, 2006), a damping ratio of 5% was accounted for all modes through the design acceleration spectrum.

Table 1: Impulsive and convective masses and stiffness for 90%, 85%, 25%, and 20% filling levels of the tank. The elevations of the masses are also presented.

Mass type	Filling level	Mass [t]	Elevation [m]	Stiffness [KN/m]
m_i	90%	$1.7 \cdot 10^3$	6.14	$1.3 \cdot 10^6$
	85%	$1.6 \cdot 10^3$	5.77	$1.4 \cdot 10^6$
	25%	$2.2 \cdot 10^2$	1.6	$1.7 \cdot 10^6$
	20%	$1.4 \cdot 10^2$	1.28	$1.5 \cdot 10^6$
m_c	90%	$4.5 \cdot 10^2$	11	$1.3 \cdot 10^3$
	85%	$4.5 \cdot 10^2$	10.3	$1.3 \cdot 10^3$
	25%	$3.7 \cdot 10^2$	2.2	$8.6 \cdot 10^2$
	20%	$3.3 \cdot 10^2$	1.7	$6.8 \cdot 10^2$

A linear elastic model was developed according to the Eurocode provisions for the design of the supporting structure. The modelling philosophy was the same as that previously introduced, while mechanical properties and material adopted are listed in Table 2. The model (Figure 7) was developed in SAP2000 (CSI, 2011) by analogy to the information presented in Figure 6. The seismic demand on columns was obtained by the response spectrum analysis. Once the design had been created, the seismic performance assessment of the code-conforming tanks was carried out using a non-linear model, which was developed in OpenSees (McKenna & Fenves, 2010) as described in section 2.1.3.

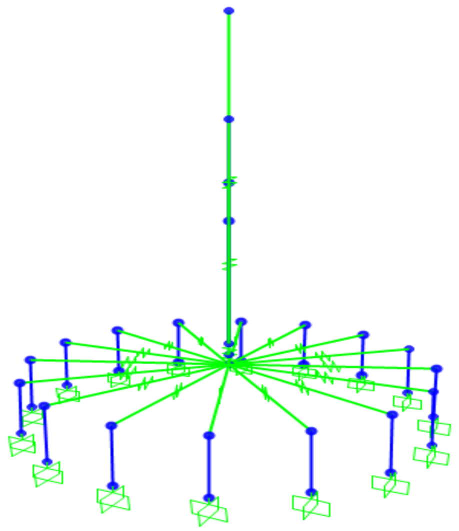

Figure 7: Linear elastic model of the elevated tank developed in SAP2000.

2.1.3 Non-linear model for the seismic performance assessment of the elevated tanks

The non-linear model of the elevated tank was developed in OpenSees. The supporting reinforced concrete columns were modelled with 3D non-linear beam-column elements with fibre cross-sections. The column section was divided into two parts to consider the confinement effect of the stirrups on the concrete core, as presented in Figure 8. The confinement effect was taken into account by increasing the compressive concrete strength as allowed by Eurocode (CEN, 2004a). Concrete behaviour was modelled using the Kent-Scott-Park model (Scott et al., 1982), which is already implemented in OpenSees throughout uniaxial material Concrete01. The stress-strain behaviour of reinforcing rebars was simulated using Giuffré-Menegotto-Pinto model coded in OpenSees environment and named Steel02 (Filippou et al., 1983). The adopted mechanical properties of the material adopted in the model are presented in Table 2. Column heads were, later, rigidly connected to the centre of gravity of the supporting slab. Each lumped mass simulating the fluid and tank itself was connected to the supporting slab by an elastic element with appropriate stiffness, as previously discussed. The damping ratio, assumed to be proportional to the convective mass and impulsive mass, was assumed to be 0.5% and 2%, respectively (Malhotra et al., 2000).

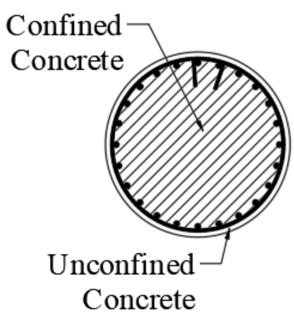

Figure 8: Confined and unconfined column cross-section.

The columns of the non-code-conforming tanks were particularly vulnerable to shear failures, as demonstrated by the failure mechanism during the Kocaeli seismic event (Sezen & Whittaker, 2006). The shear force – shear deformation behaviour for the pure-shear failure of the supporting structure was simulated employing the model introduced by Setzler et al. (Setzler & Sezen, 2008), which is not implemented in the OpenSees software. To introduce the stress-strain model to the supporting reinforced concrete columns, the section aggregator command of the OpenSees was used to provide a uniaxial hysteretic material to represent the sectional shear behaviour (Figure 9) , as suggested by Phan et al. (Phan et al., 2017).

However, the first and the second characteristic points of the shear force – shear deformation relationship of the so-defined material were calculated based on the modified compression field theory using the Response 2000 software (Bentz, 2000). The first and second point characterise, respectively, the shear deformation at which the first crack appears, γ_{cr}, and the shear deformation corresponding to the maximum shear force, γ_y. The third point, γ_u, was obtained according to the procedure proposed by Elwood et al. (Elwood & Moehle, 2005). The shear force of the third point corresponds to the 80% drop of maximum shear force. The values of the described characteristic points of shear force – shear deformation relationship are presented in Table 3 and Table 4 for each considered filling level for the non-code and code-conforming tanks, respectively.

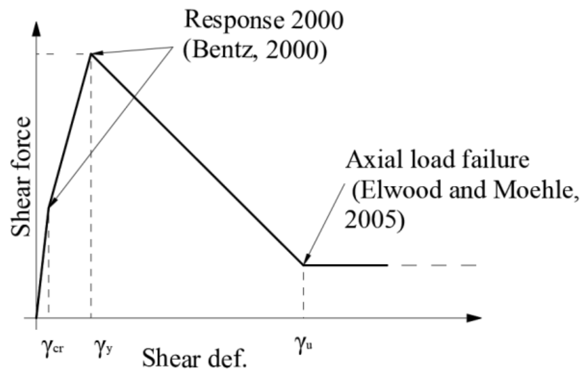

Figure 9: The shear force – shear deformation relationship of the columns.

Table 2: Material properties adopted for the non-linear model.

Material	Density [kg/m³]	E [MPa]	Strength [MPa]	
			Non-code-conforming	Code Conforming
Conf. Concrete	2500	32000	39	49
Unconf. Concrete	2500	32000	30	38
Reinforcement	7850	210000	420	575

Table 3: The characteristic points of shear force – shear deformation relationship in the non-linear model of the columns of non-code conforming supporting structure of the elevated tank.

Filling level	**Non-code-conforming**					
	γ_{cr} **[%]**	**Shear [KN]**	γ_y **[%]**	**Shear [KN]**	γ_u **[%]**	**Shear [KN]**
90%	0.01	103	0.03	583	10	117
80%	0.01	103	0.07	496	10.33	99
70%	0.01	103	0.08	491	10.35	98
60%	0.01	103	0.08	481	10.32	96
50%	0.01	103	0.08	470	10.37	94
40%	0.01	103	0.02	448	10.38	90
30%	0.01	103	0.02	413	10.39	83
20%	0.01	103	0.02	414	10.40	83
0%	0.01	104	1.33	397	10.40	79

Table 4: The characteristic points of shear force – shear deformation relationship in the non-linear model of the columns of code conforming supporting structure of the elevated tank.

Filling level	**Code Conforming**					
	γ_{cr} **[%]**	**Shear [KN]**	γ_y **[%]**	**Shear [KN]**	γ_u **[%]**	**Shear [KN]**
90%	0.46	902	1.09	1295	10.43	259
80%	0.46	934	1.10	1328	10.43	266
70%	0.47	962	1.11	1341	10.43	268
60%	0.47	988	1.12	1353	10.44	271
50%	0.43	957	1.13	1355	10.44	271
40%	0.47	1041	1.14	1360	10.44	272
30%	0.43	1018	1.16	1363	10.44	273
20%	0.40	990	1.02	1378	10.44	276
0%	0.01	338	1.05	1389	10.41	278

2.1.4 Definition of limit state

Several failures modes can occur in industrial facilities, which have been an object of interest by several authors (Cozzani & Salzano, 2004; Paolacci et al., 2011; Phan & Paolacci, 2018). Moreover, the strengthening of the supporting structure may cause other failure modes mostly related to the tank itself (e.g. tank wall failures due to buckling, the anchorage system failure, or the connected fittings failures). However, in the present study, attention was paid only to the support structure.

The near-collapse (NC) limit state was defined by the damage observed in the columns of the supporting structure. Note that other failure modes related to the tank itself (e.g. tank wall failures due to buckling), the anchorage system, or the connected fittings (e.g. nozzles, pipes, etc.) may occur. The present study assumed that the tank and other components of the system were less vulnerable than the supporting structure. In a more general case, the performance of all components of the system should be considered.

The NC limit state was assumed to occur when the chord rotation exceeds the ultimate chord rotation, which was assumed to correspond to 85% strength in the post-capping range in the case of the code-conforming tank. Such an approach is not fully consistent with the Eurocode (CEN, 2005) definition, which prescribes an NC limit state at 80% strength. Nevertheless, the authors decided to adopt a slightly more stringent criterion than that defined in the Eurocode. In the case of the non-code-conforming tank, the NC chord rotation was assumed to correspond to the maximum shear force in the pushover analyses because of the brittle behaviour displayed in the Kocaeli earthquake (Sezen & Whittaker, 2006).

Such an approach guaranteed consistency between the definition of the NC limit state and the non-linear model. For simplicity, it was decided to estimate the NC chord rotation by performing pushover analysis, as demonstrated in Figure 10.

Pushover analyses were performed and accounted for the most relevant modal shape capable of exciting most of the total mass (support structure and content), providing, in this respect, a modal-shaped loading profile. In this manner, even the variation of the filling level, thus the content mass, was considered.

Note that in Figure 10, the pushover curves and LS for the code-conforming and the non-code-conforming tanks are presented for filling levels from 90% to 0%. Note that, due to the circular shape of the columns and supporting structure, the pushover curves are not affected by the loading direction.

Based on the pushover analysis, the NC chord rotations were estimated for each filling level of the tank. They were used to identify the NC limit state in the response history analysis. The resulting values of the NC chord rotations are presented in Table 5.

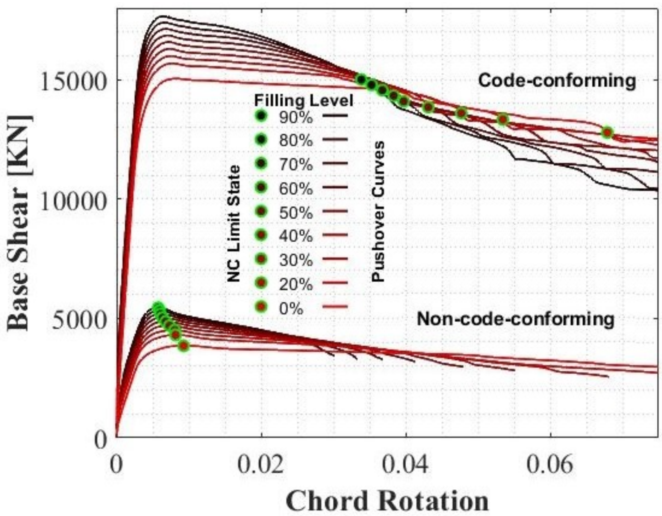

Figure 10: The shear force – chord rotation relationship of the columns.

Table 5: The chord rotation capacities for the NC limit state with consideration of different tank filling levels.

Filling level	NC chord rotation	
	Non-code-conforming	Code-conforming
90%	0.006	0.034
80%	0.006	0.035
70%	0.006	0.037
60%	0.006	0.038
50%	0.007	0.040
40%	0.007	0.043
30%	0.008	0.048
20%	0.008	0.053
0%	0.009	0.068

2.2 Seismic performance assessment of tanks subjected to Kocaeli ground motion

During the Kocaeli earthquake, the peak ground accelerations were recorded in the range from 0.2 *g* to 0.4 *g* (Sezen & Whittaker, 2006). The ground motion considered in this study was recorded at the Kocaeli recording station, which is located in the same county as the elevated tanks that collapsed during the earthquake. The peak ground accelerations for two horizontal components were respectively PGA = 0.15 *g* and PGA = 0.22 *g*, for Direction 1 and Direction 2, respectively. The vertical component was neglected in the response history analysis (CEN, 2004). The ground motions and the corresponding acceleration spectra are presented in Figure 11.

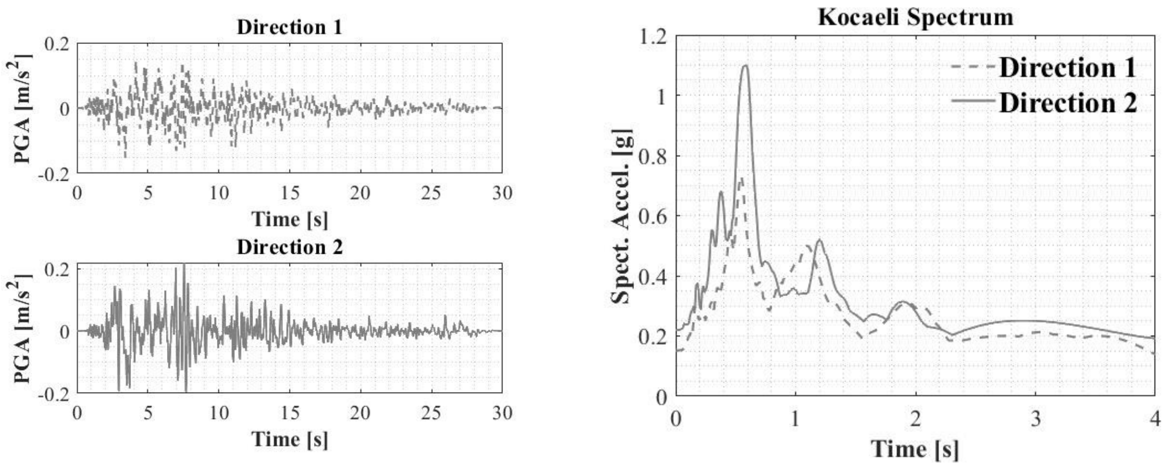

Figure 11: Horizontal components of the Kocaeli ground motions and the corresponding acceleration spectra.

The seismic response of the non-code-conforming tank is first simulated for the Kocaeli ground motion to compare the simulated damage of the tank with the damage observed after the earthquake and to observe the impact of the tank filling level on the seismic response of the tank. In addition, the seismic response of the code-conforming tanks to the Kocaeli ground motion is also presented. The damage associated with the NC limit state is observed with the demand-to-capacity ratio, which considers the NC chord rotation presented in Table 5. The chord rotation demand was calculated as the ratio between the maximal displacement at the top of the columns and the height of the columns. The resulting demand-to-capacity ratios are presented in Figure 12 (a) and Figure 12 (b) for the non-code-conforming and the code-conforming tank, respectively. The results are presented for 85% and 25% filling levels, which were the levels in the tanks during the Kocaeli earthquake. The NC limit state was exceeded in the non-code-conforming tank filled at 85%, while no exceedances were observed for the tanks filled to 25% of the filling level. The observed performance of the non-code-conforming tank is similar to the performance of the actual tanks during the Kocaeli earthquake. The tanks with 85% tank filling level collapsed, while the tank with 25% was undamaged. Some elevated tanks collapsed during the Kocaeli earthquake. If the supporting structure had been designed according to Eurocode, the damage to the supporting structure would have been negligible, which was proven by simulating the seismic response of the code-conforming tanks. Figure 12 (b) shows that the demand-to-capacity ratio in the columns of the supporting structure is on the order of 0.1 if the filling level of the tank was 85%. The seismic performance of the tank's supporting structure designed for DCH was observed to be almost elastic.

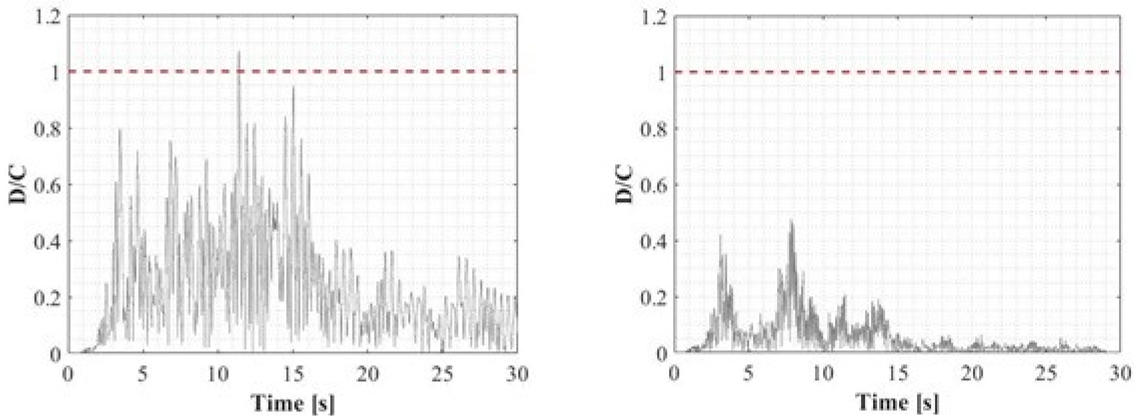

(a)

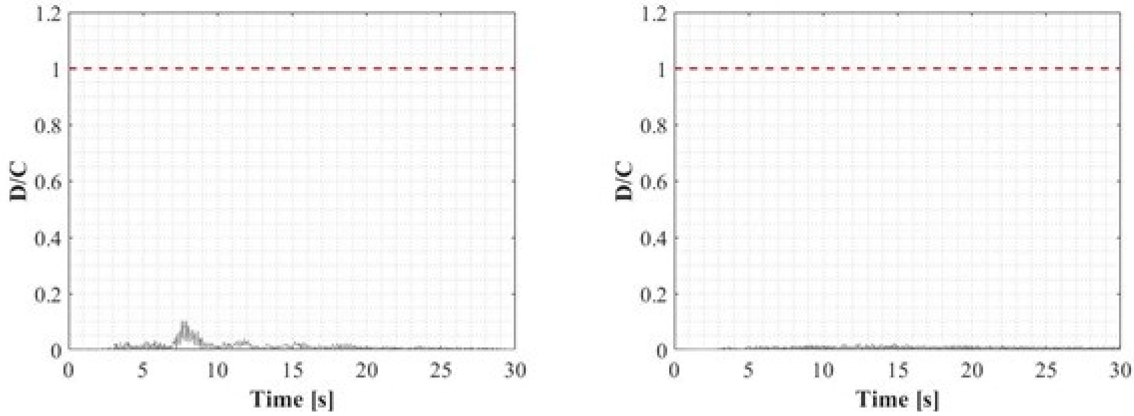

(b)

Figure 12: The simulated demand-to-capacity ratio in the columns in the case of the Kocaeli earthquake for (a) the non-code-conforming tank and (b) the code-conforming tank, with the tanks filled to 85% (left) or 25% (right).

Furthermore, the increase in the filling level causes a greater mass and longer impulsive vibration period (Table 6), while the convective vibration period decreases by increasing the filling level (Table 6). For this ground motion, the increase of the impulsive period almost always resulted in higher spectral acceleration (see Figure 13), which consequently increased seismic forces. On the other hand, the variation of the filling has a small impact on the seismic action due to convective mass because the seismic action effects of convective mass are usually marginal even for the most non-slender tanks (Bakalis, 2017). Namely, the convective mass is smaller in comparison to the impulsive mass, and spectral accelerations related to high vibration period of the convective response (i.e. from 3.7 to 4.4 s in the case of the investigated tanks) are very small. Note that periods presented in Table 6 were calculated according to the EC 8-4 (CEN, 2006) (A.35 and A.36 for the impulsive period and convective period, respectively). However, the maximum allowable chord rotation in the support structure (see Table 5) reduces with the increase of the filling level (Table 5). Thus, exceeding the capacity of the columns is most likely for configurations with a high level of filling. Due to non-linear effects, exceptions are possible.

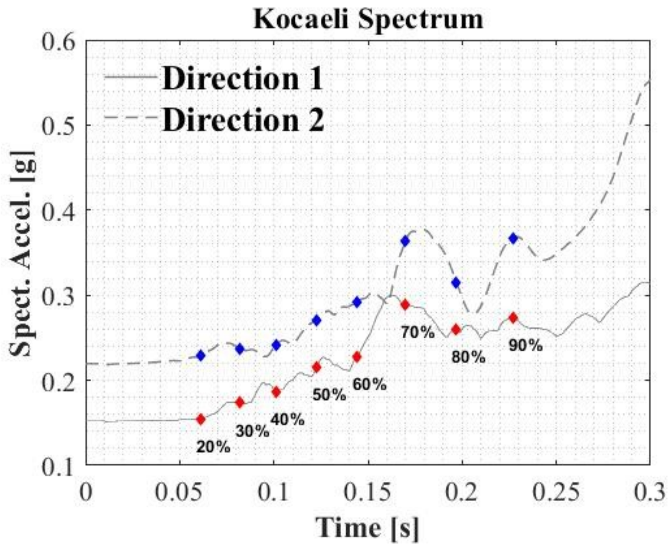

Figure 13: Corresponding spectral acceleration for the impulsive periods according to different filling levels for the Kocaeli spectrum in both horizontal directions.

Table 6: Impulsive (T_i) and convective (T_c) periods for filling levels ranging from 90% to 20%.

Filling level	90%	80%	70%	60%	50%	40%	30%	20%
***T_i* [s]**	0.22	0.19	0.17	0.14	0.12	0.09	0.08	0.06
***T_c* [s]**	3.74	3.74	3.74	3.74	3.80	3.85	4.01	4.40

2.3 Seismic performance assessment of tanks using three decision models

2.3.1 Description of conventional, conditional risk-based and risk-based decision models

Three decision models are presented and described. Figure 14 presents the workflow and the decision-making process for all three decision models to highlight similitudes and differences (red dashed border) that distinguish each decision model from the others. The two risk-based decision models share the need for a proper seismic hazard site characterisation to establish the seismic intensity for the definition of the most appropriate target spectrum. The definition of the target spectrum is the first process common for all three decision models, but the resulting target spectra differ.

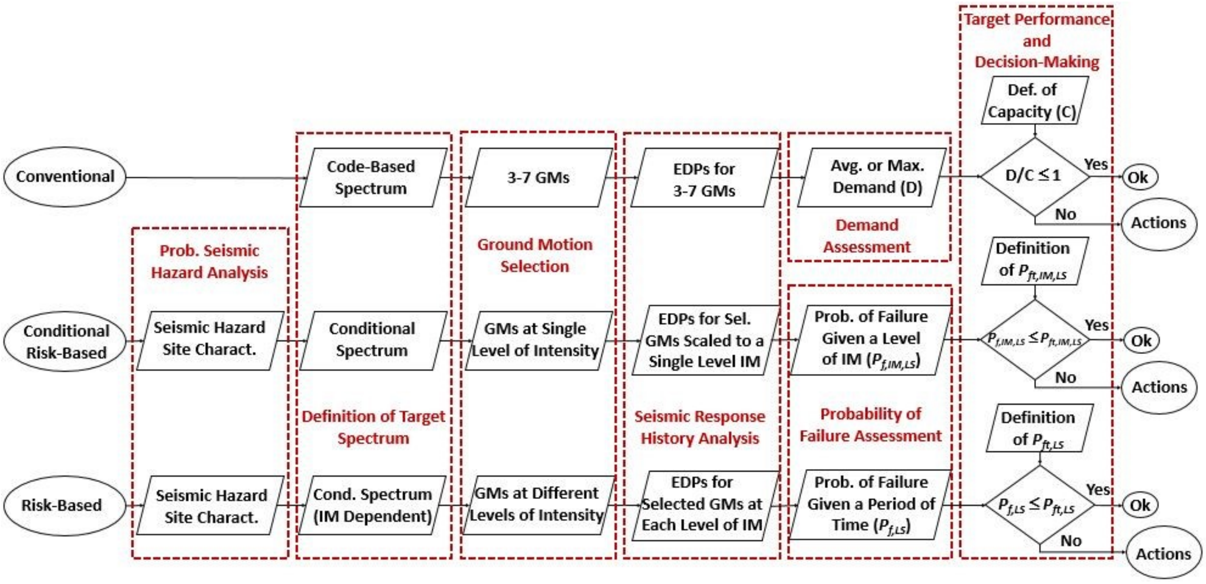

Figure 14: The workflow of the conventional decision model, conditional risk-based decision model and risk-based decision model.

The conventional decision model allows the user to use the code-based spectra directly and select at least three ground motions (CEN, 2004). Seven ground motions were considered in the case study. The demand used in the decision-making process was estimated by an average value rather than the maximum of engineering demand parameters resulting from the seismic response history analyses of seven ground motions (clause 4.3.3.4.3(3) of Eurocode (CEN, 2004)).

The conditional risk-based decision model and the risk-based decision model require more precise information about probabilistic seismic hazard analysis because the conditional spectrum defines the target spectrum. While the first approach requires the selection of ground motions at a specific seismic intensity to which the decision model is conditioned, the latter approach requires the selection of ground motions at multiple seismic intensities. In the present case study, 50 ground motions were selected for the conditional risk-based decision model, while the same number of ground motions was selected at different seismic intensity levels for the risk-based decision model.

The seismic response analysis, which is the simplest in the case of the conventional decision model, follows. The seismic response analysis for the other two decision models is equivalent to that from the conventional decision model but performed for significantly more ground motions. The conditional risk-based decision model provides a 'single stripe analysis'. The outcomes of the seismic response history analyses are represented by a multiple stripe analysis (MSA) (Jalayer & Cornell, 2009) or incremental dynamic analysis (IDA) (Vamvatsikos & Fragiadakis, 2010) for the risk-based model. In the present case study, the MSA was adopted.

The split between the three decision models is introduced in the next process, which involves the demand assessment and probability of failure assessment, respectively, in the case of the conventional decision model and the other decision models. For the conventional decision model, the demand is characterised by the mean values of the engineering demand parameters. However, in the case of conditional risk-based and risk-based decision models, the outcomes of the probability of failure assessment process are, respectively, the probability of exceeding a limit state for a given seismic intensity level, $P_{f,IM,LS}$, and the probability of exceeding a limit state for a given period, $P_{f,LS}$. The $P_{f,IM,LS}$ was calculated simply as the ratio between the ground motions that cause the exceedance of the LS (n_{LS}) and the total number of the selected ground motions (n_{GM}). $P_{f,LS}$ can be calculated by the conventional risk equation (McGuire, 2004; Jalayer & Cornell, 2009; Lazar & Dolšek, 2014) Eq. (1):

$$\lambda = \int_0^\infty P(C|IM = im) \cdot \left|\frac{dH(im)}{d(im)}\right| \cdot d(im) \tag{1}$$

where λ is the rate of exceedance of the selected limit state, *im* is the value of random variable IM representing the seismic intensity measure, $P(C|IM = im)$ is the probability of exceeding a designed LS given IM = *im,* and *H(im)* is the hazard function of the site of interest. Note that λ is practically equal to the probability of failure for one year, $P_{f,LS}$. This statement is valid for the low values of λ, which is the case when it corresponds to the exceedance of near-collapse limit state. Under the assumption of the linearisation of the hazard function in log-domain, Eq. (1) can be represented in the closed-form solution (McGuire, 2004; Jalayer & Cornell, 2009), as presented in Eq. (2):

$$\lambda = k_0(\mu)^{-k} \cdot e^{0.5 \cdot k^2 \cdot \beta^2} \tag{2}$$

where k is the slope of the linear approximation of the hazard function in the log-domain, and k_0 is its intercept, μ is the median value of the IM that causes the exceedance of LS, and β is the corresponding standard deviation of the natural logarithms of the IM which causes the exceedance of the LS.

The differentiation of the demand in the case of the three decision models is reflected in the target performance. The capacity (C) in the case of the conventional decision model is defined by the engineering demand parameter associated with the exceedance of a limit state of interest. Because the demand in the other two decision models is expressed by the probability, it is necessary to define the target performance with the target probability.

For the conditional risk-based decision model and the limit state of interest, the target performance is defined using the target probability of exceeding the limit state ($P_{ft,IM,LS}$). The limit state of interest of this study is the NC limit state, and the level of seismic intensity corresponds to the return period of 2475 years as defined in EC 8-3 (CEN, 2005). For $P_{ft,IM,LS}$, we refer to ASCE/SEI 7-10 (ASCE/SEI 7-10, 2010), which provides a threshold in terms of probability of exceeding different limit states according to their consequences for a maximum credible earthquake (MCE). MCE is 'the most severe earthquake effects considered by this standard'. In more detail, an MCE can be defined in two ways: with adjustment to target collapse risk (MCE_R) and without adjustments to target risk (MCE_G). MCE_R is calculated via an iterative procedure starting from a collapse fragility function with assumed dispersion and hazard functions for the site of interest. MCE_G ground motion is obtained from mean hazard curves for the site of interest considering the mean annual frequency of 1 in 2475 years, which corresponds to a probability of exceeding of 2% in 50 years (Luco et al., 2007; Petersen et al., 2018). Moreover, ASCE/SEI 7-10 defines the design earthquake as 2/3 of MCE_R, while the target probability of exceeding a limit state given a designated level of seismic intensity ($P_{ft,IM}$) primarily depends on the severity of limit state. The ASCE/SEI 7-10 accounts for two limit states: 'total or partial structural collapse' and 'failure that could result in endangerment of individual lives'. The corresponding target probability of exceeding the LS also depends on the risk category. In this study, the content of the tank is not hazardous. The collapse does not 'cause a substantial economic impact and/or mass disruption of day-to-day civilian life' but neither to have 'a low risk to human life in the event of failure'. Thus, according to the risk category classification provided by the code, the most appropriate risk category for the investigated tank is risk category II (ASCE/SEI 7-10, 2010). Consequently, the allowable probability of exceeding a LS that can cause the 'total or partial structural collapse' in the case of MCE is 10%. This value was adopted in this study for $P_{ft,IM,LS}$.

Concerning the target performance of the risk-based based decision model, some standards already address the target probability of failure given a period (e.g. (ASCE/SEI Standard 43-05, 2005)), while others, for instance, the working draft of new Eurocode (CEN, 2019), are still in the development process. In the state-of-practice, P_{ft} basically depends on the definition of LS. Thus, the limit states of interest need to be selected. For this study, the near-collapse limit state was selected to be verified. A similar limit state is also assigned by ANS 2.26 (American Nuclear Society et al., 2004) to units related to seismic design category 2, which is the category to which the investigated tanks are assigned because the content of the tank is not hazardous. Consequently, the target probability of exceeding the NC limit state for one year and 50 years is equal to $4 \cdot 10^{-4}$ and 2%, respectively. The limit state and the corresponding target probability of exceeding are thus consistent with ASCE 43-05 (ASCE/SEI Standard 43-05, 2005) and compatible with the draft of the new Eurocode (CEN, 2019) which informatively defines a target probability of exceeding the near-collapse limit state to $2 \cdot 10^{-4}$ (i.e. 1% in 50 years) for consequence class 2 (CC2) structures. However, the adopted $P_{ft,LS}$ can be considered very high if compared to the target probability of exceeding less stringent limit states related to permanent load and variable loads (, 2002). Thus, the target reliability from Eurocode 0 cannot be directly comparable to target seismic risk. In a more general case, however, the definition of target probability of limit state exceeding due to earthquakes can be related to fatality risk or the performance of the system (e.g. (Tsang & Wenzel, 2016; Crowley et al., 2017; Crowley et al., 2018; Tsang et al., 2018; Lazar Sinković & Dolšek, 2020)) which was, not addressed in the study due to simplicity reasons.

2.3.2 Ground motions for the performance assessment using three decision models

Ground motions for the performance assessment using the conventional decision model were selected according to Eurocode 8, as discussed in section 2.3.2. A set of seven ground motions was selected through Rexel software by Iervolino et al. (Iervolino et al., 2010), which is based on target spectrum matching. The software searches for pairs of the two horizontal components of ground motions. In the present case, seven pairs were selected for a total of fourteen records. In the selection procedure, the average spectrum of the fourteen records was matched to the target spectrum. This procedure was found to be adequate in Iervolino et al. (Iervolino et al., 2009) concerning Eurocode provisions (CEN, 2005), even if it is not fully compliant with the Eurocode.

The target spectrum was selected as the Type 1 spectrum of the Eurocode provisions and normalized to PGA=1 g (from the hazard curve at T_R=2475 years). The spectra of the selected records, the corresponding mean spectrum, and the target spectrum are presented in

Figure 15.

The most common target spectrum for the ground-motion selection is the uniform hazard spectrum (UHS). However, the UHS was found to be unsuitable as it conservatively implies large-amplitude spectral values at all periods within a single ground motion (Baker, 2010). Hence, the conditional spectrum approach is used for ground motion selection in the case of conditional risk-based and risk-based decision models. Ground motions were selected according to the algorithm proposed by Jayaram et al. (Jayaram et al., 2011). The PGA was assumed as the seismic intensity measure IM.

Because the fragility analysis was performed by multiple-stripe analysis (Jalayer & Cornell, 2009), different sets of ground motions were selected for different levels of PGA. Note that twenty-five PGA intervals from 0.1 g to 4 *g* were identified, spaced every 0.1 g from 0.1 to 1 *g*, and then every 0.2 *g*. Fifty GMs were selected using the conditional spectrum approach (CS) computed at each PGA interval up to 1 *g*.

For the PGA steps greater than 1 *g*, the set of GMs corresponding to 1 *g* was scaled up to 4 *g*. CS was defined using the results of the SHARE project by Woessner et al. (Woessner et al., 2015) and based on the results of the seismic hazard disaggregation for the site.

Note that all GMs were selected from the NGA strong ground motion database (Chiou et al., 2008) and the RESORCE (Akkar et al., 2014) database. For example, Figure 16 shows the spectra of the selected ground motions in the case of PGA = 1 *g*, which correspond to a returning period of 2475 years, the corresponding mean spectrum and the target spectrum. The magnitude and the source-to-site distance of the events of the selected GM are within 4.5 – 7.5 and 5-50 km, respectively. Note that this set of ground motions was also used in the seismic response analysis performed in the case of the conditional risk-based decision model.

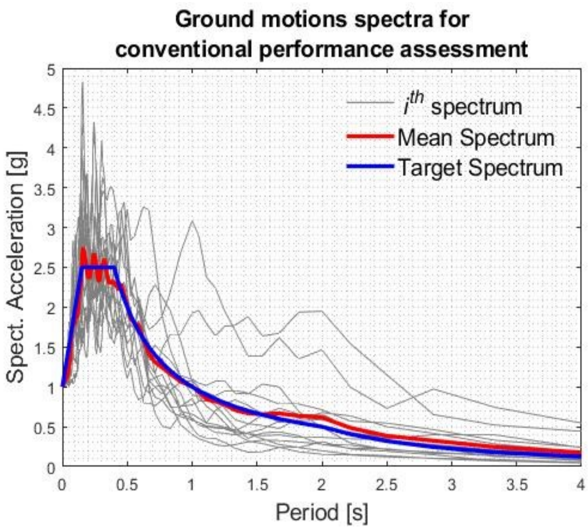

Figure 15: Acceleration spectra of selected ground motions for the two horizontal components, the corresponding mean and the target spectrum for conventional performance assessment.

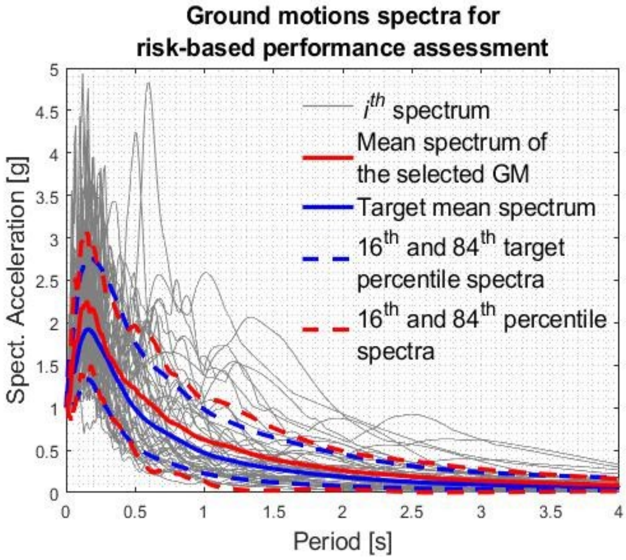

Figure 16: Ground motion spectra, mean and target spectrum at PGA = 1 g, which corresponds to a return period of 2475 years.

2.3.3 Performance assessment of the investigated tanks by the conventional decision model

The seismic performance of the non-code-conforming tanks and code-conforming tanks was evaluated by the conventional decision model presented in section 2.3.1.

Based on the results of response history analyses of non-code-conforming tanks, which were determined with consideration of the seven ground motions (section 2.3.2), it was observed that the mean value of the demand-to-capacity ratio of the non-code-conforming tank was greater than 1 for a full (90% filling level) or empty (0% filling level) tank (Figure 17 (a)). By considering the full or empty tank, it can be concluded that the seismic performance of the investigated non-code-conforming tank is not acceptable. However, the seismic performance of the code-conforming tanks was acceptable. The demand-to-capacity ratios were significantly less than one for all considered tank filling levels (Figure 17 (b)).

Because the demand-to-capacity ratios of the code-conforming tank are significantly less than 1, It could appear that the supporting structure of the code-conforming tanks is overdesigned. Such interpretation might be valid if only the conventional decision model is used for the evaluation of the performance assessment of structures. However, before making conclusions, we will first present the results of the evaluation of the seismic performance assessment of the investigated tanks using the conditional risk-based and risk-based decision models.

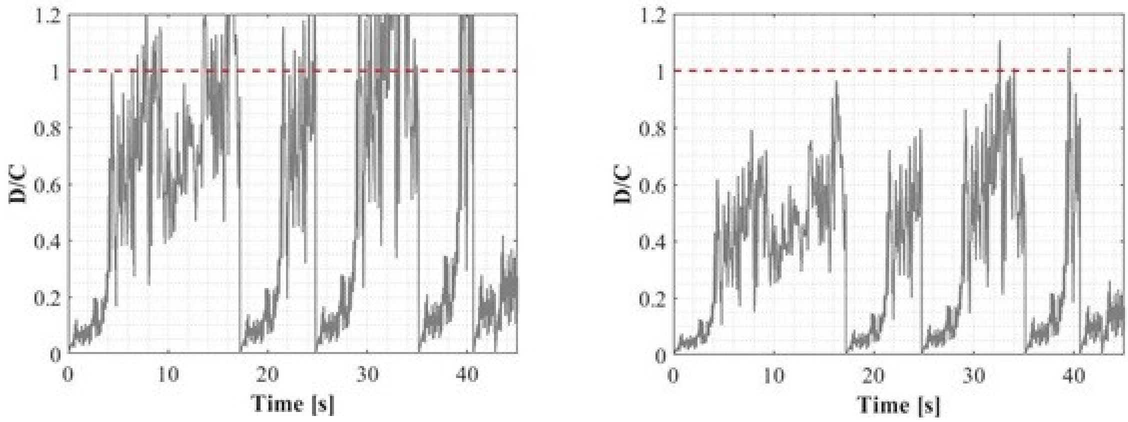

(a)

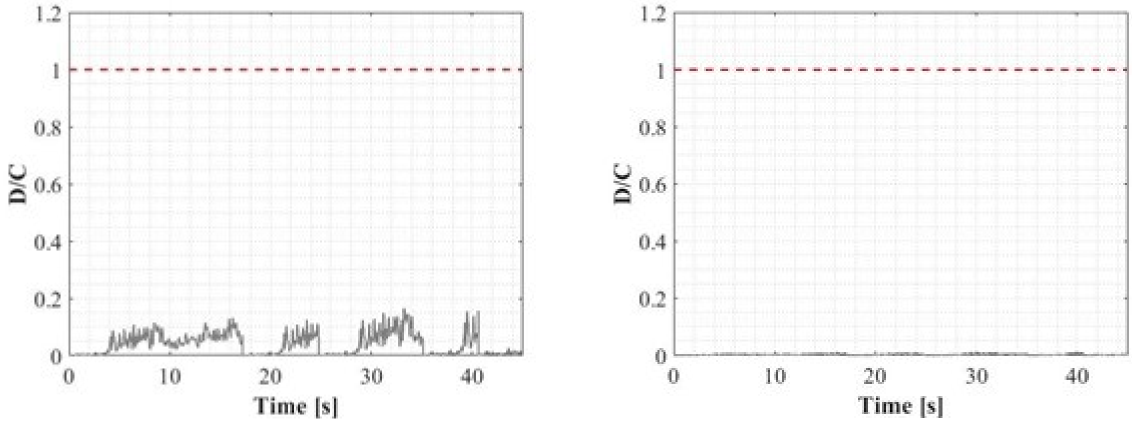

(b)

Figure 17: The demand-to-capacity ratio in the columns based on the averaging results of the seven ground motions in the case of (a) non-code-conforming tank and (b) code-conforming tank. Results are presented for full tanks (90% filling level, left) and empty tanks (0%, right).

2.3.4 Performance assessment of the investigated tanks by the conditional risk-based and risk-based decision models

The seismic performance assessment of the investigated tanks was evaluated using the conditional risk-based model and the risk-based decision model (section 2.3.1). The intermediate results of the latter decision model are fragility functions, which were evaluated by MSA using ground motions presented in section 2.3.2. Note that ground motions for the stripe corresponding to PGA=1 *g* (section 2.3.2) were used in the case of the conditional risk-based decision model because this intensity level corresponds to the return period of 2475 years. The considered filling levels of the tanks did not include the empty tank, because in this case, the scaling factors for the ground motions to reach the structural collapse would be too high.

The MSA was performed to evaluate the number of ground motions that caused the exceedance of the NC limit state. The parameters of the fragility function, i.e. the median PGA causing the exceedance of the NC limit state, μ, and the corresponding dispersion, β, were calculated by maximising the logarithm of the likelihood function in Eq. (3) (Baker, 2015):

$$\{\hat{\mu}, \hat{\beta}\} = \mathrm{argmax}_{\mu,\beta} \sum_{j=1}^{m} \left\{ ln \binom{n_j}{z_j} + z_j \, ln\, \Phi\left(\frac{ln\frac{x_j}{\mu}}{\beta}\right) + (n_j - z_j)\, ln\left(1 - \Phi\left(\frac{ln\frac{x_j}{\mu}}{\beta}\right)\right)\right\} \tag{3}$$

where m represents the number of stripes in MSA, n_j is the number of ground motions at intensity j, z_j is the number of ground motions exceeding NC LS at stripe j, and x_j is the seismic intensity at stripe j. The resulting estimators (i.e. $\hat{\mu}$ and $\hat{\beta}$) are presented in Table 7 for all investigated tanks and all considered tank filling levels. Note that for the sake of brevity they are termed as μ and β.

Figure 18 presents the results of MSA in the case of 90% of the filling level for non-code-conforming and code-conforming tanks, respectively. Each dot on the right-hand side of the LS dashed line represents the aforementioned z_j. Note that in the case of the non-code-conforming tank, for PGA=1 g, z_j corresponds to n_j, which is the total amount of GM at that stripe (50 GM).

The multiple stripe analysis was performed by scaling ground motions to PGA = 4 g, which required unrealistically high scaling factors of recorded ground motions. Thus the fragility functions were calculated by cutting off MSA results at PGA = 2 g for 90% of the filling level. Such an approach make it possible to check the bias in the evaluation of the fragility functions and the corresponding risk. However, no changes were observed in the fragility function of the non-code-conforming tank. For the code-conforming tank, the median PGA causing exceedance of NC limit state and the corresponding dispersion as presented in Table 7 were reduced, respectively, for about 10% and 20%. This reduction caused a slight anticlockwise rotation of the fragility function of the code-conforming tank around the point characterised by the probability of exceeding of about 0.16. However, such modification of fragility function causes only a minor impact on the annual probability of failure, as discussed elsewhere (Dolšek & Brozovič, 2016). In this particular case, the probability of exceeding was estimated to $1.6 \cdot 10^{-4}$ per year for maximum PGA cut off at 2 g instead of $1.7 \cdot 10^{-4}$ per year for PGA considered to 4 g. Thus, it was decided to use the fragility functions based on MSA associated with high scaling of ground motions, which may not be the case for some other structures or even some other tanks.

The corresponding fragility functions are presented in Figure 19 for all the investigated tanks and different tank filling levels. Reducing the tank filling level shifts the fragility functions to the right. This shift means the vulnerability of the supporting structure of tanks can be significantly reduced when the tanks are empty. However, this does not mean the tank is not vulnerable.

Table 7: Median PGA causing the exceedance of the NC limit state, μ, and the corresponding dispersion, β, for different filling levels of non-code-conforming and code conforming tanks.

Tank filling level	β		μ[g]	
	Non-code-conforming	Code-conforming	Non-code-conforming	Code-conforming
90% (full)	0.49	0.57	0.32	2.05
80%	0.53	0.54	0.34	2.23
70%	0.52	0.52	0.35	2.51
60%	0.50	0.48	0.40	2.75
50%	0.48	0.47	0.45	3.11
40%	0.44	0.42	0.55	3.50
30%	0.40	0.36	0.64	3.79
20%	0.37	0.26	0.69	4.22

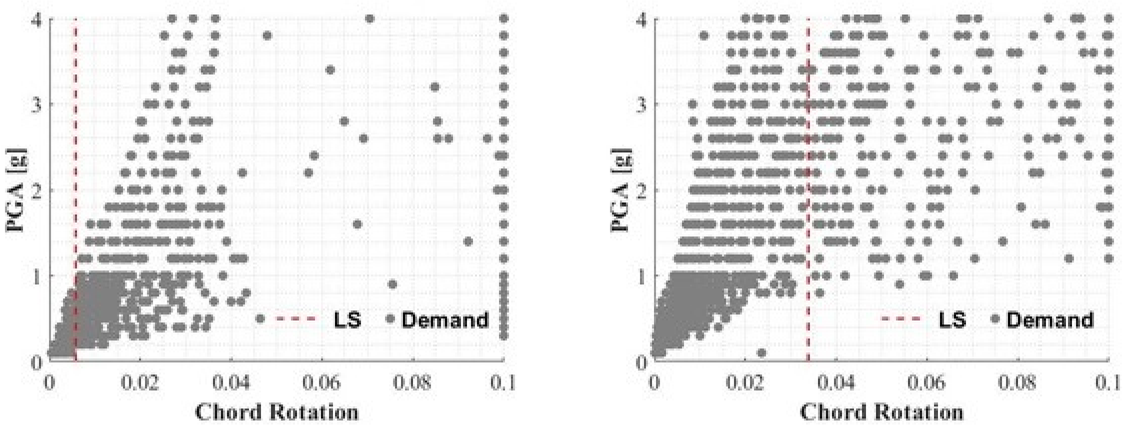

Figure 18: MSA results for (a) the non-code-conforming and (b) the code-conforming tank. Results are presented for full tanks (90% filling level).

Note that the demand points located at 0.1 of chord rotation in Figure 18 (a) and (b) represent the collapse which was observed at higher chord rotations. However, extremely high chord rotation values would have produced unreadable figures. Thus, it was decided to render them at 0.1 of chord rotation without affecting the results.

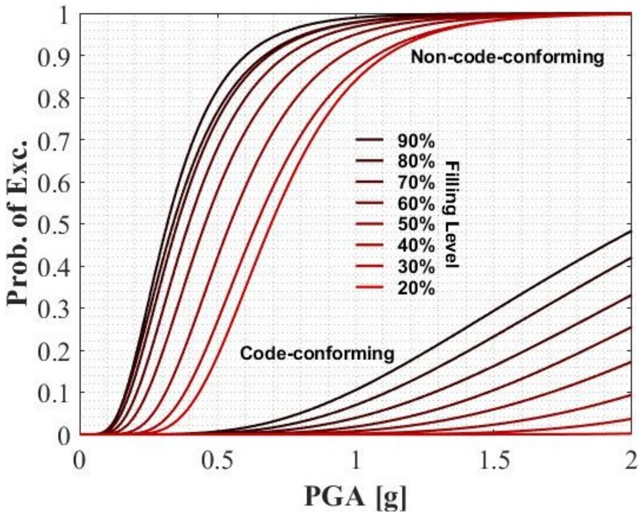

Figure 19: Fragility curves for non-code-conforming tank and code-conforming tank designed for DCH. Fragility curves are presented for different tank filling levels.

The ratios between the median PGA capacities causing the exceedance of the NC limit state in the case of the full and almost empty tank (i.e. 20% tank filling level) is about 2. The dispersion of PGA causing the NC limit state is in the case of the full tank about 0.5, regardless of the type of the tank. However, for low levels of tank filling (e.g. 20–40%), β is reduced to about 0.4. Quite similar trends for the β can be observed in the case of code-conforming tanks. As the filling level reduces, the dispersion reduces, too. The reason for this behaviour is twofold. First, by reducing the impulsive mass, the period is closer to zero. As a consequence, the dispersion of spectral acceleration reduces. Subsequently, this dispersion causes a reduction of dispersion of spectral acceleration, causing exceedance of limit state. Note that a smaller dispersion reveals an increase in the efficiency of the IM, as discussed by Jankovic et al. (Jankovic & Stojadinovic, 2004).

To facilitate the interpretation of the results, the ratios between the PGA corresponding to returning period of 475 years ($\mu_{475} = 0.5\ g$) and the median PGA causing the NC limit state are presented in Table 8. These ratios are not constant, and they are significantly greater than 1 in some cases of non-code-conforming tanks (see $\mu_{475}/\mu > 1$ Table 8). This means that the probability of exceeding the NC limit state in the case of the non-code-conforming tank is greater than 50%, if the tank filling level is more than 50%, and in the case of seismic action corresponding to returning period of 475 years.

The performance of the code-conforming tanks is significantly better. The observed ratios μ_{475}/μ are in the interval from about 0.3 to 0.1. The values of θ for code-conforming tanks are very high (from 2 to 4 g). The latest value of μ is even greater than the largest recorded PGA during the strongest earthquakes. However, it cannot be excluded that the NC limit state is exceeded for significantly lower values of PGA (see Figure 18).

According to the first risk-based decision model, the performance of the tank for the NC limit state is considered acceptable if there is less than 10% probability of exceeding the NC limit state at PGA = 1 g (i.e. returning period of 2475 years), which is, in this particular example, 200% of the PGA corresponding to return period of 475 years. Table 9 summarises the probability of exceeding the NC limit state calculated according to the single stripe analysis (SSA) referring to the PGA = 1 *g* (Figure 18) as defined in section 2.3.1. The presented probabilities are based on the ratio between the number of ground motions causing collapse and the number of all ground motions considered in the SSA.

The results in Table 9 show that the performance of the non-code-conforming tank is not acceptable because the resulting probability of exceeding the NC limit state given PGA = 1 *g* is significantly greater than 10% even when the tank is only 20% full (see Table 9). Regarding the code-conforming tank, in the case of lower filling levels, the probabilities of exceedance of the NC limit state given PGA = 1 g are negligible. The highest probability is observed in the case of 90% of the filling level, which is even greater than 10%.

The basic result of the risk analysis is the probability of exceeding a designated limit state for one year ($P_{f,LS}$), which can be calculated by a conventional risk equation (Eq. (1)). The results of the risk analysis in terms of probability of exceeding the NC limit state in one year are presented in Table 10. In addition, the probability of exceeding the NC limit state in 50 years ($P_{f,LS,50}$) is also presented. The corresponding acceptable probabilities for a period of 1 and 50 years are $2{\cdot}10^{-4}$ and 1%, respectively, as defined in section 2.3.1.

The risk of exceedance of the NC limit state in the case of the non-code-conforming tank is about 30% in 50 years if the tank is full. Such a risk is excessively high and requires immediate action to reduce it. However, the performance of the code-conforming tank can be considered acceptable, but the probability of exceeding the NC limit state in the case of the code-conforming tank is almost equal to the acceptable probability (i.e. $2{\cdot}10^{-4}$ in one year, 1% in 50 years). Thus, the supporting structure is not overdesigned, based on the conventional decision model and the risk-based decision model that employs the probability of exceeding the NC limit state for a given seismic intensity.

Table 8: The ratio between PGA corresponding to the return period of 475 years (μ_{475}) and the median PGA causing the exceedance of the NC limit state.

Tank filling level	μ_{475}/μ	
	Non-code-conforming	**Code-conforming**
90% (full)	1.56	0.24
80%	1.47	0.22
70%	1.43	0.20
60%	1.25	0.18
50%	1.11	0.16
40%	0.91	0.14
30%	0.78	0.13
20%	0.72	0.12

Table 9: Probability of exceedance of near-collapse LS for the PGA corresponding to a returning period of 2475 years.

Tank filling level	Probability of Exceedance of LS given PGA = 1.0 *g* ($P_{f,IM,LS}$)	
	Non-code-conforming	**Code-conforming**
	SSA	**SSA**
90% (full)	100%	14%
80%	98%	4%
70%	96%	[-]
60%	98%	[-]
50%	94%	[-]
40%	88%	[-]
30%	84%	[-]
20%	80%	[-]

Table 10: Probability of Exceedance of LS given a period of time.

Tank	Probability of Exceedance of LS given 1 year and 50 years			
	Non-code-conforming		**Code-conforming**	
	$P_{f,LS}$	$P_{f,LS,50}$	$P_{f,LS}$	$P_{f,LS,50}$
90% (full)	$7.5 \cdot 10^{-3}$	31.4%	$1.7 \cdot 10^{-4}$	0.9%
80%	$7.1 \cdot 10^{-3}$	29.7%	$1.3 \cdot 10^{-4}$	0.6%
70%	$6.4 \cdot 10^{-3}$	27.5%	$8.5 \cdot 10^{-5}$	0.4%
60%	$5.2 \cdot 10^{-3}$	23.0%	$5.8 \cdot 10^{-5}$	0.3%
50%	$4.0 \cdot 10^{-3}$	18.0%	$3.9 \cdot 10^{-5}$	0.2%
40%	$2.6 \cdot 10^{-3}$	12.3%	$2.4 \cdot 10^{-5}$	0.1%
30%	$1.8 \cdot 10^{-3}$	8.6%	$1.5 \cdot 10^{-5}$	0.1%
20%	$1.4 \cdot 10^{-3}$	6.9%	$8.8 \cdot 10^{-6}$	0.04%

2.4 Discussion

The damage to the almost-full and almost-empty tanks observed during the Kocaeli earthquake could be adequately simulated by the simplified non-linear models of the tanks, as presented and discussed in the Chapter. However, the simulations of seismic response of tanks, as considered in the study, are based on several assumptions. The study focused only on the seismic performance of the supporting structure against the NC limit state. Thus, the study's observations and conclusions may be partially affected by the definition of the limit states and the corresponding target probabilities of exceedance, the definition of which is currently a topic of discussion (e.g. (CEN, 2019)).

The results of the study also proved that the seismic performance of the non-code-conforming support structure of the elevated tank is not acceptable, regardless of the decision model used. Such an outcome indicated the need to urgently retrofit cases like the non-code-conforming tank.

The opposite can be concluded for the code-conforming tank, for which the seismic performance is acceptable, except in the case of the full tank evaluated using the conditional risk-based decision model. In this case, the probability of exceeding the near-collapse limit state was slightly higher than the target probability. This finding may be the consequence of the relatively simple evaluation of the probability of exceeding the near-collapse limit state given the seismic intensity. If this probability were evaluated from the fragility function, then the performance of the code-conforming tank would be acceptable even when evaluated using the conditional risk-based decision model.

Comparing the results of the three decision models applied to the code-conforming tank showed that the conventional decision model is not well calibrated to the target risk. The D/C ratios were significantly lower than the unity, which makes the support structure appear to be overdesigned. The results of the risk-based decision model proved that such a conclusion would be incorrect because the estimated probability of failure of the code-conforming tank was slightly less than the target value, which was set equal to 1% in 50 years. For this reason, the risk-based metrics provide much more information. However, they are computationally more demanding, especially in the case of the risk-based decision model, and can be considered only by using simplified non-linear models.

3 SIMPLIFIED MODEL FOR THE SIMULATION OF FLOATING ROOF IN STORAGE TANKS UNDER SEISMIC LOADING

The simplified model presented in the following was already proposed by (Shabani & Golzar, 2012). The authors derived the governing nonlinear equation of motion of the coupled floating roof–fluid system using Hamilton's variational principle, accounting for non-dissipative forces. In order to describe the floating roof–fluid Lagrangian the following assumptions were adopted:

- the tank's bottom plate and walls are supposed to be rigid;
- the fluid is assumed to be inviscid, incompressible and irrotational;
- the rocking of the rigid tank is not possible;
- no separation between fluid and roof is allowed (perfect contact);
- the floating roof is considered linear elastic.

In Figure 20 a sketch of a typical, single deck, floating roof in which the main parts are highlighted: the inner plate and the surrounding annular pontoon. Moreover, the polar reference system used in the development of the mathematical formulation is depicted.

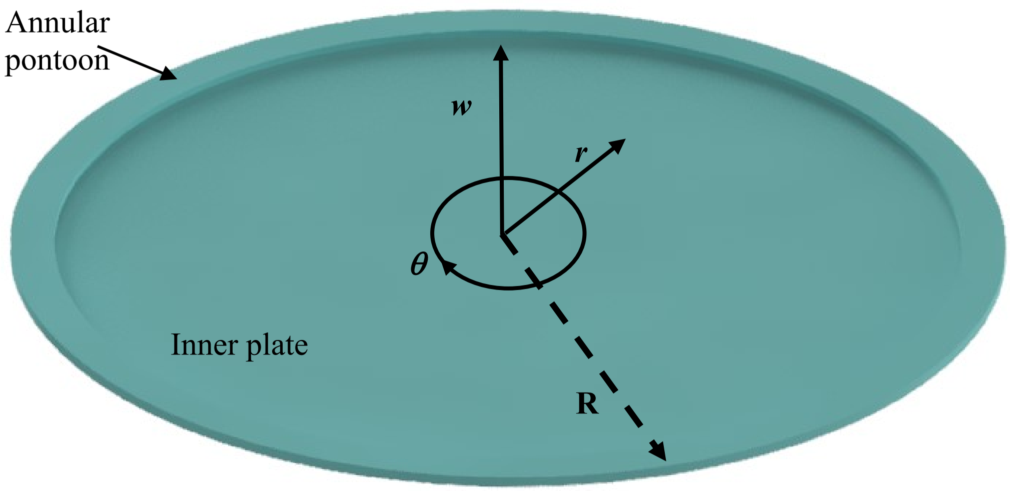

Figure 20: Sketch of a typical floating roof with the identification of the inner plate, the annular pontoon and the reference system used in the mathematical formulation.

Consequently, the Lagrangian of the system assumes the following form:

$$\int_{t_1}^{t_2} L\,dt = \int_{t_1}^{t_2} (T - U + F)\,dt \tag{4}$$

where *T, U* and *F* are the kinetic energy of the floating roof, the strain energy of the floating roof and the fluid Lagrangian. The fluid Lagrangian is considered as the energy of external forces. *T* simply represents the energy needed to accelerate the floating roof mass from the rest state to a given velocity:

$$T = \frac{1}{2} \int m\, \dot{w}^2(t, r, \theta)\, dS_v \tag{5}$$

where S_v is the floating roof surface defined by the floating roof radius r, ranging from 0 to R, and θ is the angular coordinate in a polar reference system, ranging from 0 to 2π. The variable m is the mass per unit area and w is the vertical displacement of the floating roof plate, which, it is assumed, can be approximately simulated by the linear combination of time-invariant interpolation functions (Shabani & Golzar, 2012):

$$w(t, r, \theta) = \sum_{i=1}^{I} B_i(t)\, \xi_i(r, \theta) \tag{6}$$

where ξ_i is the *i-th* interpolation function (see Eqs. (16) – (17)), $B_i(t)$ is the corresponding time-dependent coefficient (i.e. displacement in generalized coordinates), and I refers to the number of considered interpolation functions. Modal shapes of a free-edge thin circular plate have been assumed for the interpolation functions (Itao & Crandall, 1979).

U from Eq. (7) represents the energy stored by the floating roof due to its deformation. By assuming the linear elastic response of the floating roof, its strain energy can be defined as (Shabani & Golzar, 2012):

$$U = \int_0^{2\pi} \int_0^{R} \int_{-\frac{h}{2}}^{\frac{h}{2}} (\sigma_{rr}\varepsilon_{rr} + \sigma_{\theta\theta}\varepsilon_{\theta\theta} + \sigma_{r\theta}\varepsilon_{r\theta})\, r\, dz\, dr\, d\theta \tag{7}$$

where σ_{rr}, $\sigma_{\theta\theta}$, $\sigma_{r\theta}$ are the stress tensor components of the floating roof deck in polar coordinates, ε_{rr}, $\varepsilon_{\theta\theta}$ and $\varepsilon_{r\theta}$ are the corresponding strain values, and *R* and *h* are the floating roof radius and thickness, respectively.

F is the fluid Lagrangian, which represents the external energy of the floating roof. Therefore, it accounts for the kinetic energy due to the movement of the coupled system floating roof–fluid and the potential energy due to the vertical fluid wave displacement. The fluid Lagrangian computed at the floating roof–fluid interface can be expressed in polar coordinates as introduced by (Shabani & Golzar, 2012):

$$F = \int_0^{2\pi} \int_0^R \rho \left[-\frac{1}{2} \left(\frac{\partial \phi}{\partial z} \right)_{z=H} \phi + \frac{\partial w}{\partial t} \phi - \frac{g}{2} w^2 \right] r \, dr d\theta \tag{8}$$

where ρ is the fluid density, H is the fluid height (filling level), w is the flexural displacement of the floating roof introduced in Eq. (6), g is the gravity acceleration, and ϕ is the potential function of the fluid. The first two terms in square brackets represent the kinetic energy of the fluid at the surface level, while the last term represents the potential energy of the surface. The potential function of the fluid ϕ must satisfy the Laplace equation for an irrotational fluid:

$$\nabla^2 \phi = 0 \tag{9}$$

The function must also satisfy the related boundary conditions:

$$\frac{\partial \phi}{\partial z}_{z=H} = \frac{\partial w}{\partial t} \qquad \text{on the fluid-floating roof contact surface} \tag{10}$$

$$\frac{\partial \phi}{\partial z}_{z=0} = 0 \qquad \text{on the bottom plate} \tag{11}$$

$$\frac{\partial \phi}{\partial r}_{r=R} = \dot{x}_g \cos \theta \qquad \text{on the tank wall} \tag{12}$$

where $\dot{x}_g$ is the ground velocity due to the ground motion. The boundary condition in Eq. (10) reflects the assumption of perfect contact between the fluid and floating roof, while Eq. (12) derives from the assumption of the rigid tank wall. Under these premises, the fluid potential can be derived as (Shabani & Golzar, 2012):

$$\phi(t, r, \theta) = \left[r\dot{x}_g + \sum_{i=1}^{I} A_k(t) \frac{J_1\left(\frac{\epsilon_i}{R} r\right) \cosh\left(\frac{\epsilon_i}{R} z\right)}{J_1(\epsilon_i) \cosh\left(\frac{\epsilon_i}{R} H\right)} \right] \cos \theta \tag{13}$$

where J_1 is the Bessel function of the first kind of order one, $A_i(t)$ is the time-dependent modal amplitude, z is the vertical coordinate for the fluid (zero at the bottom tank plate and equal to H at the free surface height) and ϵ_i is the *i-th* root of the first derivative of the Bessel function of the first kind of order one (as in Eq. 29).

By applying Hamilton's variational principle to the Lagrangian of the system (Eq. (4)), the governing non-linear equation of motion of the coupled floating roof – fluid system can be obtained (Shabani & Golzar, 2012):

$$\left(\boldsymbol{P} + \rho \boldsymbol{T} \boldsymbol{S}^{-1} \boldsymbol{T}^t \right) \ddot{\boldsymbol{B}} + (\boldsymbol{Q} + \rho g \boldsymbol{U}) \boldsymbol{B} + \boldsymbol{\chi} \boldsymbol{B}^3 = \rho \boldsymbol{G} \ddot{x}_g \tag{14}$$

where $\boldsymbol{P}$, $\boldsymbol{Q}$, $\boldsymbol{S}$ and $\boldsymbol{\chi}$ are matrices of order $I \times I$ where I represents the number of considered modes and $\boldsymbol{G}$ is a vector of size I. The components of $\boldsymbol{G}$ reflect the importance of each interpolation function, $\boldsymbol{P}$ represents the contribution of the mass of the floating roof to the mass of the system, $\boldsymbol{TS^{-1}T^{t}}$ contributes to the fluid mass due to the sloshing, $\boldsymbol{Q}$ is the floating roof stiffness matrix and $\boldsymbol{U}$ can be interpreted as an additional stiffness due to the fluid. $\boldsymbol{P}$, $\boldsymbol{Q}$, $\boldsymbol{S}$, $\boldsymbol{G}$ and $\boldsymbol{\chi}$ are composed of different elements which are described in detail in the following.

$\boldsymbol{P}$ is the first part of the first term of Eq. (14) and represents the floating roof mass matrix which has the following indicial form:

$$P_{ij} = -m \int_0^{2\pi} \int_0^R \xi_i \, \xi_j \, r \, dr d\theta \tag{15}$$

where m stands for the floating roof unit mass and ξ are interpolation functions used to describe the deformed shape of the floating roof. In this particular case, the interpolation functions are the mode shape functions of the floating roof in the air (Itao & Crandall, 1979):

$$\xi_{0,1}(r,\theta) = 2\frac{r}{R} cos\,\theta \tag{16}$$

$$\xi_{j,p}(r,\theta) = D_{j,p}\left[J_p\left(\lambda_{j,p}\, r/R\right) + E_{j,p} I_p\left(\lambda_{j,p}\, r/R\right)\right]\cos(p\theta) \tag{17}$$

where R is the floating roof radius, the index j represents the nodal circumference number, and p is the nodal diameter number. A few examples of modal shapes are presented in Figure 21.

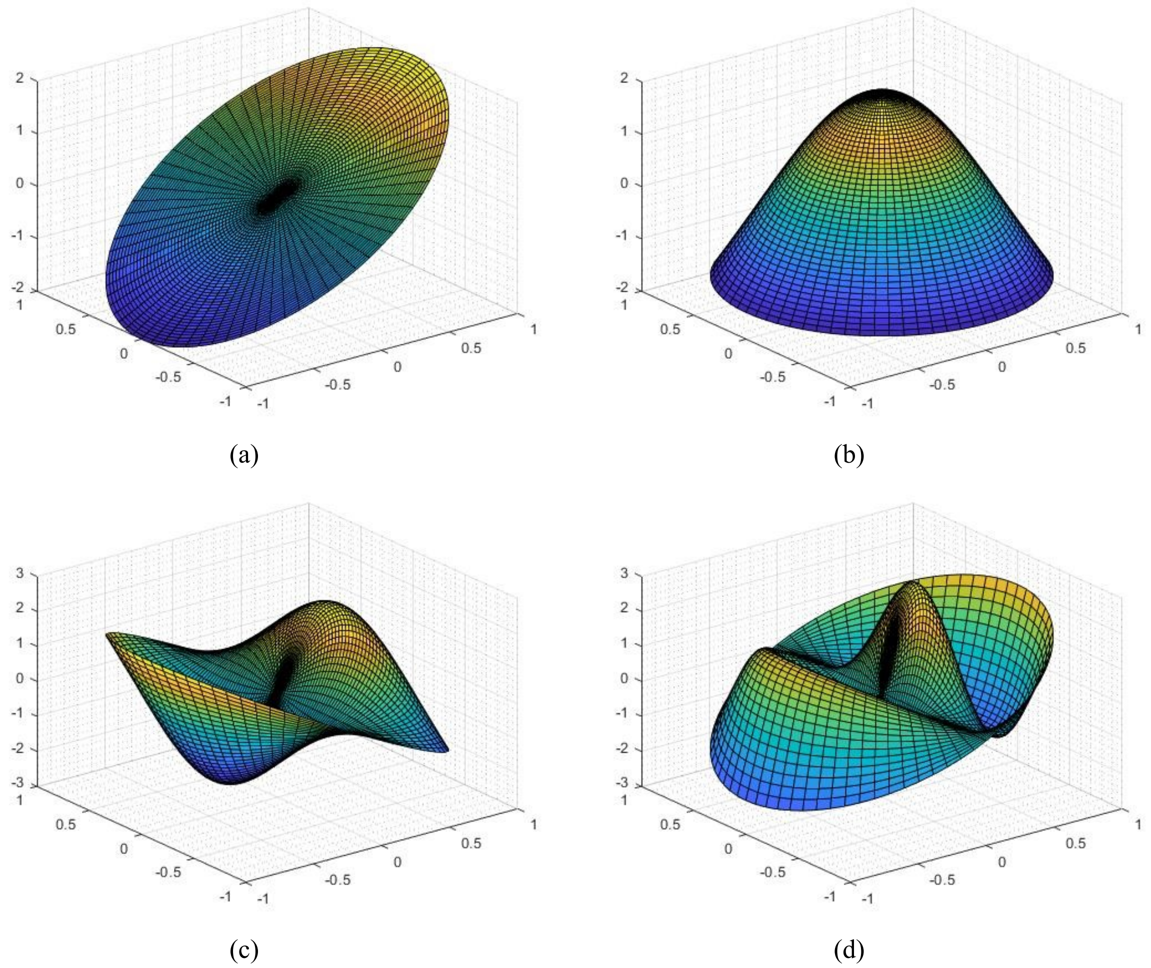

Figure 21: Free edge circular plate modal shapes (a) p=1 and j=0 (b) p=0 and j=1 (c) p=1 and j=1 (d) p=1 and j=2.

However, as highlighted in (Shabani, 2013), it is worth noting that only rigid and elastic radial mode shapes are considered in the formulation. Hence, subscript p is equal to 1 while subscript j=0, 1, …, n. In this particular case, when p = 1 and j = 0, (see Eq.(16)), the free edge plate experiences a rigid-body mode with zero frequency, which means rigid rotation about the diameter, while the other modal shapes are described by Eq. (17), (Itao & Crandall, 1979). In this respect, for simplicity, subscript p will be removed by notation since it will be assumed to be always equal to 1.

In Eq. (17) the frequency parameter ($\lambda_{j,p}$) and the mode shape parameter ($E_{j,p}$) are obtained by the eigenvalue problem while the amplitude parameter ($D_{j,p}$) is derived by imposing the normalization as explained in the following: J_p and I_p are Bessel functions of the first kind of order p and a modified Bessel function of order p, respectively.

The solution of the eigenvalue problem of a thin plate with free edges as boundary conditions makes it possible to compute $\lambda_{j,p}$ and $E_{j,p}$ (Itao & Crandall, 1979):

$$\begin{cases} E_{j,p} = \frac{\lambda_{j,p}^2 J_p(\lambda_{j,p})+(1-\nu)[\lambda_{j,p} J_p'(\lambda_{j,p})-p^2 J_p(\lambda_{j,p})]}{\lambda_{j,p}^2 I_p(\lambda_{j,p})-(1-\nu)[\lambda_{j,p} I_p'(\lambda_{j,p})-p^2 I_p(\lambda_{j,p})]} \\ E_{j,p} = \frac{\lambda_{j,p}^3 J_p'(\lambda_{j,p})+p^2(1-\nu)[\lambda_{j,p} J_p'(\lambda_{j,p})-J_p(\lambda_{j,p})]}{\lambda_{j,p}^3 I_p'(\lambda_{j,p})-p^2(1-\nu)[\lambda_{j,p} I_p'(\lambda_{j,p})-I_p(\lambda_{j,p})]} \end{cases} \quad (18)$$

The amplitude parameter $D_{j,p}$ from Eq. (17) is computed by imposing the shape function to be normal with respect of the mass Eq. (19), (Itao & Crandall, 1979):

$$\int_0^{2\pi} \int_0^R \rho h \xi_{j,p}^2 (r,\theta) r \, dr d\theta = \pi \rho h R^2 \quad (19)$$

where ρ is the plate density, h is the plate thickness, and R is the plate radius. Substituting Eq. (17) in the left-hand side part of Eq. (19) and integrating over θ leads to Eq. (20):

$$\int_0^{2\pi} \rho h D_{j,p}^2 \left\{\left[J_p\left(\lambda_{j,p}\, r/R\right) + E_{j,p} I_p\left(\lambda_{j,p}\, r/R\right)\right]\right\}^2 \cos^2(p\theta)\, r \, d\theta = \rho h D_{j,p}^2 \left\{\left[J_p\left(\lambda_{j,p}\, r/R\right) + E_{j,p} I_p\left(\lambda_{j,p}\, r/R\right)\right]\right\}^2 r \left(\pi + \frac{\sin(4p\pi)}{4p}\right) \quad (20)$$

Because p is always an integer, Eq. (20) becomes:

$$\int_0^{2\pi} \rho h D_{j,p}^2 \left\{\left[J_p\left(\lambda_{j,p}\, r/R\right) + E_{j,p} I_p\left(\lambda_{j,p}\, r/R\right)\right]\right\}^2 \cos^2(p\theta)\, r \, d\theta = \pi \rho h D_{j,p}^2 \left\{\left[J_p\left(\lambda_{j,p}\, r/R\right) + E_{j,p} I_p\left(\lambda_{j,p}\, r/R\right)\right]\right\}^2 r \quad (21)$$

The right-hand side of Eq. (21) can now be integrated (for $p \geq 0$) with respect to variable r (Eq. (22)). It is worth noting that, since $\pi, \rho, h, D_{j,p}^2$ are r-independent, they can be extracted from the integral.

$$\pi \rho h D_{j,p}^2 \int_0^R \left\{\left[J_p\left(\lambda_{j,p}\, r/R\right) + E_{j,p} I_p\left(\lambda_{j,p}\, r/R\right)\right]\right\}^2 r \, dr = \pi \rho h D_{j,p}^2 R^2 \frac{1}{2\lambda_{j,p}} \Big\{-E_{j,p}^2 \lambda_{j,p} I_{p-1}^2\left(\lambda_{j,p}\right) + E_{j,p}^2 \lambda_{j,p} I_p^2\left(\lambda_{j,p}\right) + \lambda_{j,p} J_{p-1}^2\left(\lambda_{j,p}\right) + \lambda_{j,p} J_p^2\left(\lambda_{j,p}\right) + 2E_{j,p} I_{p-1}\left(\lambda_{j,p}\right) \left[p E_{j,p} I_p\left(\lambda_{j,p}\right) + J_p\left(\lambda_{j,p}\right) - 2J_{p-1}\left(\lambda_{j,p}\right)\left(E_{j,p} I_p\left(\lambda_{j,p}\right) + p J_p\left(\lambda_{j,p}\right)\right)\right]\Big\} \quad (22)$$

The right-hand side of Eq. (22) can be written in a simplified manner (Eq. (23)):

$$\pi \rho h D_{j,p}^2 R^2 \frac{1}{2\lambda_{j,p}} \Big\{-E_{j,p}^2 \lambda_{j,p} I_{p-1}^2\left(\lambda_{j,p}\right) + E_{j,p}^2 \lambda_{j,p} I_p^2\left(\lambda_{j,p}\right) + \lambda_{j,p} J_{p-1}^2\left(\lambda_{j,p}\right) + \lambda_{j,p} J_p^2\left(\lambda_{j,p}\right) + 2E_{j,p} I_{p-1}\left(\lambda_{j,p}\right) \left[p E_{j,p} I_p\left(\lambda_{j,p}\right) + J_p\left(\lambda_{j,p}\right) - 2J_{p-1}\left(\lambda_{j,p}\right)\left(E_{j,p} I_p\left(\lambda_{j,p}\right) + p J_p\left(\lambda_{j,p}\right)\right)\right]\Big\} = M D_{j,p}^2 X \quad (23)$$

where M and X are defined by Eq. (24) and Eq. (25), respectively. It is worth noting that M represents the total mass of the floating roof.

$$M = \pi \rho h R^2 \quad (24)$$

$$X = \frac{1}{2\lambda_{j,p}}\Big\{-E_{j,p}^2\lambda_{j,p}I_{p-1}^2(\lambda_{j,p}) + E_{j,p}^2\lambda_{j,p}I_p^2(\lambda_{j,p}) + \lambda_{j,p}J_{p-1}^2(\lambda_{j,p}) + \lambda_{j,p}J_p^2(\lambda_{j,p}) +$$
$$2E_{j,p}I_{p-1}(\lambda_{j,p})\Big[pE_{j,p}I_p(\lambda_{j,p}) + J_p(\lambda_{j,p}) - 2J_{p-1}(\lambda_{j,p})\Big(E_{j,p}I_p(\lambda_{j,p}) + pJ_p(\lambda_{j,p})\Big)\Big]\Big\} \tag{25}$$

Imposing the normalization with respect to the total plate mass, it is now possible to solve Eq. (23) with respect to the amplitude parameter $D_{j,p}^2$. Eq. (26) will provide two opposite values. For the amplitude parameter, the positive value must be selected.

$$MD_{j,p}^2X = M \tag{26}$$

The matrix $\rho\boldsymbol{T}\boldsymbol{S}^{-1}\boldsymbol{T}^{t}$ in the second part of the first term of Eq. (14) represents the fluid mass excited during the convective motion. Their indicial forms are provided by the following equations:

$$S_{ij} = \int_0^R \left[\frac{\epsilon_j J_1\left(\frac{\epsilon_j}{R}r\right)}{2RJ_1(\epsilon_j)}\tanh\left(\frac{\epsilon_j}{R}H\right)\frac{J_1\left(\frac{\epsilon_i}{R}r\right)}{J_1(\epsilon_i)} + \frac{\epsilon_i J_1\left(\frac{\epsilon_i}{R}r\right)}{2RJ_1(\epsilon_i)}\tanh\left(\frac{\epsilon_i}{R}H\right)\frac{J_1\left(\frac{\epsilon_j}{R}r\right)}{J_1(\epsilon_j)}\right] r\,dr \tag{27}$$

$$T_{ij} = \int_0^{2\pi}\int_0^R \xi_i \frac{J_1\left(\frac{\epsilon_j}{R}r\right)}{J_1(\epsilon_j)}\cos\theta\, r\, drd\theta \tag{28}$$

where J_1 is a Bessel function of the first kind of order one and ϵ_i is the i^{th} root of the first derivative of a Bessel function of the first kind of order one, as in Eq. (29).

$$J'_1(\epsilon_i) = 0 \tag{29}$$

Matrices $\boldsymbol{Q}$ and $\boldsymbol{U}$ in Eq. (14) represent the stiffness matrix of the floating roof and the contribution of the fluid to the stiffness of the coupled floating roof–fluid system, respectively, whose indicial form is defined in Eq. (30) and (31).

$$Q_{ij} = \frac{Eh^3}{12(1-\nu^2)}\int_0^{2\pi}\int_0^R \Big(\xi_{i,rr}\xi_{j,rr} + \frac{\nu}{r^2}\xi_{i,rr}\xi_{j,\theta\theta} + \frac{\nu}{r}\xi_{j,r}\xi_{i,rr} + \frac{1}{r^4}\xi_{j,\theta\theta}\xi_{i,\theta\theta} + \frac{1}{r^3}\xi_{j,\theta\theta}\xi_{i,r} +$$
$$\frac{1}{r^3}\xi_{j,r}\xi_{i,\theta\theta} + \frac{1}{r^2}\xi_{j,r}\xi_{i,r} + \frac{\nu}{r^2}\xi_{j,rr}\xi_{i,\theta\theta} + \frac{\nu}{r}\xi_{j,rr}\xi_{i,r}\Big) r\, drd\theta + \frac{Eh^3}{24(1+\nu)}\int_0^{2\pi}\int_0^R \Big(\frac{4}{r^2}\xi_{j,r\theta}\xi_{i,r\theta} -$$
$$\frac{4}{r^3}\xi_{j,r\theta}\xi_{i,\theta} - \frac{4}{r^3}\xi_{j,\theta}\xi_{i,r\theta} + \frac{4}{r^4}\xi_{j,\theta}\xi_{i,\theta}\Big) r\, drd\theta \tag{30}$$

$$U_{ij} = \int_0^{2\pi}\int_0^R \xi_i\xi_j r\ drd\theta \tag{31}$$

E and ν are the Young modulus and the Poisson ratio of the floating roof material, respectively, while h is the floating roof thickness. ξ is the interpolating function of Eq. (16) or Eq. (15), and subscripts after the comma represent the derivative with respect to the subscripts themselves.

$\boldsymbol{\chi}$ matrix in Eq. (14) is defined by Eq. (32). It accounts for the large deflection of the floating roof using a cubic stiffness term (Shabani & Golzar, 2012).

$$\chi_{lmni} = \frac{Eh}{1-\nu^2}\int_0^{2\pi}\int_0^R \Big(\sum_{j=1}^{I}\eta_{j,r}\Psi_{lmj}\xi_{n,r}\xi_{i,r} + \frac{1}{2}\xi_{l,r}\xi_{m,r}\xi_{n,r}\xi_{i,r} + \frac{\nu}{2r^2}\xi_{l,\theta}\xi_{m,\theta}\xi_{n,r}\xi_{i,r}\sum_{j=1}^{I}\eta_{j,r}\Psi_{lmj}\xi_{n,r}\xi_{i,r} + \frac{1}{2}\xi_{l,r}\xi_{m,r}\xi_{n,r}\xi_{i,r} + \frac{\nu}{2r^2}\xi_{l,\theta}\xi_{m,\theta}\xi_{n,r}\xi_{i,r} + \frac{\nu}{r}\sum_{j=1}^{I}\eta_j\Psi_{lmj}\xi_{n,r}\xi_{i,r} + \frac{1}{r^3}\sum_{j=1}^{I}\eta_j\Psi_{lmj}\xi_{n,\theta}\xi_{i,\theta} + \frac{1}{2r^4}\xi_{l,\theta}\xi_{m,\theta}\xi_{n,\theta}\xi_{i,\theta} + \frac{\nu}{r^2}\sum_{j=1}^{I}\eta_{j,r}\Psi_{lmj}\xi_{n,\theta}\xi_{i,\theta} + \frac{\nu}{2r^2}\xi_{l,r}\xi_{m,r}\xi_{n,\theta}\xi_{i,\theta}\Big)r\,drd\theta + \frac{Eh}{2(1+\nu)}\int_0^{2\pi}\int_0^R \Big(\frac{1}{r^2}\sum_{j=1}^{I}\eta_{j,\theta}\Psi_{lmj}\xi_{n,\theta}\xi_{i,r} + \frac{1}{r^2}\sum_{j=1}^{I}\eta_{j,\theta}\Psi_{lmj}\xi_{n,r}\xi_{i,\theta} + \frac{1}{r^2}\xi_{l,r}\xi_{m,\theta}\xi_{n,\theta}\xi_{i,r} + \frac{1}{r^2}\xi_{l,r}\xi_{m,r}\xi_{n,\theta}\xi_{i,\theta}\Big)r\,drd\theta \tag{32}$$

All the terms in Eq. (32) have the same meaning as the aforementioned terms. The only novelties are represented by the introduction of Eq. (33) and the terms Ψ_{lmj} presented in Eq. (34).

$$\eta_i(r,\theta) = \sin\left(\lambda_i\frac{r}{R}\right)\cos\theta \tag{33}$$

Eq. (37), similarly to Eqs. (20) and (21), is an interpolation function, which is used to describe the radial deflection in the midplane of the floating roof. Ψ_{lmj} can instead be calculated using Eqs. (35) and (36).

$$\sum_{j=1}^{J} -\left[H_{ij}\right]^{-1}\sum_{l=1}^{I}\sum_{k=1}^{I}\Gamma_{lkj}B_lB_k = \sum_{l=1}^{I}\sum_{k=1}^{I}\Psi_{lkj}B_lB_k \tag{34}$$

$$H_{ij} = \frac{Eh}{1-\nu^2}\int_0^{2\pi}\int_0^R\left(\eta_{j,r}\eta_{i,r} + \frac{\nu}{r}\eta_j\eta_{i,r} + \frac{1}{r^2}\eta_j\eta_i + \frac{\nu}{r}\eta_{j,r}\eta_i\right)r\,drd\theta + \frac{Eh}{2(1+\nu)}\int_0^{2\pi}\int_0^R\frac{1}{r^2}\eta_{j,\theta}\eta_{i,\theta}r\,drd\theta \tag{35}$$

$$\Gamma_{lki} = \frac{Eh}{1-\nu^2}\int_0^{2\pi}\int_0^R\left(\frac{1}{2}\xi_{l,r}\xi_{k,r}\eta_{i,r} + \frac{\nu}{2r^2}\xi_{l,\theta}\xi_{k,\theta}\eta_{i,r} + \frac{1}{2r^3}\xi_{l,\theta}\xi_{k,\theta}\eta_i + \frac{\nu}{2r}\xi_{l,r}\xi_{k,r}\eta_i\right)r\,drd\theta + \frac{Eh}{2(1+\nu)}\int_0^{2\pi}\int_0^R\frac{1}{r^2}\xi_{l,r}\xi_{k,\theta}\eta_{i,\theta}r\,drd\theta \tag{36}$$

The last term of Eq. (14) is the vector $\boldsymbol{G}$. It is described in Eq. (37), where all the terms have already been described.

$$G_i = \int_0^{2\pi}\int_0^R \xi_i\, r^2\cos\theta\;drd\theta \tag{37}$$

Eq. (14) can be seen as a conventional form of the equation of motion, which is expressed as

$$\boldsymbol{M}\ddot{\boldsymbol{B}} + \boldsymbol{K}\boldsymbol{B} + \boldsymbol{\chi}\boldsymbol{B}^{\boldsymbol{3}} = \rho\boldsymbol{G}\ddot{x}_g \tag{38}$$

where $\boldsymbol{M}$ and $\boldsymbol{K}$ are expressed as

$$\boldsymbol{M} = \boldsymbol{P} + \rho\boldsymbol{T}\boldsymbol{S}^{-\boldsymbol{1}}\boldsymbol{T}^{\boldsymbol{t}} \tag{39}$$

$$\boldsymbol{K} = \boldsymbol{Q} + \rho g\boldsymbol{U} \tag{40}$$

Since Eq. (14) is derived according to Hamilton's principle, the effect of non-conservative forces is not accounted for in the governing nonlinear equation of motion (Eq. (38)). This can be overcome by adding the effect of viscous damping using the Rayleigh damping model (Shabani, 2013). As a consequence, the damping matrix $\boldsymbol{C}$ (Eq. (41)) is introduced as a linear combination of matrices $\boldsymbol{M}$ and $\boldsymbol{K}$:

$$\boldsymbol{C} = \alpha \boldsymbol{M} + \beta \boldsymbol{K} \tag{41}$$

where coefficient α and β are calculated according to the Rayleigh damping model by using a damping ratio ζ. Eq. (38) can then be expressed as

$$\boldsymbol{M}\ddot{\boldsymbol{B}} + \boldsymbol{C}\dot{\boldsymbol{B}} + \boldsymbol{K}\boldsymbol{B} + \boldsymbol{\chi}\boldsymbol{B}^{\mathbf{3}} = \rho \boldsymbol{G}\ddot{x}_g \tag{42}$$

Eq. (42) represents the differential equation of motion for simulating the seismic behaviour of the floating roof in generalized coordinates $\boldsymbol{B}$.

The solution of the equation of motion has been derived by using a Matlab-based code (MathWorks, 2012). The workflow of the developed software tool is presented in Figure 22. The input data related to the tank, the roof and the content are the number of considered modes I [-], fluid height H [m], Poisson's ratio of floating roof material v, tank radius R [m], floating roof thickness h [m], Young's modulus of floating roof material E [N/m^2], the density of floating roof material ρ_r [kg/m^3], the density of fluid ρ [kg/m^3], the critical damping ratio ζ and gravity acceleration g [m/s^2]. Input data are received by the matrix function (MF), which is a function designed to calculate matrices $\boldsymbol{M}, \boldsymbol{C}, \boldsymbol{K}, \boldsymbol{\chi}$ and the vector $\boldsymbol{G}$ from Eq. (42). However, to calculate all the presented matrices, the coefficients $\lambda_{j,p}, E_{j,p}, D_{j,p}$and ϵ_i (Eqs. (18) – (26) – (29)) has to be defined. For this reason, the MF function calls the coefficient function (CF), which returns all necessary coefficients.

The output of the MF function ($\boldsymbol{M}, \boldsymbol{C}, \boldsymbol{K}, \boldsymbol{\chi}$ and the vector $\boldsymbol{G}$**)** is the input for the run function (RF), which composes Eq. (42). In this step, it is necessary to also define the seismic action in terms of the ground motion acceleration history ($\ddot{x}_g$ in [g]) with its time-sampling interval (dt) in seconds.

To calculate the response history of vertical displacements (Eq. (6)), the location of the roof's vertical displacement has to be defined in polar coordinates. The variable *RPos* [m] represents the radial coordinate from 0 to floating roof radius R, and *Pos* [rad] refers to the angular coordinate ranging from 0 to 2π. Positive values of kinematical quantities are defined on the direction π–0 (i.e. the direction 180º–0º (see Figure 25 (a)).

Finally, the RF composes Eq. (42) and calls the equation solver function (ESF) which solves it. The ESF function incorporates ode45, a built-in Matlab differential equations solver (Shampine & Reichelt, 1998) which is based on the work of Dormand et al. (Dormand & Prince, 1986). The ESF function returns the vector of generalized displacements $\boldsymbol{B}$ for each time step of the ground motion. The output is then post-processed within the RF to calculate the vertical displacement of the floating roof w according to Eq. (6). Eq. (6) provides the vertical displacement history's coupling time-dependent coefficients $B_i(t)$ (i-th element of column vector $\boldsymbol{B}$) and the interpolation functions ξ_i (Eqs. (16) – (17)). Finally, the vertical displacement history of the floating roof at the required position is calculated and plotted.

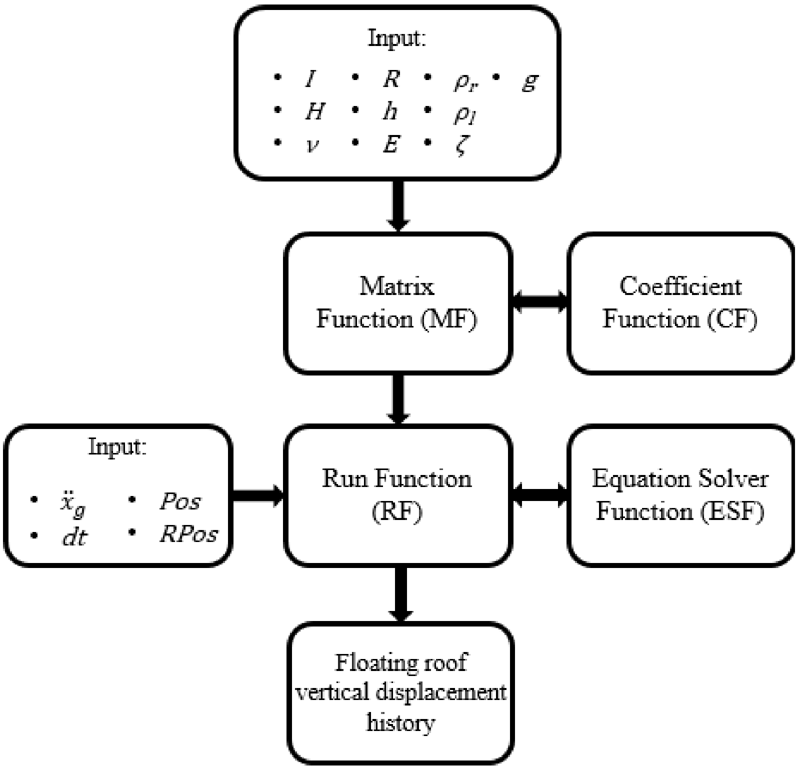

Figure 22: Software tool workflow.

4 VALIDATION OF THE SIMPLIFIED MODEL BY A REFINED FE MODEL AND THE SHAKING TABLE TEST

An overview of a scaled steel storage tank with a floating roof, which had been tested on the shake table (CEA, 2017), is described first. Then the refined FE model of the liquid storage tank with a floating roof is developed, and numerical outcomes compared to experimental data and simplified model results. Furthermore, a parametric study aiming to highlight the most relevant simplified model parameters is presented. Finally, the results of the present Chapter are summarized and discussed.

4.1 Shaking table test campaign of unanchored tank equipped with a floating roof

An extensive experimental campaign was performed in 2017 within the European project INDUSE-2-SAFETY in cooperation with CEA EMSI laboratory (CEA, 2017). In particular, shaking table tests have been carried out on two steel storage tank typologies (CEA, 2017). However, attention was paid only to the unanchored broad steel storage tank mock-up with a floating roof, (Figure 23 (a)), which has a diameter of 3 m and a height of 0.868 m. The mock-up was a reduced-scale model with a scaling factor of 1/18. The tank wall was made of SS304 steel with a uniform thickness of 1 mm. The same material with the same thickness was also used for the bottom plate, which was welded to the cylindrical wall. The tank was filled with water up to 90% of the tank height (0.781 m) with a freeboard approximately 8.5 cm thick. The mechanical properties of the steel storage tank are summarized in Table 11.

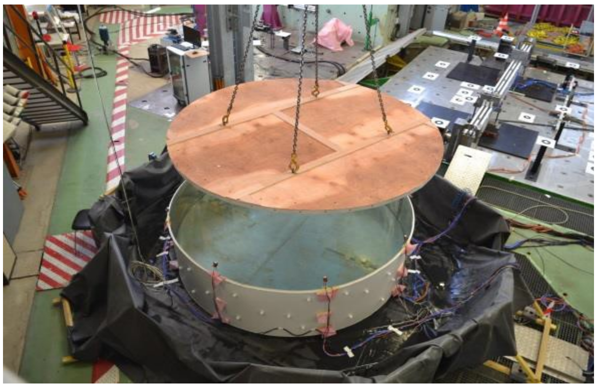

(a)

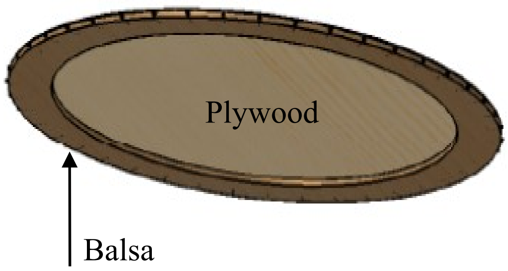

(b)

Figure 23: (a) view of the tested specimen and (b) the floating roof model indicating the inner part made of 5 mm thick plywood and the annular ring to which the 32 mm thick balsa was added.

Table 11: Tank material properties.*

Young's modulus [N/m^2]	$2.1 \cdot 10^{11}$
Poisson's ratio [-]	0.3
Density [kg/m^3]	7850

*Material properties assumed as regular steel without affecting the result.

The process of installing the floating roof of the tested specimen on the shaking table is presented in Figure 23 (a). The floating roof was made of two different types of timber, as schematically presented in Figure 23 (b). The base material was 5 mm-thick plywood, which was used for the entire roof, while the pontoon was simulated with a 26 cm-width annular ring of 32 mm-thick balsa with the mechanical properties presented in Table 12. The outside diameter of the floating roof was slightly less (2.98 m) than the inner diameter of the steel storage tank (3.00 m). In order to reproduce the self-centring behaviour of the floating roof and to simulate the linear elastic contact between the floating roof and the inner side of the tank wall, 43 springs were placed radially in the annular ring as depicted in Figure 24, which presents the section view of the annular ring.

Table 12: The mechanical properties of plywood and balsa.

	Inner plate - plywood	**Annular ring - balsa**
Young's modulus [N/m^2]	$7.8 \cdot 10^9$	$1 \cdot 10^9$
Poisson's ratio [-]	0.26	0.38
Density [kg/m^3]	500	163

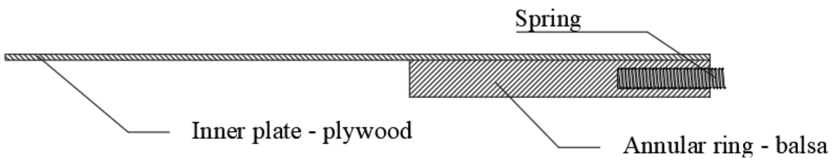

Figure 24: The detail of the installation of the floating roof spring.

In order to prevent damage to the shaking table's electronic instruments due to loss of containment (LOC), a rubber sheet (black) was placed between the bottom plate and the shaking table's surface, as presented in Figure 23 (a). The presence of this insulating rubber sheet affected the friction coefficient (μ_F) between the steel storage tank and the shaking table. Its value was empirically estimated to be 0.11, as reported in (CEA, 2017).

Many sensors were installed on the steel storage tank or the shaking table. Triaxial accelerometers were distributed across the outer surface of the tank to measure the acceleration distribution, taking into account the height of the tank and the angle around the tank axis (see Figure 25 (b)). Also, several pressure sensors were installed on the inner surface of the tank to acquire the pressure response history across the tank's entire height and circumference. Furthermore, vertical displacement sensors were installed on the tank base to monitor the presence of uplift. However, the floating roof was not equipped with measuring devices because its local response was not of particular interest. Only wave gauges were installed on the inner side of the tank wall. The eight wave gauges were radially spaced (as represented by red points in Figure 25 (a)). The wave gauges measured the wave height during the test. The triaxial accelerometer placed on the shaking table also provided useful information. In particular, the accelerometer measured the single horizontal component of the acceleration history (defined by the 0°–180° axis as presented in Figure 25), which was used as a point of comparison with the numerical simulations.

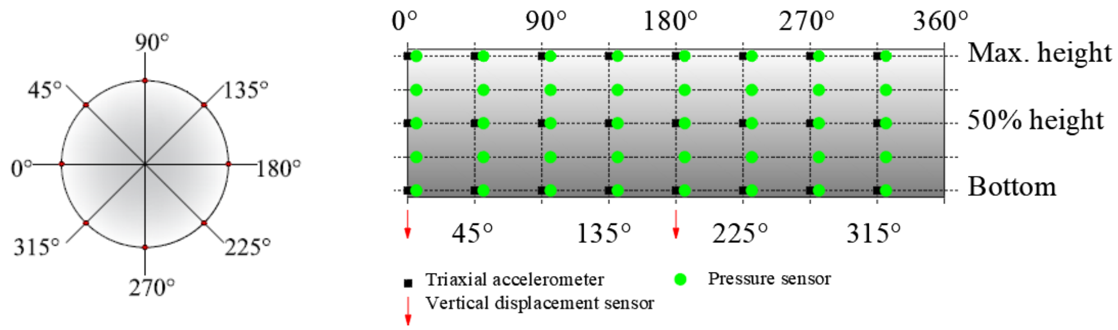

(a) (b)

Figure 25: Location of wave gauges (a) and triaxial accelerometer and vertical displacement sensors (b) in the tested steel storage tank.

4.1.1 Experimental results

Several ground motions with different scaling factors were used during the experimental campaign. However, only the ground motion named "Düzce 29" was used because its frequency content strongly affected the sloshing motion of the floating roof. During the test, LOC occurred mainly due to overtopping. The uniaxial acceleration history recorder on the shaking table along the 0–180° direction (see Figure 25 (a)) and the corresponding response spectrum are shown respectively in Figure 26 (a) and Figure 26 (b).

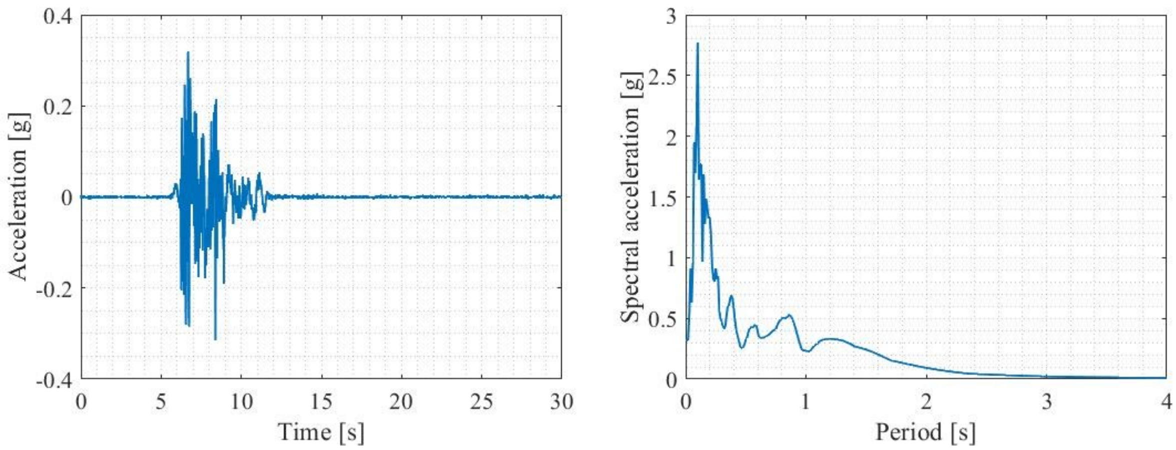

(a) (b)

Figure 26: (a) the shake table acceleration history and (b) the corresponding acceleration response spectrum.

Figure 27 shows an example of data recorded by the wave gauges installed on the inner wall of the steel storage tank (i.e. the wave gauges at the positions 0° and 180°). The maximum wave height was about 10 cm. Note that the upward wave movement corresponds to positive displacements, as shown in Figure 27.

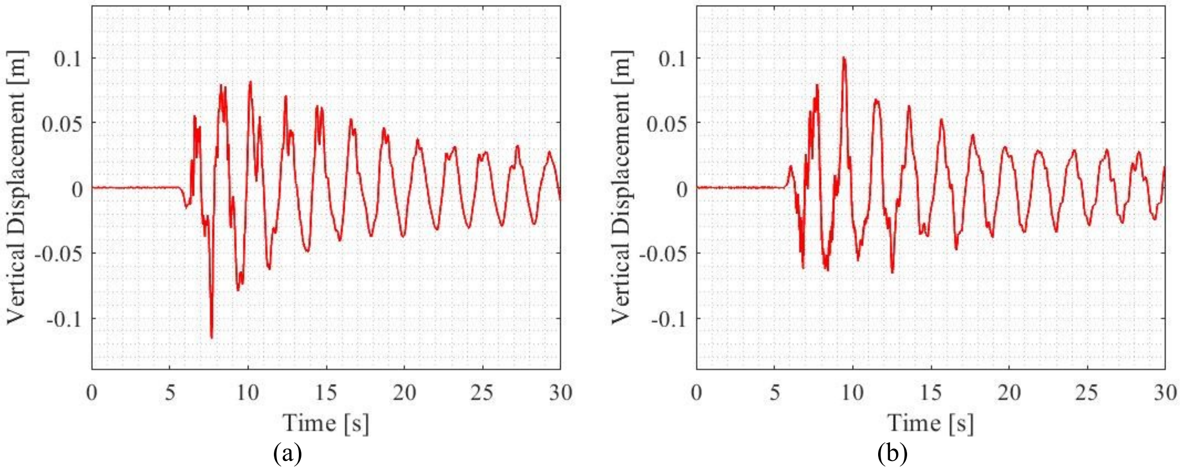

Figure 27: The measured wave height history from the shake table test at (a) the position 0° and (b) 180° (see Figure 25).

During the shaking table test, overtopping was observed (CEA, 2017), highlighted in yellow in Figure 28. According to the data acquired and presented in Figure 27 (b), overtopping, represented by the total exceedance of the freeboard by the floating roof, appears to be only about 1.5 cm. However, as earlier discussed, the roof itself had a thickness of approximately 4 cm, with 3.2 cm of balsa plus 0.5 cm of plywood as shown in Figure 24, and experimental evidences proved it totally exceeded the tank's top edge. Moreover, because of copious LOC occurred, higher wave heights were expectable. This misleading result reflects the difficulties encountered in performing the experimental test and the limitations of the sensors used, which were not capable of recording wave heights properly. Moreover, as presented in the previous section, 43 springs were installed within the annular ring. During the vertical floating roof displacement, once the roof exceeded the top edge of the steel storage tank, the springs popped out of place and obstructed the free movement of the floating roof, affecting the results.

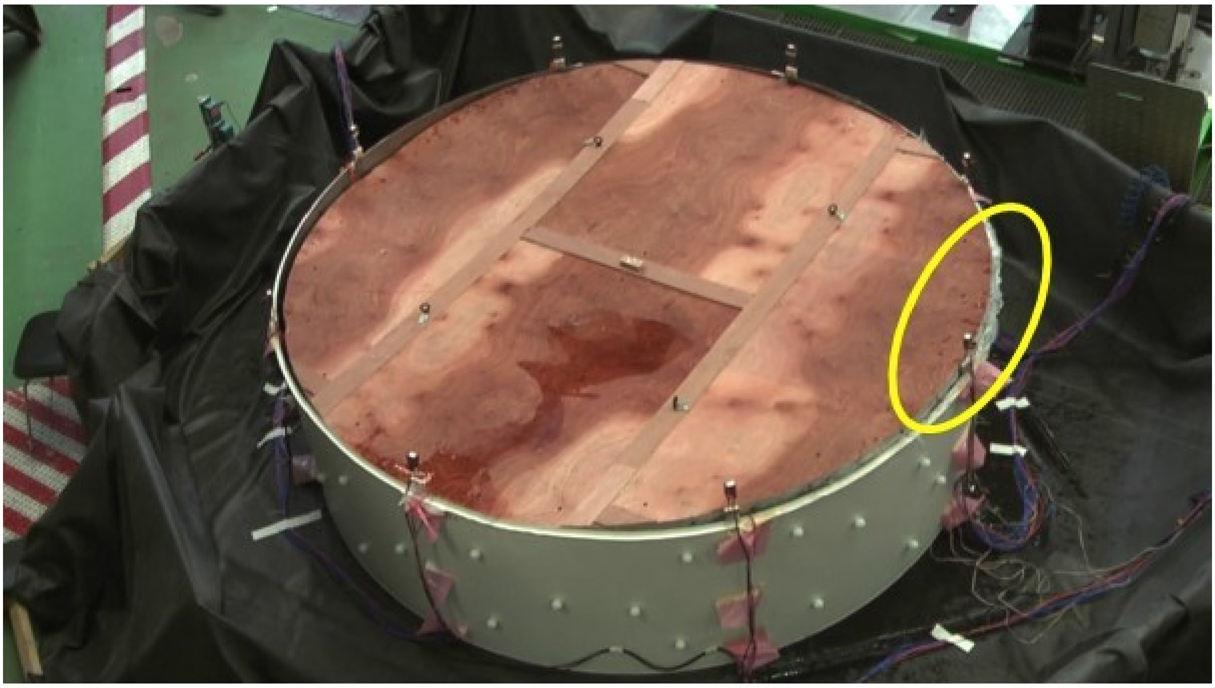

Figure 28: Overtopping during the shake table test.

4.2 Refined FE model of the liquid storage tank with a floating roof

The seismic response of the floating roof was also investigated with a refined FE model (Figure 29), which was developed in Abaqus/Explicit (Dassault Systemes, 2019) software. The model was developed in four parts, which were assembled in the assembly module of the software. Firstly, an analytical rigid surface was modelled to simulate the shaking table (Figure 29). Although Abaqus supports several types of rigid surfaces (i.e. three-dimensional or two-dimensional, discrete or analytical), it was decided to use a two-dimensional analytical rigid surface because the contact with the tank is in one plane and because discrete rigid surfaces are more computationally demanding, as reported in (Dassault Systemes, 2019). Moreover, the analytical rigid surface does not contribute to the rigid body's mass or inertia properties. All the nodes of the analytical rigid surface were constrained to the motion of the surface's reference node (RN) (see Figure 29). Thus, the acceleration history measured on the shaking table during the test was directly imposed to the analytical rigid surface throughout the RN. Note that the ground motion (Figure 26 (a)) was imposed only in the X direction (Figure 29) because the main objective of this case study was to simulate the shaking table test.

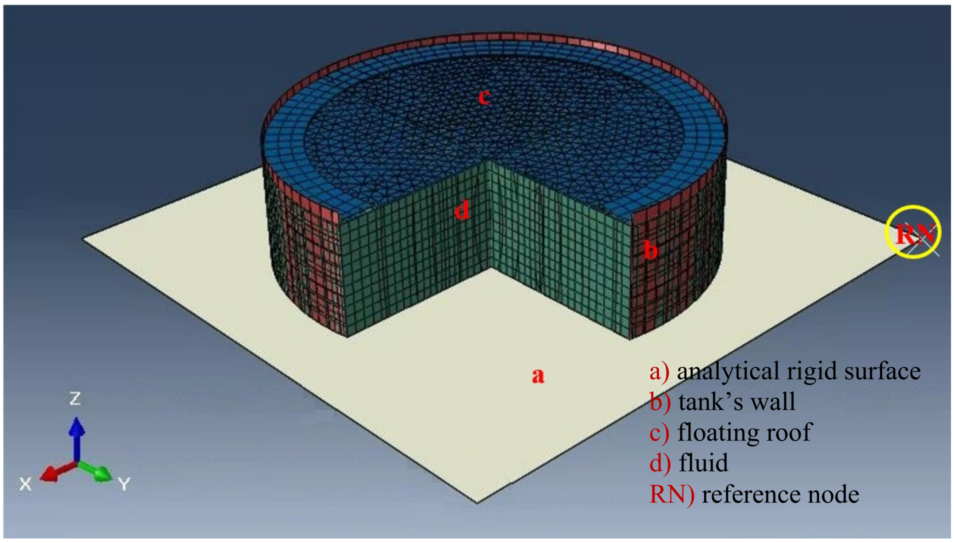

Figure 29: Refined finite element model.

The tank's wall and the bottom plate between the water and the rigid surface (Figure 29) comprised the second part of the refined model and were modelled by fully-integrated S4 shell elements available in the Abaqus/Explicit library. This finite element is defined in the Abaqus' manual under "general-purpose shell elements" and was selected because it does not suffer the transverse shear locking problem. Additionally, this element has no unconstrained hourglass modes. Hence, no hourglass control is required in the bending and membrane response of the fully-integrated S4 element. Moreover, the S4 shell element is capable of providing robust and accurate solutions in all loading conditions for thin and thick shell problems. To reduce the computational time, the material of the steel storage tank was considered linear. Moreover, this assumption is supported by the fact that during the shaking table test no visible damage to the tank was observed. The properties of the steel are listed in Table 11.

The third part of the refined FE model is the floating roof (Figure 29). It was modelled using the same shell elements used for the tank, but it was composed of two parts: the inner plate and the annular surrounding ring. Each part was modelled separately and then coupled. In both cases, the plywood and the balsa were modelled by linear elastic material, the properties of which are presented in Table 12.

The fluid, which represents the fourth part of the model (Figure 29), was modelled with the adaptive meshing technique. The adaptive meshing technique in Abaqus combines the features of pure Lagrangian and pure Eulerian formulations of the problem. This type of adaptive meshing is often referred to as Arbitrary Lagrangian-Eulerian (ALE) analysis. Since the sloshing mode caused a large amount of distortion in the solid element representing the fluid, we employed the automatical mesh refinement process supported by Abaqus (Dassault Systemes, 2019) to ensure that the element itself had a smooth mesh. This process can be accessed in the ALE adaptive mesh domain menu by selecting the desired frequency and re-meshing sweep per increment. The frequency parameter mostly affects the mesh quality, while the re-meshing sweep per increment parameter defines when a new mesh is created by iteratively sweeping over the adaptive mesh domain, as discussed in the Abaqus users' manual (Dassault Systemes, 2019). Default values of the parameters are 10 and 1, respectively. The user can decide whether to improve the accuracy of the adaptive mesh by reducing the frequency and increasing the number of mesh sweeps performed in each adaptive mesh increment. However, this will affect the computational cost. In the present case study, the default parameters were used.

The water was modelled by a three-dimensional solid element, C3D8R, which is a general-purpose brick element defined by eight nodes. In order to model the fluid static and dynamic behaviour, a hydrodynamic material model was needed. Thus, the material's volumetric strength was determined by an equation of state (EOS) provided for the content material (i.e. the water), which is supported by Abaqus/Explicit. However, the EOS can be defined in different ways. In the present model, a linear EOS was adopted. This EOS can be defined in the software by selecting the "Us-Up" type of EOS, which is the linear form of the Mie-Grüneisen EOS. This type of EOS proved to be particularly useful because it treats pressure as a function of the density and the internal energy per unit mass of the fluid. Internal energy is defined by the rate at which heat is added and the work done by stresses. However, if heat and stresses are neglected, the linear "Us-Up" can be defined (Constantinescu et al., 2011). The definition of the "Us-Up" EOS for the fluid modelled in this case study required the selection of three parameters: the reference speed of sound in the medium (C_0), the slope of the Us-Up curve (s) and the Grüneisen ratio (Γ_0) of the material. This EOS can also be applied to materials that have isotropic elastic or viscous deviatoric behaviour (Dorogoy et al., 2011). Furthermore, dynamic viscosity (μ_V) was provided to simulate the behaviour of water. Table 13 presents the properties of the water model. It is worth noting that material properties are temperature-dependent, and so the ambient temperature (20 °C) was assumed. Note also that the water density (ρ) and μ_V were selected according to Crittenden et al. (Crittenden et al., 2012), while C_0 was selected according to Cutnell et al. (Cutnell & Johnson, 2009). Finally, s and Γ_0 were set to zero, as reported in the Abaqus examples manual.

Table 13: Properties of the FE model of water.

ρ [kg/m^3]	998.2
μ_V [N/m s]	$1.002 \cdot 10^{-3}$
C_0 [m/s]	1482
s [-]	0
Γ_0 [-]	0

Once all the parts of the model were created and assembled, it was necessary to carefully model the contacts between different parts of the model. Two categories of contacts were used in this model: the friction between the tank bottom plate and the shaking table and the frictionless contact between the tank contents and the tank and floating roof. Abaqus/Explicit offers various ways to model contacts. For friction and frictionless cases, the normal behaviour of the contact plane of two materials was modelled by “hard contact,” which does not allow penetration of elements but does allow separation between the two materials. This feature can account for tank uplift. Concerning the tangential behaviour of the contact between the tank bottom plate and the shaking table, a friction coefficient of 0.11 was used, as earlier mentioned. Zero friction was considered in the case of contacts between the water, the steel plates of the tank and the floating roof.

4.3 Simulation of the shake table test

The seismic response of the floating roof was first simulated using the simplified model which input data were partially presented in the previous sections. The height of the water H and the tank’s diameter R are defined in the description of the tested tank, while ρ is presented in Table 13. The gravity acceleration g was assumed to equal 9.81 m/s^2. The number of floating roof modes I can affect the computational cost because the matrices size is $I \times I$, but as discussed by Hosseini et al. (Hosseini et al., 2011), the effects of higher modes are relatively unimportant for the estimation of the vertical displacement of the floating roof at the edge of the tank. Thus I was assumed to equal three. The critical damping ratio ζ has to be carefully selected because it strongly affects the amplitude of the vertical displacement of the floating roof. In general, there are phenomena involved in the dynamic behaviour of a floating roof (i.e. friction between the annular sealing and the internal tank wall, floating roof impacts, etc. (Nishi et al., 2008)) which can be at least approximately simulated by viscous damping. However, the quantification of the critical damping ratio is not straightforward. In the work of Nishi et al. (Nishi et al., 2008), an experimental study on sloshing behaviour in a real tank showed how the damping ratio may vary with wave height. However, the authors considered ζ = 2.5% to be an appropriate value to represent the maximum wave height. Thus, the same damping ratio was used for the present case study’s simplified model by adopting the classical Rayleigh damping model. Since the presence of the floating roof may significantly affect the first natural sloshing mode, while its stiffness has important effects only on higher modes (Hosseini et al., 2011), the first and third vibration modes of the floating roof have been considered to calibrate the Rayleigh coefficients.

In the simplified model, it was necessary to pay particular attention to the selection of the material properties of the floating roof. Indeed, the floating roof of the case study is composed of two different materials with different densities and thicknesses, while the formulation of the model presented accepts only one value for each of these parameters. Thus, in the first attempt at model calibration, only the inner plate was considered, with its corresponding mechanical (Table 12) and geometrical properties.

The vertical displacements of the floating roof at 0° and 180° are shown in Figure 30 (a) and Figure 30 (b), respectively, along with the experimental measurements of the wave gauges. In addition to the basic simplified model, which accounts for the floating plywood roof only, an additional model was developed. In this case, the characteristics of the floating roof approximated the effect of the plywood and balsa installed at the annular ring. Equivalent values for Young's modulus E and Poisson's ratio ν were calculated as the volume-weighted mean of Young's moduli and Poisson's ratios of plywood and balsa, as suggested in (Tornabene, 2012). This produced E and ν values of $2.7 \cdot 10^9$ (N/m^2) and 0.35, respectively. Additionally, the equivalent thickness of the floating roof h_e was also defined. First, the floating roof flexural stiffness (R_f) was evaluated according to (Huston & Josephs, 2008):

$$R_f = \frac{E {h_{ip}}^3}{12(1-\nu^2)} + \frac{EI}{d} \tag{43}$$

where h_{ip} is the inner plate thickness, I is the second moment of inertia of the annular ring section with respect to the middle axis of the inner plate, and d is the floating roof diameter minus the annular ring width. Eq. (43) yielded to bending stiffness of approximately 2240 N/m. Equating Eq. (43) with the stiffness of an ideal homogeneous plate, the equivalent uniform thickness h_e was determined to be approximately 2 cm. This value was used for the recalculation of the equivalent density of the floating roof ρ_r under the hypothesis of the invariance of the total mass.

The modified simplified model, which accounts for the effects of the plywood and the balsa, was subjected to ground motion recorded during the shaking table test campaign (Figure 26 (a)). Results are presented in Figure 31 (a) and Figure 31 (b), which are also compared with the experimental data for 0° and 180° respectively.

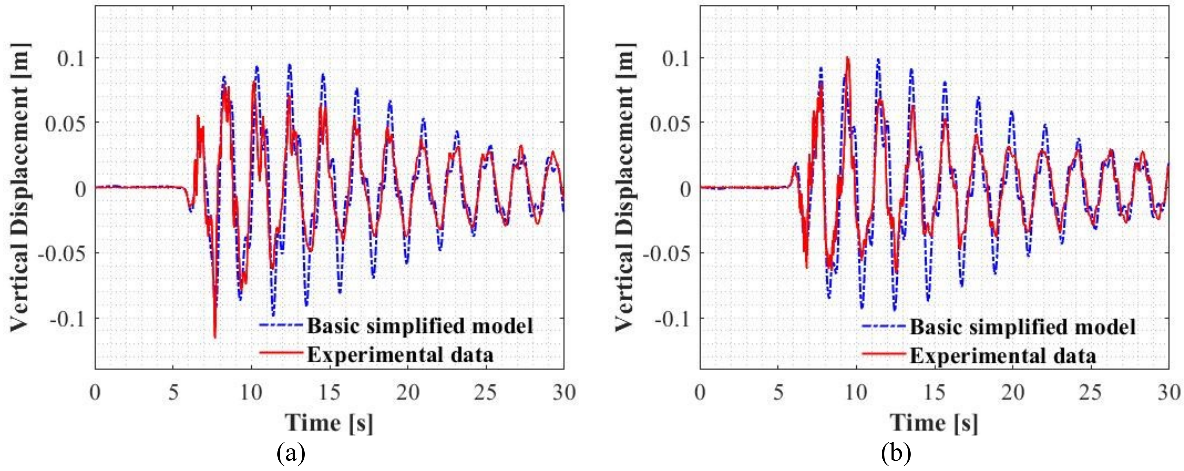

Figure 30: Vertical displacement histories of the floating roof obtained by the basic simplified model at locations (a) 0° and (b) 180° (see Figure 25 (a)) and the corresponding experimental data from the shaking table test).

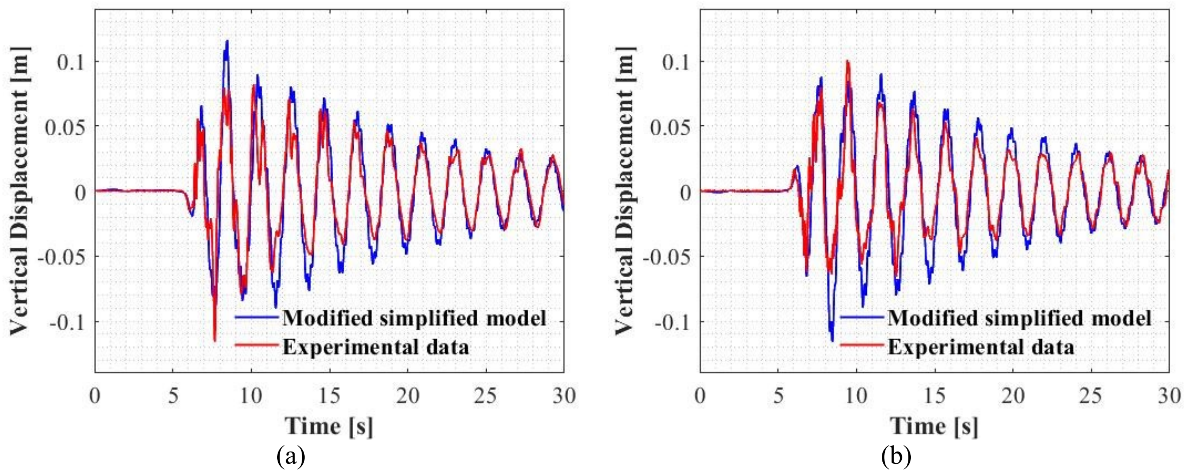

Figure 31: Vertical displacement histories of the floating roof obtained by the modified simplified model at locations (a) 0° and (b) 180° (see Figure 25 (a)) and the corresponding experimental data from the shaking table test. The floating roof of the modified simplified model accounts for the effects of plywood and balsa.

The basic simplified model, which does not account for the influence of the annular ring, provided an excellent match with the experimental data in terms of phase for both the directions examined (Figure 30 (a) and Figure 30 (b)). This confirms that, for the present case study, the vertical fluid displacement is mainly driven by the first convective mode, which is largely affected by the ratio of the fluid height to the tank's radius. At the same time, an overestimation of vertical displacement due to an underdamped behaviour is appreciable mainly in the free vibration range (over 12 seconds). The reason for this behaviour is related to the damping approach adopted in the governing equation of motion (Eq. (23)). Indeed, in Eq. (23) a Rayleigh approach was introduced and a damping matrix (Eq. (22)), which is sensitive to the mass and stiffness of the floating roof, was defined. The failure to consider the presence of the annular ring led to the underestimation of the coefficients of the damping matrix. When the effect of the annular ring was included (Figure 31 (a) and Figure 31 (b)), the simulation of the response history of vertical displacement was significantly improved, although the modified simplified model seemed to overestimate the maximum vertical displacement in comparison with the experimental results (see Figure 31 (a)). However, as previously presented, conspicuous overtopping occurred during the shaking table test (Figure 28) even though sensors were not able to properly capture it. This outcome seems to agree with the experimental test as can be observed in Figure 28, where the photo presents the peak vertical displacement from the experiment, which is greater than that measured by the sensors.

Subsequently, the seismic response of the floating roof was simulated by the refined FE model developed in Abaqus (Dassault Systemes, 2019). To be consistent with the assumptions of the previously analysed model, the Rayleigh coefficients were assumed to be equal to those used in the simplified model. The results provided by the FE model were validated by the results of the shaking table test. The lateral displacement history in the X direction (i.e. the reference axis) is presented in Figure 32 (a) for the RN node of the analytical rigid surface and the central inner node of the tank bottom plate. It can be concluded that sliding did not occur between the steel storage tank model and the analytical rigid surface. The same was observed during the shaking table test, as recorded in the testing report (CEA, 2017). The vertical displacement history of the steel storage tank bottom plate calculated at its edge at locations 0° and 180° (see Figure 25) is presented in Figure 32 (b). This result indicates that tank uplift was negligible which is consistent with the observations from the test (CEA, 2017).

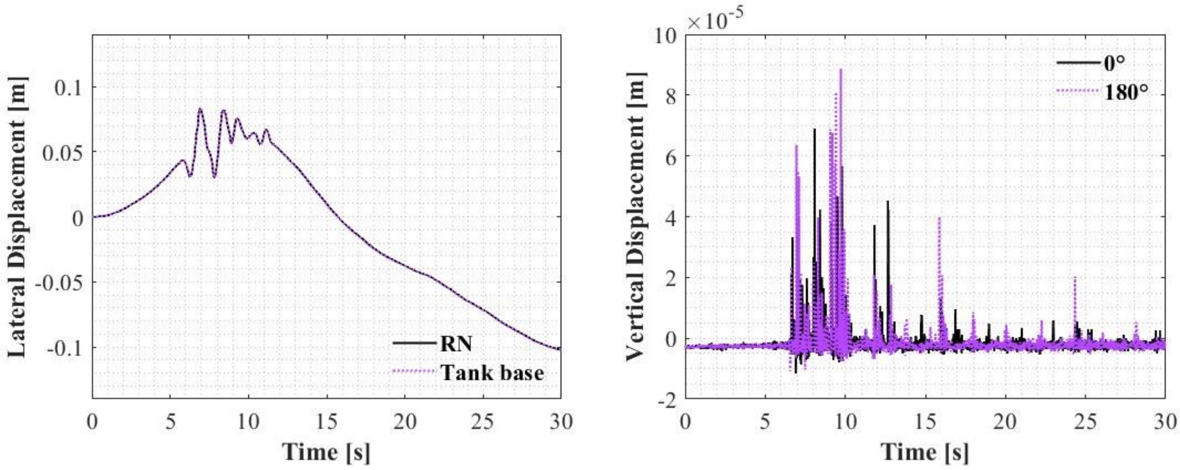

(a) (b)

Figure 32: (a) lateral displacement history in the X direction (i.e. the reference axis) for the RN node of the analytical rigid surface and the central inner node of the tank bottom plate, and (b) the vertical displacement history of the steel storage tank bottom plate calculated at its edge at locations 0° and 180°.

Figure 33 (a) and Figure 33 (b) show the calculated vertical displacement history of the floating roof at 0° and 180°, respectively, and compare this history to experimental data. The refined FE model allows the monitoring of both the floating roof and the liquid surface. The calculated vertical displacement of the floating roof and the wave height are shown in Figure 33 and compared to the wave height measured during the shaking table test. Results displayed a close match with the experimental data obtained by the shaking table test. Indeed, as depicted in Figure 33, good in-phase behaviour is appreciable for both 0° and 180°. The maximum vertical displacement seems to be overestimated, especially at 0° (Figure 33 (a)), but such an outcome was expected, as discussed above. In the free vibration range of response (i.e. for timing over approximately 12 seconds), the response was overestimated, although the difference was on the order of a few centimetres. Only slight delamination between the floating roof and the liquid (the contents of the tank) was observed in the peaks of vertical displacement in the range of forced vibration (i.e. for timing less than approximately 12 s).

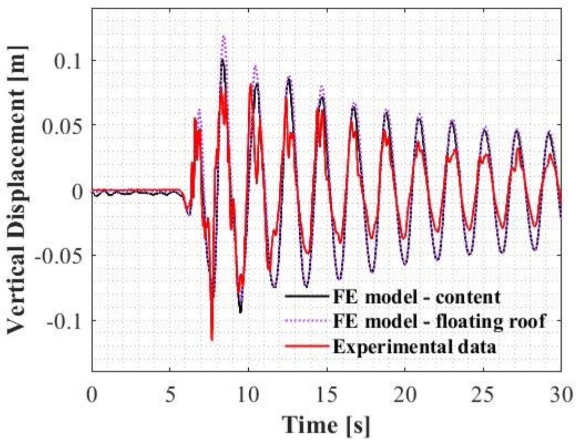

(a)

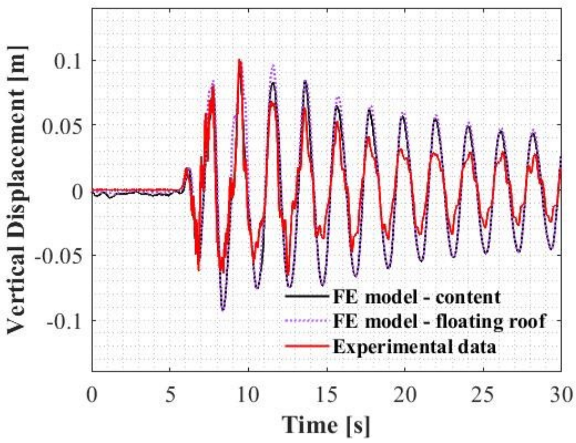

(b)

Figure 33: Vertical displacement histories of the floating roof and the water wave calculated by the refined FE model and the vertical displacement of the content recorded during shaking table testing presented for the locations (a) 0° and (b) 180°.

Moreover, the results of the refined FE model can also be used to check the impact of some assumptions used in the simplified model. For example, the assumption of perfect contact between the floating roof and the fluid, which was used in the simplified model, may not significantly affect the results obtained by the governing equation of motion (Eq. (42)), although a gap of 1 to 2 cm was observed between the water and the floating roof (see Figure 33 (a) and Figure 33 (b)) in the time interval corresponding to forced vibration (6–12 s). However, this vertical displacement gap tended to reduce as soon as the period of forced vibration ended. After this period, the gap of vertical displacement became practically negligible. Moreover, a perfect agreement in terms of the period can be appreciated between refined FE model outcomes and experimental evidence.

Finally, a comparison between the vertical displacement histories provided by both numerical models is provided in Figure 34. The vertical displacement of the liquid surface produced by the refined FE model is also presented in Figure 34.

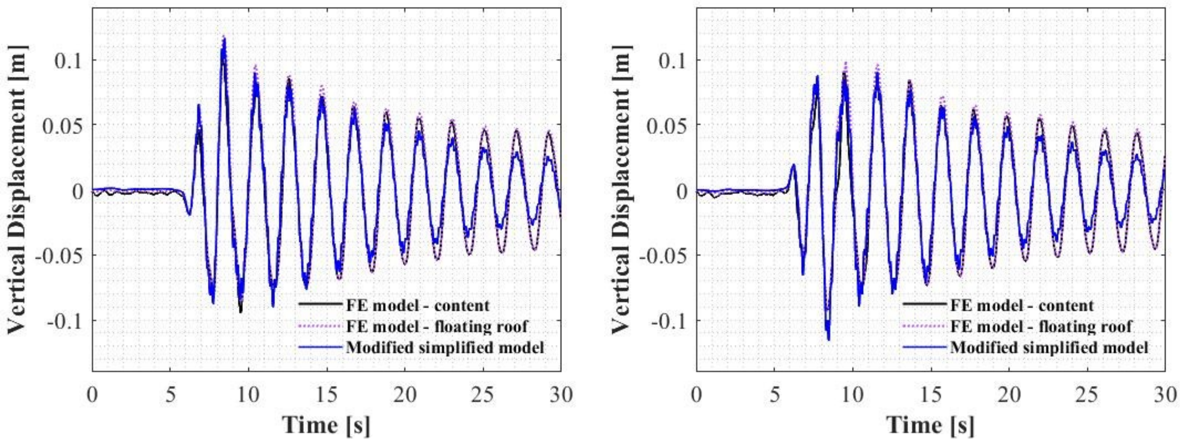

(a) (b)

Figure 34: Vertical displacement histories of the refined FE model and the modified simplified model at locations (a) 0° and (b) 180°.

Both the simplified model and the refined FE model overestimate the maximum vertical displacement in comparison with the experimental results (Figure 31 (a) and Figure 33 (a)). However, as previously mentioned, conspicuous overtopping occurred during the shaking table test (Figure 28). Therefore, the peak vertical displacement values obtained by both numerical models are in agreement with empirical observations (see Figure 28). Moreover, by comparing the experimental data with the models' results, satisfactorily in-phase behaviour can be observed. This reflects accurate mass and stiffness choices in the simplified model's input data and good modelling assumptions in the refined model. In this respect, it is worth emphasising that vertical floating roof displacement is mainly driven by the first sloshing mode, which is largely affected by the aspect ratio (γ=H/R) of the storage tank. Even in the free vibration range, the vertical displacement histories of both modelling approaches agree with each other and closely match the experimental data.

4.3.1 Parametric study

The seismic response of the floating roof was investigated through a parametric study of what input data has the greatest impact on the floating roof's vertical displacement. The modified simplified model, which accounts for the presence of the balsa annular ring, was used as the basic model in the parametric analysis. Each analysis was performed with the same ground motion adopted in the experimental campaign (Figure 26 (a)). The following parameters of the modified simplified model were varied:

- the aspect ratio of the tank (γ = H/R), which represents the ratio between the fluid height and the tank radius;
- the roof density ρ_r;
- Young's modulus of the floating roof E; and
- the content density ρ_l.

One parameter was varied at a time, while the other parameters maintained the same values used in the modified simplified model. The aspect ratio γ was assumed to range between 0.1 and 1 and was used to investigate the influence of the filling level on the response (E=2.7·10^9 N/m^2, ρ_l=998.2 kg/m^3 and ρ_r=208 kg/m^3). Roof density ρ_r was assumed to range from 100 to 1000 kg/m3 as presented in Table 15 (E=2.7·10^9 N/m^2, γ=0.5 and ρ_l=998.2 kg/m^3). Some roof density values may be inapplicable to real tanks but were kept to investigate the influence of this parameter across a wide range of possible density values while keeping the plywood density as the median value of the selected range (see Table 12). Young's modulus is assumed to vary from 1·10^5 N/m^2 to 5·10^9 N/m^2, as presented in Table 15 (ρ_l=998.2 kg/m^3, γ=0.5 and ρ_r=208 kg/m^3). Considering the plate stiffness formula (see Eq. (24)), the variation of E can be interpreted as the variation of the thickness or both parameters. Therefore, only the Young modulus was varied. Content density ρ_l ranges from 150 to 1050 kg/m3 (Table 15) (E=2.7·10^9 N/m^2, γ=0.5 and ρ_r=208 kg/m^3). Even in this case, some values may be unrealistic but were kept in the parametric study to investigate potential nonlinear effects.

In the first input parameter variation, the objective was to calculate the maximum vertical displacement at location 0° (see Figure 25) and then compare the results (w) with the maximum expected wave heights (w_e) calculated according to the simplified procedure proposed in (Malhotra et al., 2000), which does not account for the effects of the floating roof. Results are presented in Table 14 together with the first convective period T_c and the corresponding spectral acceleration $S_e(T_c)$. The results correspond to the edge of the floating roof (i.e. r = R). The calculated vertical displacement history is also presented in Figure 35 (a). It can be observed that the greater the aspect ratio γ, the greater the vertical displacement. The maximum calculated vertical displacement corresponded to γ = 1 and was about 18 cm. This result is in agreement with the expected values obtained by the simplified procedure (Table 14). Moreover, an increase in the response period can easily be observed in the results of the modified simplified model (see Figure 35 (a)). This is most relevant for the free vibration motion, which begins after approximately 12 seconds. The reason for this behaviour is related to the large difference in the vibration mode most relevant to the sloshing. Indeed, by comparing the first convective period from γ = 1 to γ = 0.1, a period increase can be appreciated, which is also evident in Figure 35 (a).

Table 14: Influence of H/R ratio on the maximum vertical displacement of the floating roof and the expected wave height estimated according to (Malhotra et al., 2000).

γ [-]	T_c [s]	$S_e(T_c)$ [g]	w_e [m]	w [m]
0.1	4.23	0.01	0.014	0.011
0.2	3.04	0.02	0.031	0.028
0.3	2.55	0.04	0.054	0.044
0.4	2.28	0.05	0.079	0.080
0.5	2.12	0.07	0.110	0.110
0.6	2.01	0.09	0.134	0.132
0.7	1.95	0.10	0.152	0.147
0.8	1.90	0.11	0.166	0.162
0.9	1.87	0.12	0.176	0.172
1	1.85	0.12	0.183	0.179

Table 15 presents all the remaining parameters varied in the parametric analyses with their relative maximum vertical displacements ($w_{\rho r}$, w_E and $w_{\rho l}$ respectively) as calculated by the simplified model. The results are plotted in Figure 35 (b–d).

Figure 35 (b) shows the influence of ρr on vertical displacement. The weak influence of the variation in ρ_r can be observed. However, as ρr increases, the vertical displacement increases as well, with a difference of 3.5 cm from ρ_r = 100 kg/m^3 to ρ_r = 1000 kg/m^3. More significant is the shortening of the period, which is mainly evident after 12 s and is in the order of 10%. The vertical displacements for several values of E, which are listed in

Table 15, are shown in Figure 35 (c). It can be observed that the response is slightly affected by E. All the time-histories presented are in-phase with each other, which confirms that the dynamic response is mainly driven by the first convective mode of the liquid. Moreover, the influence of E is excluded since it is a "rigid" mode (i.e. the first floating roof mode, see for instance Eq. (A.2)) that governs the response of the fluid. The impact of ρ on vertical displacement is presented in Figure 35 (d) (see also

Table 15). As the ρ increases the maximum vertical displacement decreases with an overall difference of approximately 4 cm. A small phase shift can also be observed with an increase of the period of approximately 5% from ρ =150 kg/m^3 to ρ = 1050 kg/m^3.

Table 15: Parametric analysis input parameters and maximum vertical displacement observed.

#	ρ_r [kg/m^3]	$w_{\rho r}$ [m]	E [N/m^2]	w_E [m]	ρ [kg/m^3]	$w_{\rho l}$ [m]
1	100	0.135	$1\cdot10^5$	0.083	150	0.147
2	200	0.132	$5\cdot10^5$	0.089	250	0.130
3	300	0.137	$1\cdot10^6$	0.094	350	0.127
4	400	0.140	$5\cdot10^6$	0.111	450	0.122
5	500	0.139	$1\cdot10^7$	0.126	550	0.123
6	600	0.143	$5\cdot10^7$	0.120	650	0.123
7	700	0.149	$1\cdot10^8$	0.100	750	0.121
8	800	0.158	$5\cdot10^8$	0.113	850	0.116
9	900	0.164	$1\cdot10^9$	0.116	950	0.121
10	1000	0.170	$5\cdot10^9$	0.113	1050	0.111

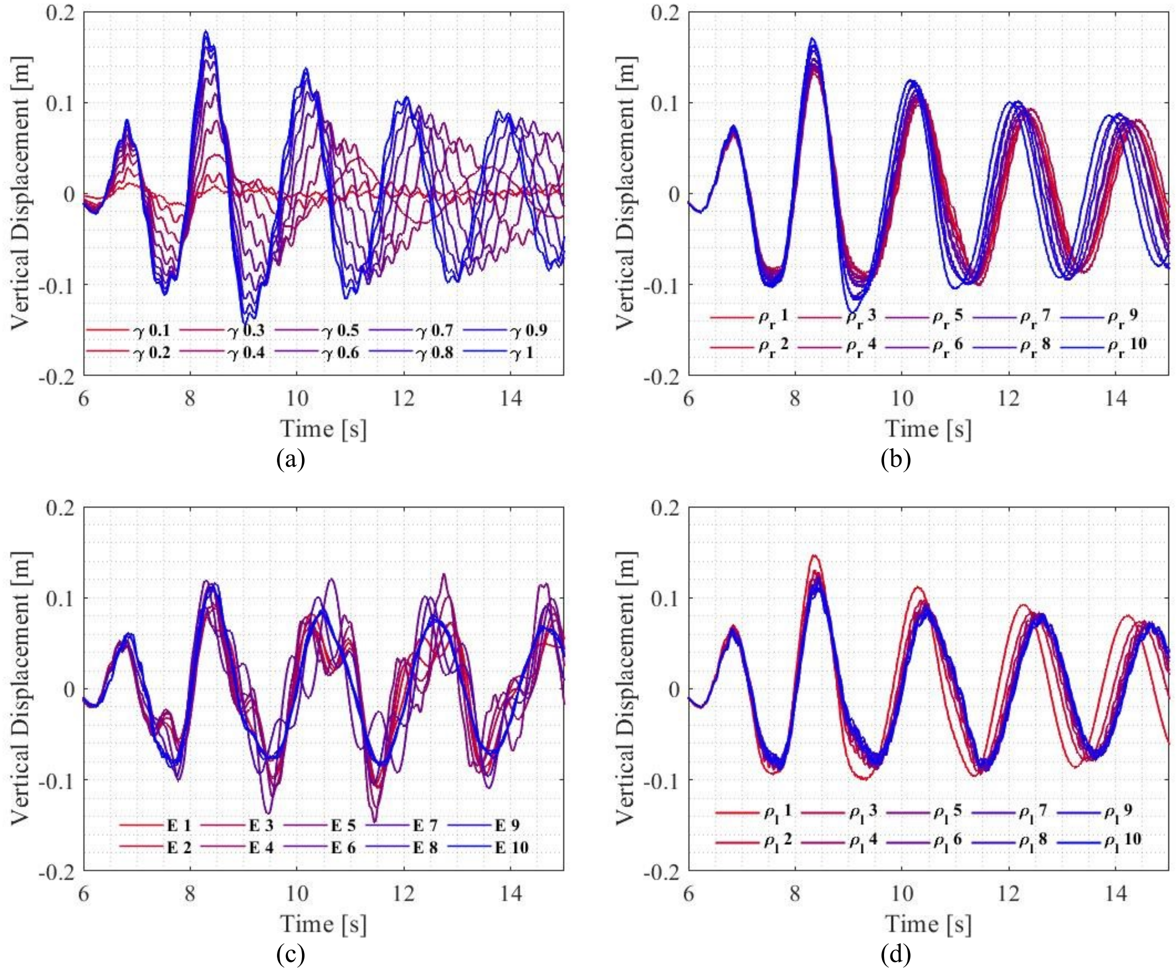

Figure 35: Vertical displacement histories computed by the simplified model for (a) different γ (H/R ratios), (b) different ρ_r, (c) different E and (d) different ρ_l.

4.4 Discussion

A refined FE three-dimensional model was developed for a scaled steel storage tank with a floating roof and set in the Abaqus software. Whilst the refined FE model achieved accurate results, it entailed a significant modelling effort and proved to be extremely time-consuming from a computational viewpoint. Conversely, the simplified model required particular attention in input data definition, especially due to the presence of the annular ring, which can affect the vertical dynamics of the floating roof. Nonetheless, both the refined FE model and the simplified model provided quite similar response histories for vertical displacements of the roof at the edge of the tank wall. In the refined FE model, only slight delamination between the floating roof bottom surface and the fluid surface was observed. For the investigated tank, this validated the assumption of perfect contact between the bottom surface of the floating roof and the fluid surface, which was adopted in the case of the simplified model.

To assist in the models' calibration and validation, shaking table test results on a scaled steel storage tank equipped with a floating roof were taken into account. The experimental test provided very useful and rare experimental data concerning the dynamic response of the floating roof under seismic loading. From the shaking table test, it was obvious that relatively weak ground motion caused spillage of liquid out of the tank. This phenomenon was adequately simulated by the FE model as well as by the simplified model, which makes the simplified model attractive for seismic risk studies that account for record-to-record randomness.

Although results from both models agree with the experimental data observed for the particular tank investigated in this case study, more studies are needed to further validate the models presented here and to better understand the limitations and seismic performance of the floating roofs of liquid storage tanks.

A simple parametric study highlighted the strong influence of the γ ratio on peak vertical floating roof displacement compared to the other parameters investigated. Variation of the floating roof's Young's modulus negligibly affected maximum vertical displacement and was relevant mostly to the free vibration range with larger response variation. Finally, it was found that the closed-form solution for peak vertical displacement can be sufficiently accurate, but this conclusion should be confirmed with response history analyses of floating roofs for a large variety of ground motions and a variety of storage tanks equipped with floating roofs.

5 SEISMIC FRAGILITY ANALYSIS OF STEEL STORAGE TANK WITH FLOATING ROOF

The mitigation of structural damages may be adopted (Krausmann et al., 2017) in order to prevent a large amount of LOC. However, the prevention of liquid sloshing, which can produces a larger amount of LOC, is usually not taken into account (Krausmann et al., 2017). This may endanger the safety in a wider area of the petrochemical plant. In this respect, LOC from the excessive vertical displacement of a floating roof represents a key aspect in the risk assessment of petrochemical plants. However, in order to provide an insight into the most relevant LOC source in the selected steel storage tank, two LOC sources were analysed: fluid overtopping due to excessive floating roof vertical displacement and tank wall failure due to the so-called elephant's foot buckling.

The LOC due to elephant's foot buckling was investigated by several authors who provided relevant contributions (Razzaghi & Eshghi, 2004; Virella et al., 2006; Buratti & Tavano, 2013; Phan & Paolacci, 2016; Alessandri et al., 2018; Bernier & Padgett, 2019). The same cannot be said for the LOC due to excessive floating roof displacement, especially if the problem is addressed by performing seismic fragility analysis. In this respect, the seismic fragility analysis reated to LOC due to the vertical displacements of the floating roof itself is performed.

In the fragility analysis a real storage tank is considered. It is made by steel shell courses with a diameter and height of 43 m and 22 m respectively. The filling level of the liquid storage tank varies within its lifetime however, in the following, only 90%, 80% and 70% of filling levels were taken into account. The reason for this choice relies on several aspects. First, it is worth mentioning that lowering the filling level corresponds to a linear increase of the available height for attaining overtopping, which means that the risk for overtopping is automatically reduced because of that. Furthermore, the lower the filling level (lower γ), the higher T_c (e.g. at 20% of filling level, for the selected case study, T_c is 23 s), which can be concluded based on Eq. (49), becoming the record selection much more challenging. Finally, given the main purpose of steel storage tanks, low filling levels were assumed to be less probable than higher ones, which results in a negligible influence on risk, as discussed later in Chapter 6.

5.1 Description of the liquid storage tank with floating roof

The seismic fragility analysis is performed for an unanchored steel storage tank equipped with a single deck floating roof. It is assumed to be located in Priolo Gargallo, Sicily, Italy (see Figure 36, PGA 0.25 *g* for 475 years of returning period). The soil type, according to the classification by EC 8-1 (CEN, 2004) is B, as reported in Paolacci et al. (Paolacci et al., 2018a). The storage tank comprises ten courses, the thickness of which varies along with the height, but with course number ten being made of angular profiles. The overall height (H_t) is 22 m, whereas the tank diameter is approximately 86 m. The bottom plate has a thickness of 16 mm. Different types of steel were used for the construction of the storage tank. In Table 16, the geometrical properties and adopted material for all the components used in the construction of the steel storage tank are listed.

Figure 36: Satellite view of Priolo Gargallo's location (Google Earth, 2020).

Table 16: Geometrical properties and material for the steel storage tank.

Component	Height [mm]	Thickness [mm]	Steel*
Bottom plate	[-]	16	Fe 52 D
Course 1	2434	43	Fe 52 D
Course 2	2434	40	Fe 52 D
Course 3	2433	33	Fe 52 D
Course 4	2433	28	Fe 52 D
Course 5	2433	23.4	Fe 52 D
Course 6	2433	18.6	Fe 52 D
Course 7	2433	14	Fe 52 D
Course 8	2433	12	Fe 52 D
Course 9	2433	12	Fe 42 B
Course 10	100 (L shape)	10	ASTM A7

*Steel as-built denomination.

The filling level is assumed to vary (from 90%, 19.8 m, to 70%, 15.4 m), whereas the remaining part of the total height is assumed to be freeboard. In Figure 37 (Google Earth, 2020), an example of a steel storage tank equipped with a single deck floating roof similar to the one object of this study is provided. First, it is worth noting that a large number of fittings are installed either on the deck or the surrounding annual ring (the pontoon) of the floating roof (e.g. the rolling ladder, draining systems). However, in the present study, they have been neglected.

Figure 37: Example of the steel storage tank equipped with a single deck floating roof.

The floating roof is composed of two parts: an inner plate and the pontoon, both made of steel (Figure 38 (a)). The pontoon presents a trapezoidal cross-section, Figure 38 (b), and several bulkheads are equally spaced along the circumferential direction in order to divide the entire pontoon into sealed sections (Figure 38 (a)). Each section is stiffened by means of steel profiles welded between the higher and lower pontoon surface (Figure 38 (a)). The inner plate has a diameter of approximately 70 m, whereas the outside floating roof diameter is several centimetres lower than the one of the steel storage tank. The inner plate thickness is 5 mm. The gap between the steel storage tank inner wall and floating roof (Figure 38 (a)) is filled by a deputed gasket, ensuring the sealing of the facility. The pontoon's cross-section dimensions, in meters, are presented in Figure 38 (b). The left-hand side of Figure 38 (b) is where the conjunction with the inner plate is realized by welding the inner plate edge to the vertical inner pontoon's rim, the thickness of which is 35 mm, whereas the outer rim's thickness is 6.35 mm. The upper and lower plates' thicknesses are both 5 mm.

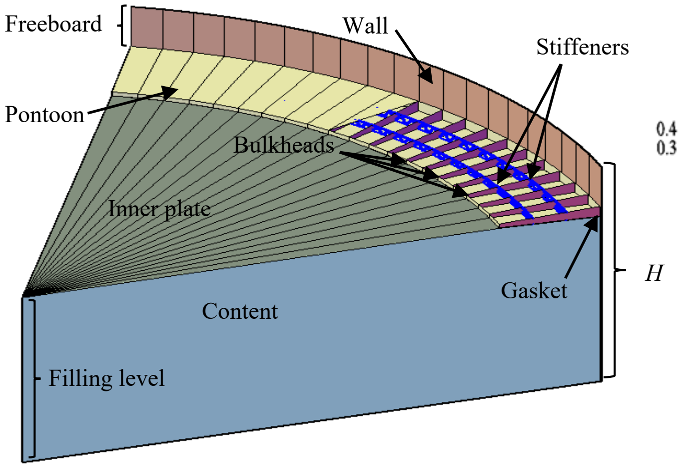

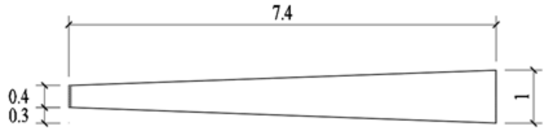

(a) (b)

Figure 38: (a) tank and (b) dimension of pontoon's cross-section in meters.

5.2 Description of the refined FE model and validation of the simplified model for the floating roof

In section 5.2.1, the refined FE model is introduced and the EC 8-4 (CEN, 2006) formula (A.15) is used to verify its performance in terms of the convective response of fluid (section 5.2.2). Because the EC 8-4 (CEN, 2006) formula (A.15) does not account for the floating roof effect, the floating roof was disregarded in the refined FE model, but only for the purpose of its verification which involved the excitation of the tank and the fluid by means of a monochromatic wave only. The resulting maximum vertical displacement of the fluid was then compared to the expected value calculated with the Eurocode formula, as presented in section 5.2.2. In section 5.2.3, the floating roof presence was taken into account in the refined FE model to validate the vertical roof displacements obtained by the simplified model.

5.2.1 Description of the refined FE model

The refined FE model utilizes Abaqus/Explicit (Dassault Systemes, 2019) software, which is more effective when large displacement in the model occurs compared to Abaqus/Standard. The refined FE model developed in Abaqus consists of different parts subsequently assembled in the Assembly module of the software. In Figure 39, the analytical rigid surface is presented. It was used to model the contact between the bottom plate of the steel storage tank and the ground.

The steel storage tank wall and bottom plate, (Figure 39), were modelled by means of shell elements. Each course of the steel storage tank wall (see Table 16) was modelled separately and, subsequently, merged. This approach was decided upon to provide the appropriate thickness for each part. Steel was modelled using a perfectly elastic behaviour. In Table 17, the steel properties provided to the model for the steel storage tank and floating roof are listed. Fully integrated S4 shell elements, available in the Abaqus/Explicit library, were also used to model the steel storage tank and floating roof. This kind of element is defined in the Abaqus' manual as ‘general-purpose shell elements’. These elements were selected because they do not suffer from transverse shear locking and do not have any unconstrained hourglass modes; hence, no hourglass control is required in the bending and membrane response of the fully integrated element S4. Moreover, they are capable of providing robust and accurate solutions in all loading conditions for thin and thick shell problems.

Table 17: Steel storage tank and floating roof material properties.

Young's modulus [N/m^2]	$2.1 \cdot 10^{11}$
Poisson’s ratio [-]	0.3
Density [kg/m^3]	7850

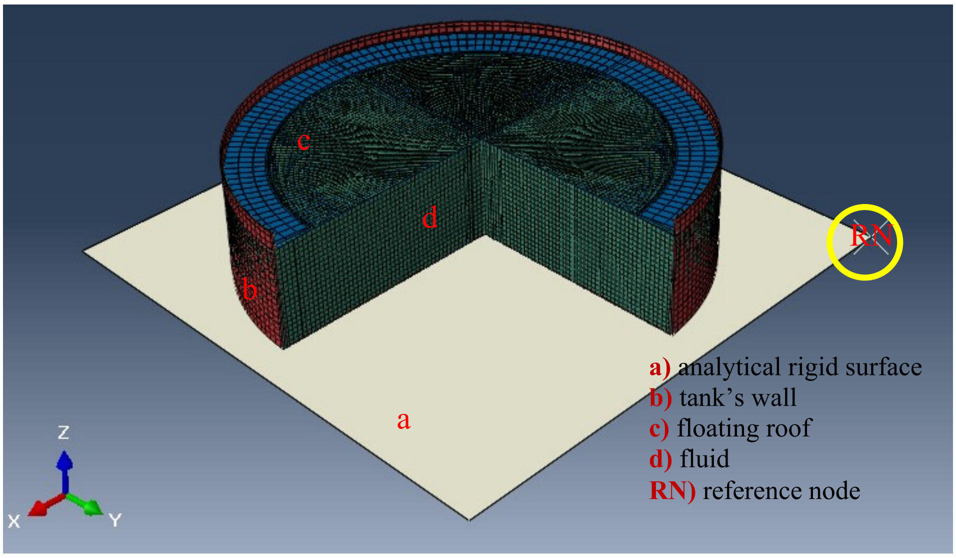

Figure 39: Section of refined FE model.

Fluid (Figure 39) modelling was performed by means of adaptive meshing analysis. Adaptive meshing in Abaqus combines the features of pure Lagrangian analysis and pure Eulerian analysis, often referred to as Arbitrary Lagrangian-Eulerian (ALE) analysis. The liquid was modelled by the three-dimensional solid element C3D8R, which is a general-purpose brick element defined by eight nodes. The fluid material, except for other parameters such as density and dynamic viscosity, has to be defined by means of an equation of state (EOS), which can describe the material's volumetric strength. In Abaqus/Explicit, in the material definition section, there is the possibility to define an EOS material. Later on, the user has to define the type of equation desired. Concerning the present case study, a linear EOS was adopted, and it can be defined by selecting in the software Us-Up as the type of EOS wanted. This process requires the definition of three parameters: the reference speed of sound in the medium (C_0), the slope of Us-Up curve (s) and the Gruneisen ratio (Γ_0) for the material. This model can be applied to materials that also have isotropic elastic or viscous deviatoric behaviour (Dorogoy et al., 2011). Finally, density and dynamic viscosity (ρ and μ_V

respectively) were provided to the material. It is worth mentioning that material properties are temperature dependent; hence, in this case, it was assumed to be ambient temperature (20 °C). ρ and μ_V were selected according to Crittenden et al. (Crittenden et al., 2012), and C_0, was chosen according to Cutnell et al. (Cutnell & Johnson, 2009). s and Γ_0 were set to zero as reported in the Abaqus examples' manual. Table 18 briefly summarizes the content properties adopted. Adopted mesh size ranged from 1.0 to 1.5 m. The total amount of created element was 192704.

Table 18: Content material properties.

ρ [kg/m^3]	998.2
μ_V [N/m s]	$1 \cdot 10^{-3}$
C_0 [m/s]	1482
s [-]	0
Γ_0 [-]	0

Once the model is defined and assembled, contact properties and interactions must be defined. The present case study involves three contact pairs: one is the friction between the tank's bottom plate and the ground, the second one involves the floating roof edge and the inner part of the tank wall, and the last one is represented by the frictionless interaction between the steel storage tank and floating roof with the fluid. Several interaction definition tools are available in Abaqus/Explicit. However, because of its advantages (for further information, refer to the Abaqus user manual), the general algorithm was used. The definition of contact properties requires to set up the normal and tangential behaviour that must be realized during the interaction. For all three above-identified interactions, concerning the normal component of the contact properties, it was defined as 'hard contact', which does not allow penetration of elements but, at the same time, it allows the separation after the contact. According to this formulation, for instance, the steel storage tank base uplifting may be possible. Tangential contact behaviour in the contact property definition was provided differently for all three types of interactions. Between the tank bottom plate and the ground, a friction coefficient of μ_F 0.4 was adopted as reported by Paolacci et al. (Paolacci et al., 2018a). Contact between the floating roof edge and the inner tank wall was assumed to be frictionless (Nishi et al., 2008). Finally, a frictionless contact for the fluid and all the other parts that may be in contact with the fluid itself was adopted.

5.2.2 Verification of the refined FE model

To verify the refined FE model, a preliminary validation was performed by comparing the maximum expected wave height (h_e) calculated by the EC 8-4 (CEN, 2006) formulation (Eq. (44)) with the numerical results in the case of 90% of the filling level.

$$h_e = 0.84 R S_e(T_c)/g \quad (44)$$

where R is the steel storage tank radius, g the gravity acceleration and $S_e(T_c)$ the elastic spectral acceleration calculated at the first convective mode period (T_c) of the fluid. T_c can be evaluated as in Eq. (45) (Sivý et al., 2017).

$$T_c = 2\pi / \sqrt[2]{g \, {}^{\lambda_1}/_{R} \tanh(\lambda_1 \gamma)} \tag{45}$$

where λ_1 is the first root of the first derivative of the Bessel equation of the first kind, R is the steel storage tank radius, γ is the fluid height-steel storage tank radius ratio, and g is the gravity acceleration. Given the present case study and 90% filling level, γ and T_c are equal to 0.46 s and 11.6 s, respectively. The steel storage tank was modelled in Abaqus/Explicit as presented in section 5.2.1, with the only exception being the absence of the floating roof. An impulsive acceleration was then generated, aiming to excite mostly the first convective mode. This excitation was possible by the sinusoidal wave $sw(t)$ presented in Eq. (46).

$$sw(t) = \mathrm{A} \cdot \sin\left(\frac{2\pi}{T_c} t\right) \tag{46}$$

where the amplitude parameter A was set to 0.05 m/s^2 in order to avoid excessive sloshing, and $t \in [0 \; T_c]$.

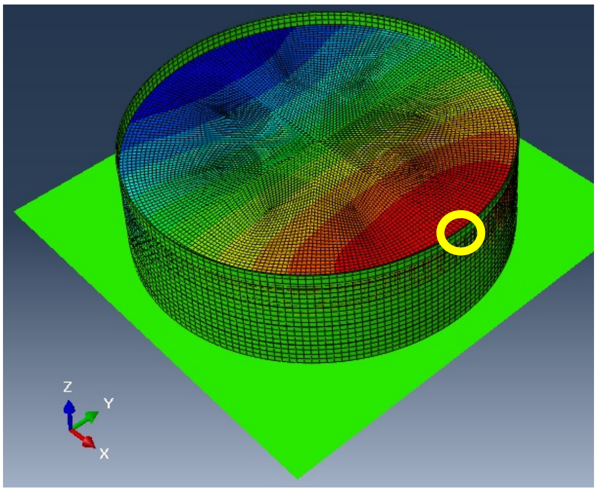

Figure 40: Steel storage tank without floating roof excited by a sinusoidal wave, (red) fluid positive vertical displacement and (blue) fluid negative vertical displacement.

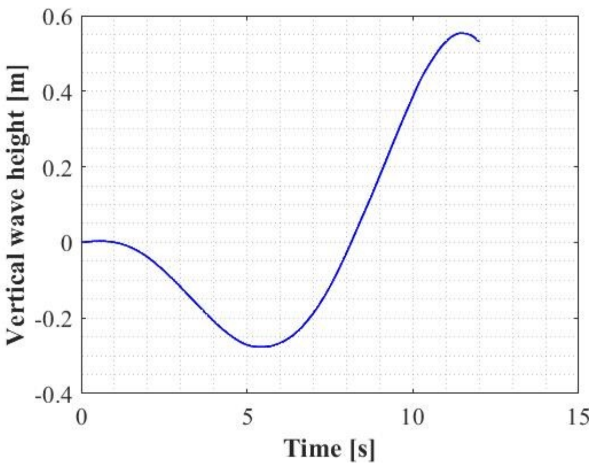

Figure 41: Vertical wave height due to the sinusoidal wave calculated at the edge of the fluid along the seismic direction (circled in yellow in Figure 40).

Figure 40 provides an image of the model subjected to acceleration $sw(t)$ in the x-direction. The vertical wave displacement was recorded at the yellow circle of Figure 40 and presented in Figure 41. Abaqus/Explicit results revealed a maximum vertical wave height of 0.55 m whereas h_e, the maximum expected by Eq. (44), was 0.56 m. Due to the low difference between the two values (1 cm, which corresponds to a wave underestimation of approximately 2%), one can sufficiently rely on the developed model.

Summarizing the evidences of this section, the vertical displacement obtained by the Eurocode formula was in good agreement with the results of the refined FE model provided that the presence of the floating roof was disregarded in the refined FE model.

5.2.3 Seismic response of floating roof by simplified and refined FE models

The seismic response of the floating roof was simulated by the simplified (see Chapter 3) and refined FE models (see section 5.2.1). These simulations are aimed at providing insight into both modelling approaches. Only the 90% filling level was taken into account in these simulations because of the highest risk of overtopping and because the selection of ground motions becomes more challenging in the case of the lower filling level. Namely, the convective period increases by reducing the filling level, which may cause an issue in ground motion selection based on spectral acceleration at the convective period. Further on, the seismic excitation, which causes overtopping in the case of lower filling levels, is directly related to higher ground motion intensities. Therefore, it can be considered reasonable to verify the most vulnerable case with the less uncertain ground motions.

The refined FE model was used to check the tank sliding, base uplifting, and the potential delamination between the floating roof and fluid. The base uplifting was monitored at points A and B depicted in Figure 42, whereas the lateral displacement of the tank along the seismic direction was checked in point C (Figure 42). The tank was subjected to ground motion based on the sinus wave (Eq. (10)) in the X direction (red arrow Figure 44). The resulting lateral displacement history in point C and vertical displacement histories in points A and B are presented, respectively, in Figure 43 (a) and Figure 43 (b). Figure 43 (a) clearly shows the absence of any sliding between the analytic rigid surface and steel storage tank, given the fact that the lateral displacement of RN and C was the same. At the same time, the base uplifting calculated at A and B was practically negligible (Figure 43 (b)), whereas the vertical displacement in point D was substantial, as demonstrated in Figure 45. Both simplified and refined FE models predicted the maximum vertical displacement of approximately 0.55 m (Figure 45). Note also that the refined FE model confirms the perfect contact between the floating roof and fluid.

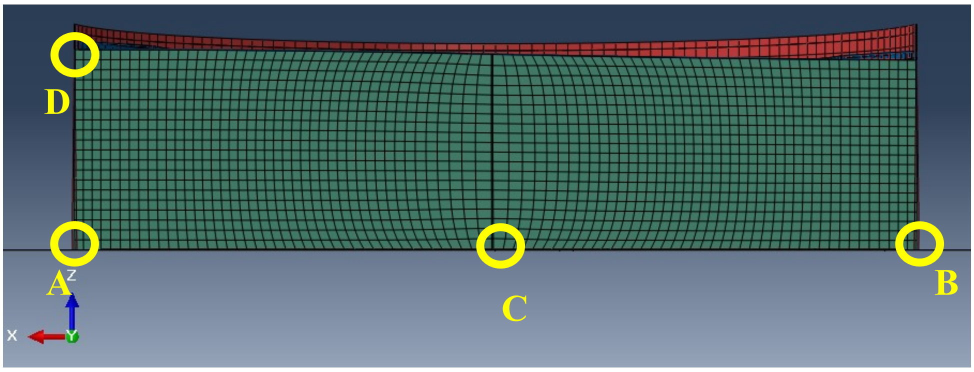

Figure 42: Refined FE model diametric cut section view.

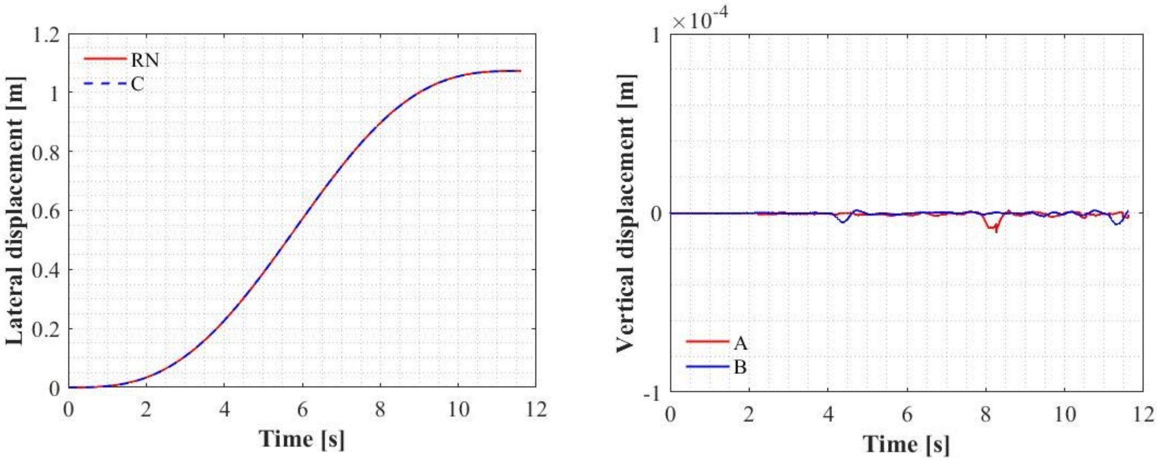

(a) (b)

Figure 43: (a) refined FE model lateral displacement and (b) base vertical displacement.

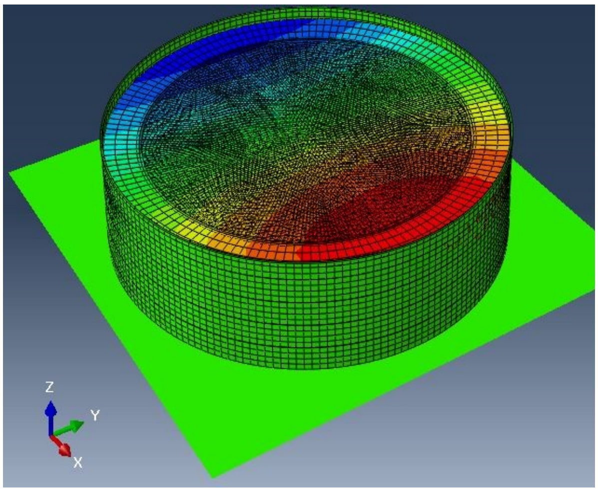

Figure 44: Steel storage tank with a floating roof excited by a sinusoidal wave with an indication of positive vertical displacement (red) and negative vertical displacement (blue).

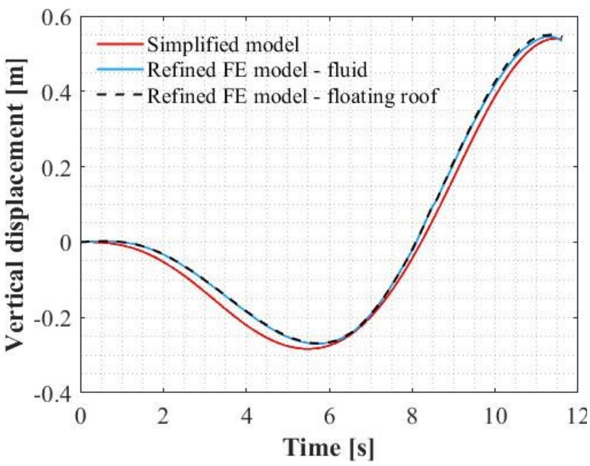

Figure 45: Vertical displacement history of floating roof and fluid based on refined FE model and the floating roof vertical displacement history based on the simplified model.

Moreover, an almost perfect match in terms of vertical displacement between simplified and refined FE models is reached, ensuring the quite reasonable reliability of the first model. However, it is worth noting that the ground motion provided by Eq. (46) was defined in such a manner to excite the first convective mode only. Therefore, the tank was then subjected to a real ground motion (Figure 46) aiming to investigate the influence of higher modes, mostly on the vertical displacement response. The results of simulation by the refined FE model indicated that the lateral displacement history of RN and that at point C are practically equal (Figure 47 (a)), which means that also in this case, no sliding occurred between the steel storage tank and the analytic rigid surface. At the same time, as remarked in Figure 47 (b), practically no tank base uplifting was observed.

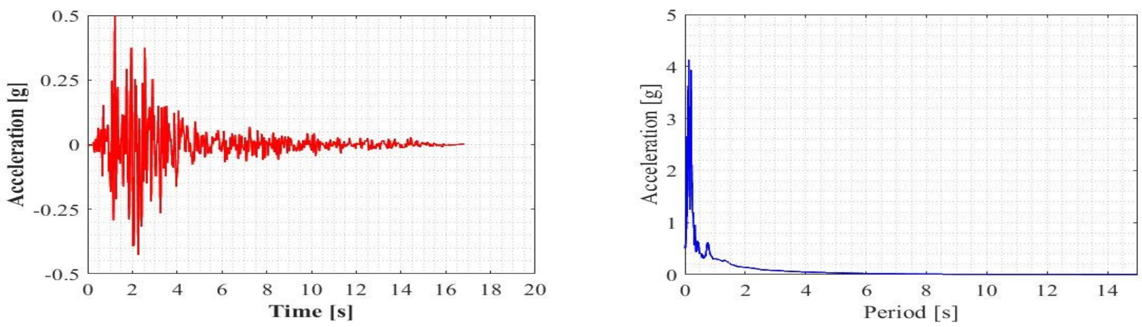

(a) (b)

Figure 46: (a) acceleration history of ground motion and (b) spectral shape of adopted ground motion for model validation.

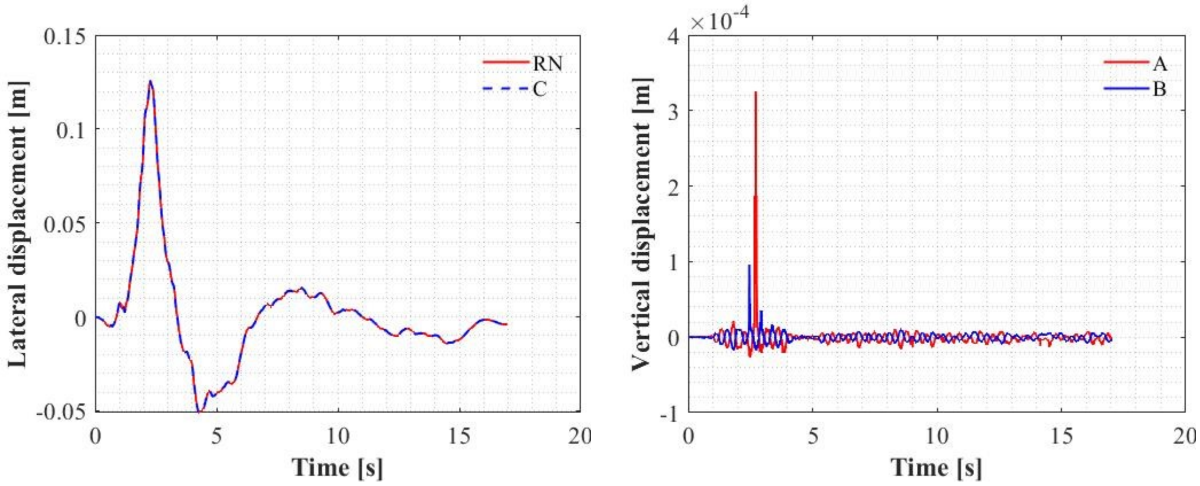

(a) (b)

Figure 47: (a) lateral displacement history and (b) base vertical displacement history simulated by refined FE model based on ground motion excitation.

Figure 48 presents the vertical displacement history simulated by the refined FE (calculated at point D, see Figure 42) and simplified model. Under the seismic action of the ground motion, the response of these models does not match perfectly at particular time intervals, especially from six to ten seconds. Furthermore, a slightly scattered response (Figure 48 (a)) in the refined FE model is evident, even though the maximum vertical displacement is highly similar in both modelling approaches.

A match of the results could be improved if the number of considered modes would have been increased in the simplified model. However, the more modes are considered, the more computational effort is required. This would lead, consequently, to the loss of the meaning of a simplified model that accounts for the computational efficiency as a key aspect. In this respect, a good compromise between computational efficiency and results accuracy has to be reached, accounting for the analysis purposes. Concerning the present study, as introduced in the previous sections, because the goal is to focus on the fluid overtopping and consequently loss of containment, the maximum vertical displacement is the most relevant outcome besides the computational speed. Indeed, because a large amount of simulations is necessary, a time-saver approach is crucial.

The scatter in the refined FE model response reflects the consequence of the stiffness of the tank wall over the contained fluid. The amplitude of vertical convective displacement is practically not affected by the tank wall stiffness (Malhotra et al., 2000) due to the significant difference between the most relevant oscillating periods of both the fluid and steel storage tank, as highlighted in the comparison presented in Figure 48 (a) and (b). However, assuming a rigid body constraint for the tank wall in the refined FE model, no more scattering in the response is observable (Figure 48 (b)). The reason for this behaviour relies on the fact that higher oscillating fluid modes may become close in periods with the main ones of the tank wall. In this case, the effect of the tank wall vibration may affect, even if not practically relevant, the fluid response (Figure 48 (a)). Under these premises, the adopted simplified model is considered to be sufficiently reliable with respect to the present study purposes.

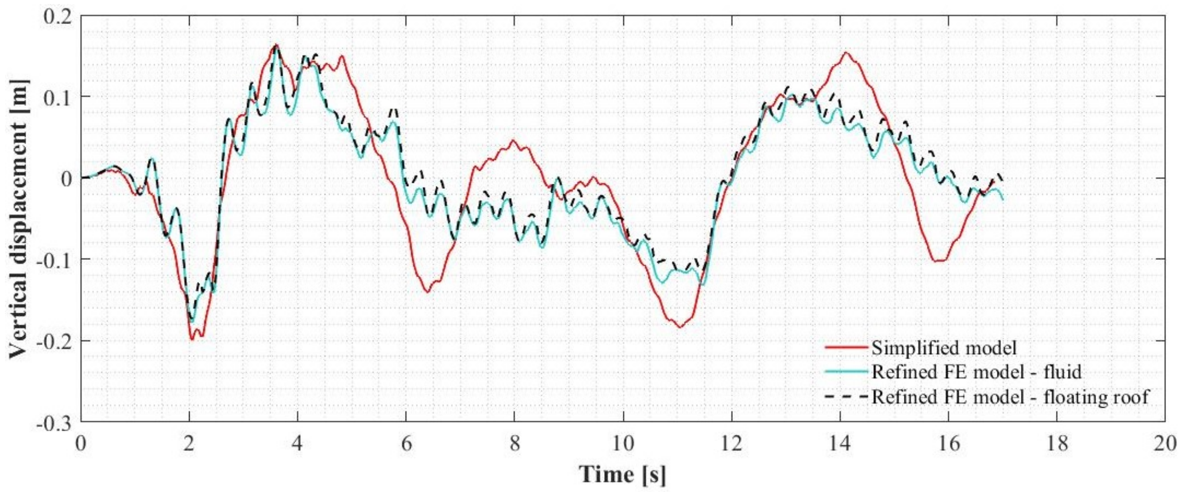

(a)

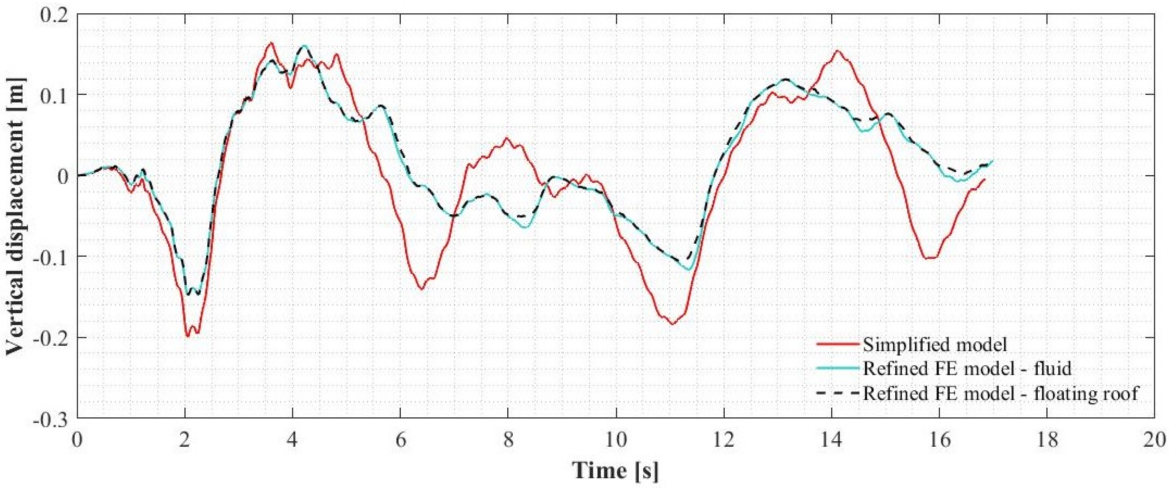

(b)

Figure 48: Vertical displacement of floating roof and fluid for refined FE model and simplified model response with consideration of (a) flexible tank wall and (b) rigid tank wall.

Concerning the present case study, the assumptions in formulating the simplified model were checked. It was shown that they caused a negligible effect on the seismic response of the investigated tank. In particular, the tank wall stiffness, the tank sliding, the rigid rocking and fluid-floating roof delamination have a negligible influence on the maximum vertical displacement. However, these conclusions refer to only 90% filling level of the tank. Although additional analyses were performed for the tank filled up to 80% and shown that the seismic response of the floating roof was adequately simulated, further studies are needed to understand the limitation of the simplified model better. For example, different parametric studies concerning the content height – aspect ratio, geometrical characteristics and other input parameters that affect the seismic response of the floating roof should be performed to provide an insight into the capability of the simplified model. The maximum vertical displacements provided by the simplified and refined FE model (flexible tank wall) were very similar in the case of the monochromatic wave and for the seismic excitations using recorded ground motion (Table 19). Because the loss of containment due to large vertical displacements is the main objective of the present study, the accuracy and reliability of the simplified model were considered adequate. However, further investigations may be desirable, mostly investigating the influence of storage tanks geometrical properties, stiffness and other input parameters of the model.

Table 19: Maximum vertical displacement provided by the simplified model and maximum vertical displacement for fluid or floating roof provided by the refined FE model for monochromatic wave and recorded ground motion.

Model	**Maximum vertical displacement [m]**	
	Monochromatic wave	**Ground motion**
Simplified	0.54	0.16
Refined FE	0.55 (fluid)	0.16 (fluid)
Refined FE	0.55 (floating roof)	0.16 (floating roof)

5.3 Calibration of the simplified numerical model of the steel storage tank

In this section a simplified model capable to easily perform the seismic response history analyses of the steel storage tank with particular attention to its wall is presented and calibrated by the refined FE model. Only the filling levels of 90%, 80% and 70% were considered. The simplified model herein presented was based on the joystick model introduced in Chapter 2, without the supporting structure. However the stick model of Chapter 2 can be easily improved accounting for base uplifting and sliding. Indeed, past works (Malhotra & Veletsos, 1994; Vathi & Karamanos, 2017; Phan & Paolacci, 2018) analysed the uplifting phenomenon providing procedures to calibrate and improve the stick model of Chapter 2.

The simplified model (Figure 49) was coded in OpenSees (McKenna & Fenves, 2010). It comprises lumped masses simulating impulsive (m_i), convective (m_c) and structural (m_s) (e.g. tank's wall and roof) masses. Impulsive and convective masses were connected by means of elastic cantilevers with appropriate stiffness (k_i and k_c, T_i and T_c, respectively, for impulsive and convective stiffness and periods respectively), damping and length. Structural masses were rigidly connected to the base and placed at the centre of gravity of the steel storage tank. Damping ratios adopted were 2% for the impulsive mass and 0.5% for the convective one (Malhotra et al., 2000). To provide the capability of simulating the base uplifting and the base sliding, a rotational spring and frictional behaviour were provided to a zero-length element (Figure 49) available in the OpenSees software (McKenna & Fenves, 2010) by means of a multi-linear material (OpenSees, 2017). In Figure 49, a representation of the simplified model is presented.

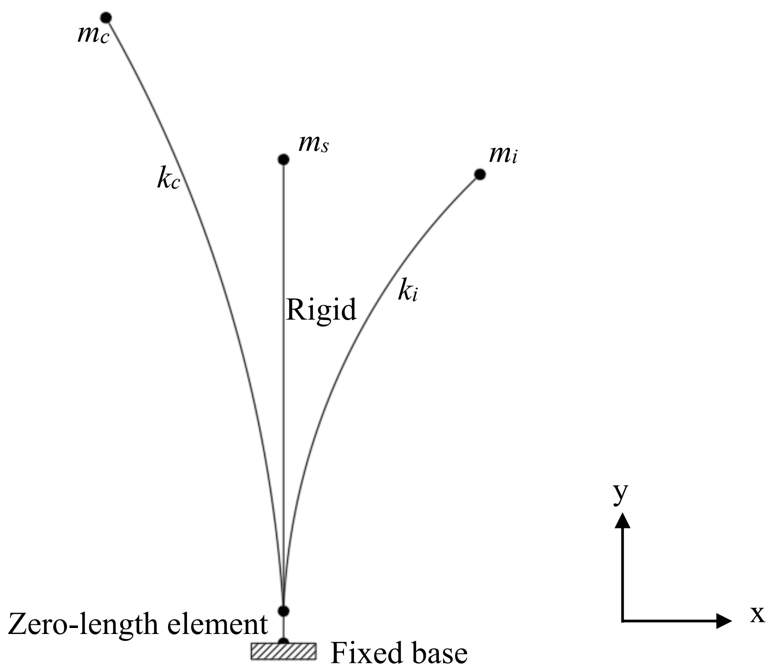

Figure 49: Simplified model (deformed shape view) for the simulation of seismic response of steel storage tanks including uplifting and sliding.

The most relevant aspect of the simplified model is the definition of the rotational spring and the friction behaviour to be provided to the zero-length element at the model base. Zero-length element has the capability to be assigned with different material properties and behaviour for each degree of freedom available in the model. In this case study a two-dimension model was coded, with a lateral translational and a rotational degree of freedom around the vertical axes of the tank. The vertical degree of freedom (Y in Figure 49) was blocked by imposing to have the same degree of freedom of the fixed node at the base (Figure 49) which was totally fixed. Lateral degree of freedom (X in Figure 49) was constrained by assigning to the zero-length element an elastic-perfect plastic material in which the initial stiffness (E in Figure 50) was selected as high as possible and then the maximum force (F_{max} in Figure 50) evaluated by means of a friction coefficient of μ_F 0.4 (Paolacci et al., 2018a) as described in the previous section (see section 5.2.1).

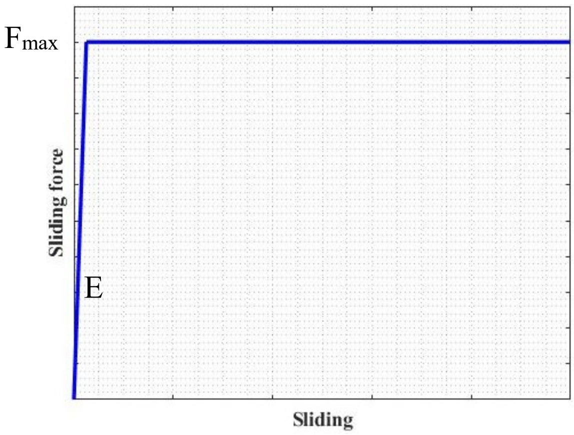

Figure 50: Sliding resistance force for the simplified model.

The definition of the rotational spring is not straightforward. For this purpose, a refined FE model was developed in Abaqus (Dassault Systemes, 2019) on the basis of the model introduced in section 5.2, but with disregarding the fluid and the floating roof. The load effects were simulated by applying gravity load (Figure 51 (a)), hydrostatic (Figure 51 (b)), the impulsive (Figure 51 (c)) and the convective (Figure 51 (d)) pressures to the model. Only the first impulsive and convective natural vibration modes were considered being the most relevant, as also suggested in the EC 8-4 (CEN, 2006). Finally, by increasing the impulsive and convective pressures, a push-over analysis was performed. Adopted pressure profiles were defined according to the formulation of the EC 8-4 (CEN, 2006).

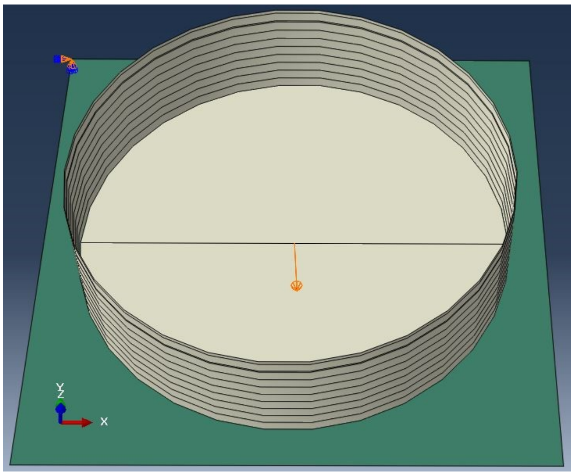

(a)

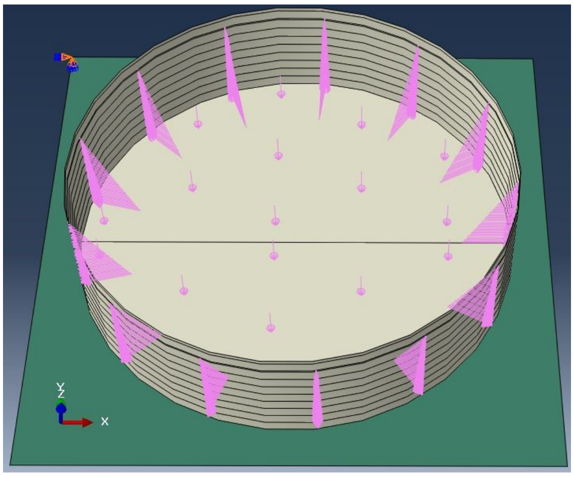

(b)

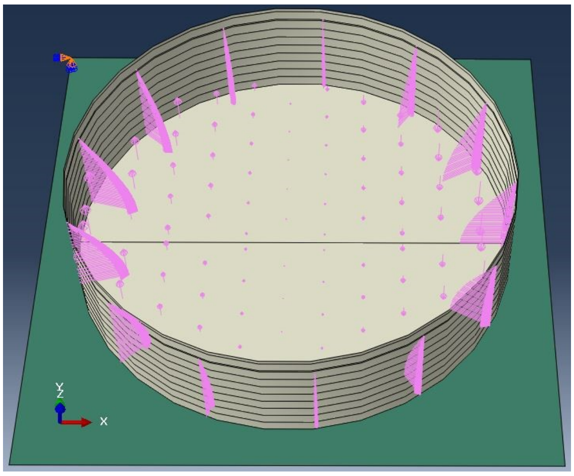

(c)

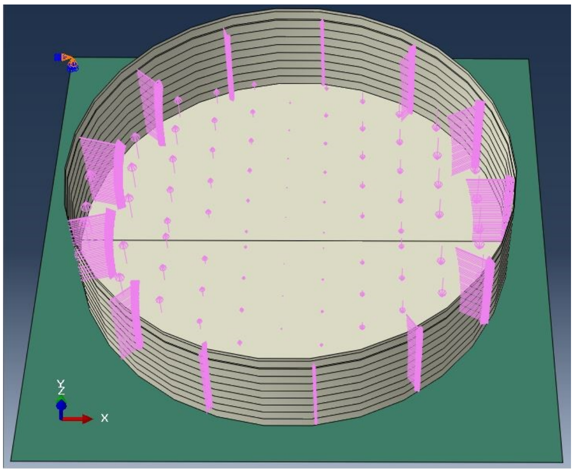

(d)

Figure 51: Refined FE model loads (a) gravity load, (b) hydrostatic pressure, (c) impulsive pressure and (d) convective pressure.

During the push-over analysis the steel storage tank experienced a base uplifting which was recorded (Figure 52) from which, under the assumption of rigid base (Malhotra & Veletsos, 1994), the rotation was calculated. Finally, the moment-rotation behaviour was linearized and provided to the zero-length element for the rotational degree of freedom by means of a multi-linear material (OpenSees, 2017).

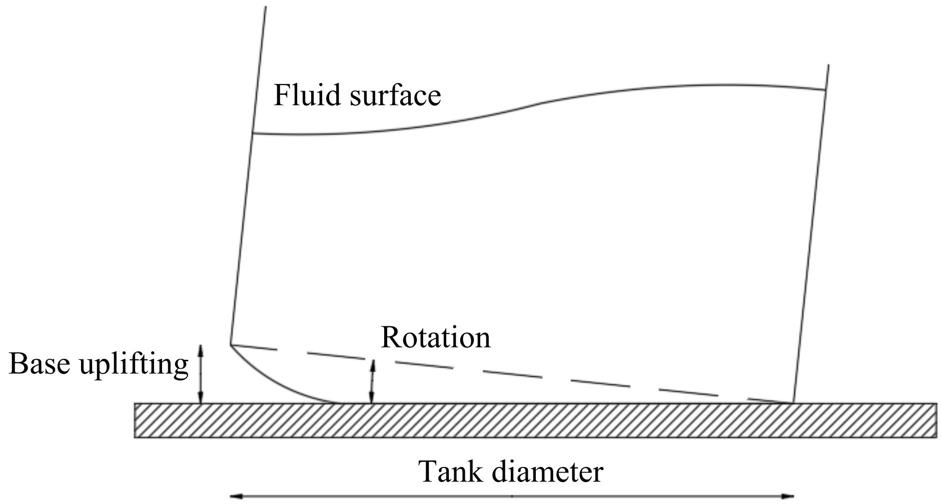

Figure 52: Base uplifting and rotation for an ideal steel storage tank subjected to pushover analysis.

In the following (Table 20) the model parameters calculated for the considered filling levels with the correspondent moment-rotation curves (Figure 53).

Table 20: Simplified model parameters for the considered filling levels.

Filling level	m_i [kg]	h_i [m]	T_i [s]	k_i [N/m]	m_c [kg]	h_c [m]	T_c [s]	k_c [N/m]
90%	$3.02 \cdot 10^7$	7.2	0.40	$2.34 \cdot 10^9$	$7.82 \cdot 10^7$	10.5	11.6	$7.21 \cdot 10^6$
80%	$2.38 \cdot 10^7$	6.4	0.38	$2.12 \cdot 10^9$	$7.22 \cdot 10^7$	9.2	12.2	$6.16 \cdot 10^6$
70%	$1.81 \cdot 10^7$	5.6	0.34	$1.92 \cdot 10^9$	$6.55 \cdot 10^7$	7.9	12.8	$5.06 \cdot 10^6$

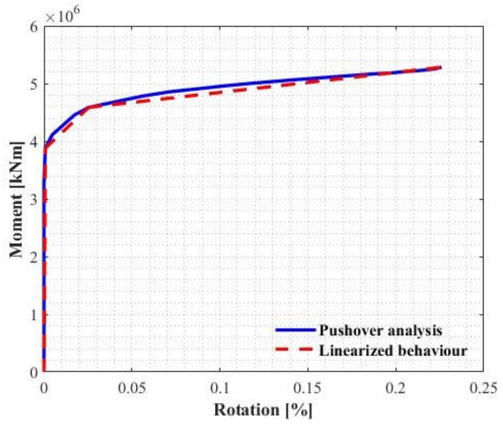

(a)

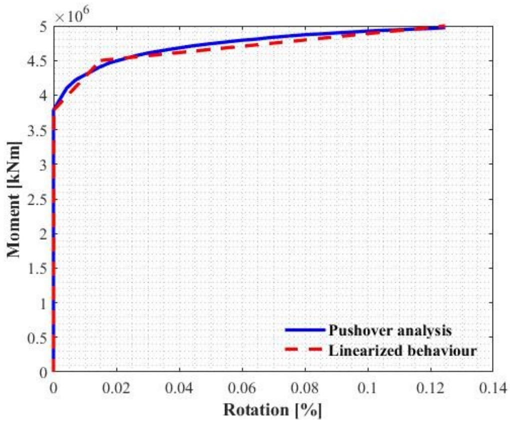

(b)

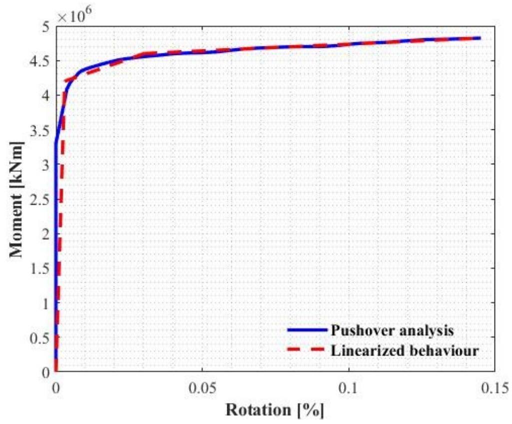

(c)
Figure 53: Moment-rotation curves for (a) 90%, (b) 80% and (c) 70% of filling levels.

5.4 Ground motion selection and definition of overtopping limit state

First, it was intended to select ground motions by choosing the spectral acceleration at the first convective period (Eq. (45)), $S_a(T_c)$ for the intensity measure (IM). Such a decision was made because $S_a(T_c)$ is a highly efficient IM for predicting vertical roof displacement. Thus, it can be considered for the seismic fragility analysis ((Baker & Cornell, 2005; Kazantzi & Vamvatsikos, 2015; Phan & Paolacci, 2016)). However, it was not practically possible to implement such an IM. For instance, in the present case study, T_c was equal to 11.6 s in the case of a 90% filling level. It is important to consider that such a long period is not accounted for in most of the ground motion prediction equations (GMPEs) used for the characterization of the site seismic hazard, (Abrahamson & Silva, 1997; Atkinson & Boore, 2003; Campbell & Bozorgnia, 2008; Chiou & Youngs, 2008). Thus, we were seeking an alternative IM. Because the spectral acceleration at the period of 4 s is often used in GMPE equations and consequently in probabilistic seismic hazard analysis, it was decided to adopt this IM for the ground motion selection and fragility function. The seismic hazard functions for the selected IM ($S_a(T = 4s)$) at Priolo Gargallo are presented in Figure 54, aimed at demonstrating the impact of the GMPEs on the seismic hazard function. Grey lines represent the hazard curves due to each of the GMPEs adopted, whereas the red dashed line represents the mean hazard function that results from the weighted average of all the others. Each GMPE has its own weight used in the seismic hazard computing logic tree by the SHARE project (Woessner et al., 2015).

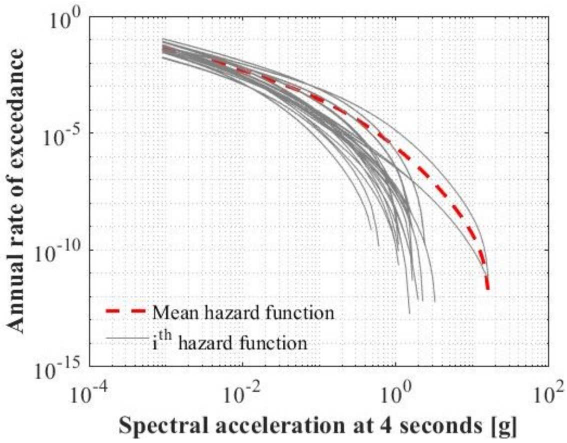

Figure 54: Hazard function for Priolo Gargallo for $S_a(T = 4\text{s})$.

Because probabilistic seismic hazard analysis provides uniform hazard spectra only up to the period of 4 s, it was impossible to define a hazard-consistent target spectrum for the interval of periods in the vicinity of T_c=11.6 s. Therefore, ground motion selection for fragility analysis was based on an earthquake scenario characterized by a mean magnitude (M) and source-to-site distance (R) obtained from the disaggregating $S_a(T = 4s)$ corresponding to a return period of 475 years. In this respect, the $S_a(T = 4s) = 0.02\ g$ was obtained from the hazard curve at an occurrence rate of 1/475 per year, and the mean magnitude and distances were estimated to be 6.9 and 37 km, respectively. Subsequently, the seismic scenario based on the magnitude and distance was used for selecting the preliminary set of compatible ground motions from the NGA-West 2 database (Ancheta et al., 2014). However, in some cases, we had to remove ground motions due to the filtering approach used in the signal post-processing, although they were consistent with the prescribed criteria of ground-motion selection. Indeed, records, particularly those from old recording instrumentations, were affected by disturbances in the signal, both in the range of high and low frequencies (Boore & Bommer, 2005). As a consequence, those ground motions were filtered; thus, they were considered inappropriate for this study. For each ground motion in the NGA-West 2 database, the so-called lowest usable frequency (LUF) is defined. LUF generally depends on the instrumentation adopted in signal recording, sampling rate and noise level (Ktenidou et al., 2016). Within the preliminary set of ground motion extracted from the database, only the ground motions with LUF equal or lower to the one corresponding to T_c were selected in order to ensure the correct frequency content of the selected signal. In Table 21, all the selected ground motions are presented beside the corresponding year of the event, M, R and LUF. Later on, selected ground motions were scaled in order to match the spectral acceleration of 0.02 g at 4 seconds (see Table 21). It is worth noting that although some records belong to the same event, the recording stations were different in order to avoid signal replication.

Figure 55 presents the spectra of the selected ground motions and the average spectrum, with particular emphasis on the T_c related to the 90% filling level case. The same behaviour is observable even for the other considered filling levels.

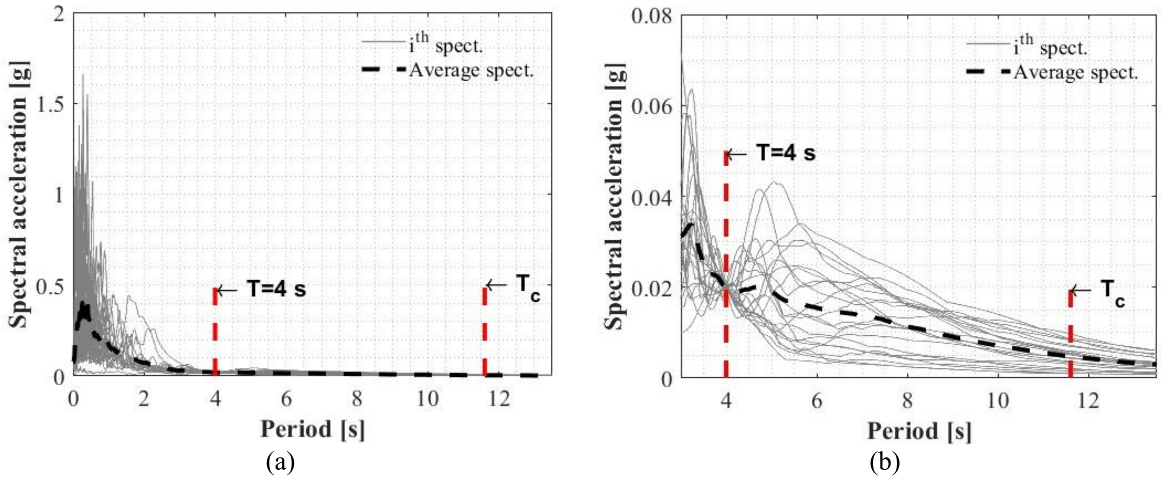

Figure 55: Spectral shape of normalized ground motions to S_a at 4 s for (a) the entire period interval and (b) the period range above 4 s.

Table 21: List of selected ground motions with corresponding year, magnitude M, distance R, lowest usable frequency LUF and scaling factors.

Earthquake name	#	Year	M	R [km]	LUF [hz]	Scaling factors
'Loma Prieta'	1	1989	6.93	35.49	0.084	1.01
'Chi-Chi_ Taiwan'	2	1999	7.62	38.42	0.0625	0.40
'Chi-Chi_ Taiwan'	3	1999	7.62	35.68	0.05	0.20
'Chi-Chi_ Taiwan'	4	1999	7.62	35	0.0375	0.23
'Chi-Chi_ Taiwan-03'	5	1999	6.2	36.99	0.0375	1.36
'Chi-Chi_ Taiwan-03'	6	1999	6.2	38.47	0.04	1.88
'Chi-Chi_ Taiwan-03'	7	1999	6.2	37.04	0.03	1.23
'Chi-Chi_ Taiwan-03'	8	1999	6.2	38.72	0.08	0.79
'Chi-Chi_ Taiwan-03'	9	1999	6.2	35.93	0.045	0.49
'Chi-Chi_ Taiwan-03'	10	1999	6.2	35.9	0.075	0.75
'Chi-Chi_ Taiwan-04'	11	1999	6.2	38.14	0.03	0.53
'Chi-Chi_ Taiwan-04'	12	1999	6.2	38.35	0.03	0.54
'Chi-Chi_ Taiwan-05'	13	1999	6.2	38.98	0.05	0.26
'Chi-Chi_ Taiwan-06'	14	1999	6.3	36.57	0.03	1.89
'Chi-Chi_ Taiwan-06'	15	1999	6.3	38	0.085	4.50
'Chi-Chi_ Taiwan-06'	16	1999	6.3	38.62	0.05	1.77
'Chi-Chi_ Taiwan-06'	17	1999	6.3	38.34	0.055	2.95
'Chi-Chi_ Taiwan-06'	18	1999	6.3	37.92	0.04	2.50
'L'Aquila_ Italy'	19	2009	6.3	37.16	0.025	1.18
'Chuetsu-oki_ Japan'	20	2007	6.8	36.79	0.075	3.11
'Iwate_ Japan'	21	2008	6.9	38.06	0.025	1.62
'Iwate_ Japan'	22	2008	6.9	38.91	0.025	0.49

In addition to the careful selection of ground motions, special attention was given to the definition of limit state for fragility analysis. Concerning sloshing in tanks, EC 8-4 (CEN, 2006), clearly states that *'Freeboard at least equal to the calculated height of the slosh waves shall be provided, if the contents are toxic, or if spilling could cause damage to piping or scouring of the foundation'*. However, according to (Pantusheva, 2017), a suitable definition of a limit state (LS) related to the loss of containment due to large vertical floating roof displacement is not straightforward and thus still a subject of research.

In this respect, due to the severe consequences owing to the loss of containment, the LS was set in such a way that the top part of the outer floating roof rim reaches the top of the steel storage tank's edge. In the present case, the overtopping limit state was controlled by the minimum freeboard height of the tank. Note that the freeboard height was defined as the distance between the top of the tank's wall and the top of the outer rim of the pontoon (see Figure 38 (a)). The height of the outer rim of the pontoon is 1 m (see Figure 38 (b)), and it is deputed to the sealing gasket connection. According to the present LS definition, a certain amount of sealing is still guaranteed, and the eventual pop-out of sealing is avoided, being on the safe side.

5.5 Ground motion selection and definition of tank wall limit state

The most common target spectrum for ground-motion selection is the uniform hazard spectrum (UHS) but it has been found unsuitable as it conservatively implies that large-amplitude spectral values will occur at all periods within a single ground motion (GM) (Baker, 2010). Hence, in the following, the conditional spectrum (CS) was used. The spectral acceleration (S_a) at the first impulsive period for 90%, 80% and 70% of filling level were assumed as the ground motion IM for the selection of GMs (see Table 20). Ground motions were selected according to the algorithm proposed by Jayaram (Jayaram et al., 2011). All sets of GMs were selected from the strong ground motion database, which contains 9188 ground motions from the NGA (Chiou et al., 2008) and the RESORCE (Akkar et al., 2014) database. The two databases were recently combined by the Institute of Structural Engineering, Earthquake Engineering and Construction IT (IKPIR) by (Šebenik & Dolšek, 2016). The selected GMs correspond to events within 5 – 48, 8 – 46 and 10 – 50 km and magnitudes 4.8 – 7, 5.2 – 7 and 5 – 7 for 90%, 80% and 70% of filling level respectively. Ground motions have been selected based on conditional target spectra (CS) and it was defined by using the results of SHARE project (Woessner et al., 2015). The CS (Figure 56) was defined based on the results of the seismic hazard disaggregation for the site and by adopting the mean return period of 475 years. Later on, GMs were scaled in order to match the spectral acceleration at the selected fundamental period which correspond to 0.46, 0.48 and 0.52 g for 90%, 80% and 70% of filling level respectively.

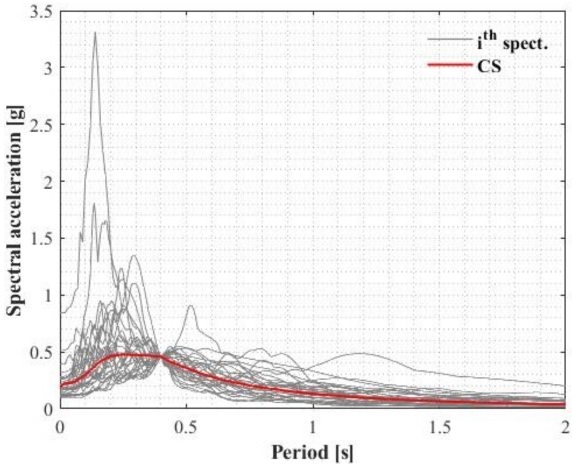

(a)

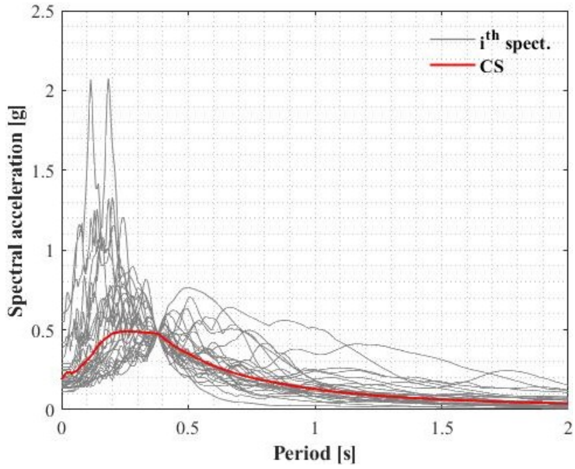

(b)

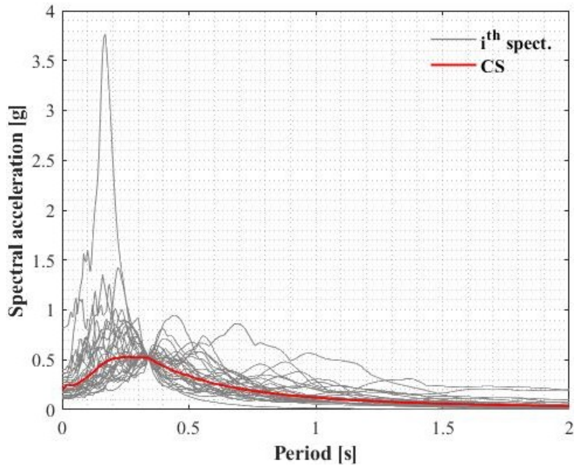

(c)

Figure 56: Spectral shape of normalized ground motions to S_a at first impulsive period (a) 90%, (b) 80% and (c) 70% of filling level.

After a proper selection of ground motions, attention was paid to the definition of the tank wall limit state (LS) to be used, later on, in the fragility analysis. Hazardous consequences are related to the loss of containment (Paolacci et al., 2018b) which may endanger the surrounding environment, human lives and can cause catastrophic economic drawbacks. In this respect, because the loss of containment (LOC) may be related to the wall cracking due to buckling phenomena, the so-called elephant’s foot buckling (EFB) has been considered the most relevant phenomena, which may cause LOC due to the wall cracking.

API 650 (American Petroleum Institute, 2012) provides different stress-based definitions of the selected LS depending on the ratio GHD^2/t^2 where G is the specific gravity of the liquid (the liquid was assumed to be water, hence, $G = 1$), H is the maximum height of the liquid in metres, D is the tank diameter in metres and t is the thickness of the shell ring under consideration in millimetres.

Instability phenomena, e.g. the EFB, are triggered by the increase of the axial compressive stress in the tank wall due to the base uplifting (Malhotra et al., 2000). Hence, the most affected shell courses of the tank wall by the EFB are the bottom ones. In this respect, in order to compute the aforementioned ratio, the lower courses thickness have to be taken into account. Based on the aforementioned ratio, the code (American Petroleum Institute, 2012) provides two different criteria for the LS Eqs. (47a) – (47b), where F_c stands for allowable longitudinal shell-membrane compression stress in MPa.

When $GHD^2/t^2 \geq 44$

$$F_c = 83\ t_s/D \tag{47a}$$

Otherwise, when $GHD^2/t^2 < 44$

$$F_c = 83\ t_s/(2.5\ D) + 7.5\sqrt{GH} < 0.5F_y \tag{47b}$$

Where t_s is the thickness of the bottom shell course and F_y is the minimum specified yield strength of the bottom course.

5.6 Seismic fragility analysis

Seismic fragility analysis was performed by considering LSs related to the excessive vertical displacement of the floating roof and the elephant's foot buckling phenomenon, which affects the tank wall. However, in both cases, the filling level of a steel storage tank may vary during the lifetime according to the industrial needs. Consequently, this parameter may have a particular influence on the fragility analysis. In this respect, the fragility analysis should be performed for many different filling levels. However, it is worth remarking that the fragility analysis was performed only for 90%, 80%, and 70% filling levels. The reason for this choice is related to different aspects, which are described in the introduction of this Chapter.

5.6.1 Floating roof

The fragility functions $P[B \mid A_i, IM = im]$, which define the probability of exceeding the designated limit state B for the *i-th* filling level A_i and the seismic intensity $IM = im$, were evaluated by means of two different approaches. In the first approach, the simplified model, which includes the floating roof, was used in the incremental dynamic analysis (IDA) (Vamvatsikos & Fragiadakis, 2010), with the set of ground motion presented in section 5.4. The IM selected was the spectral acceleration at 4 seconds; the engineering demand parameter (EDP) was the floating roof maximum vertical displacement, which can occur either at *Pos* 0 or π radiant at *RPos* equal to the floating roof radius, as described in Chapters 3 and 4. In the second approach, Eq. (44) was used to calculate the maximum vertical displacement due to the same set of ground motion of IDA but unscaled. It is worth remarking that Eq. (44) strictly neglects the presence of the floating roof, considering the fluid with a free surface. The exceedance of the LS for each ground motion was calculated by assuming a linear seismic behaviour of the tanks and evaluating mean and dispersion by assuming a lognormal distribution, as in the first approach. Demand curves and fragility functions are presented in Figure 57 for a filling level of 90% ((a) and (b)), 80% ((c) and (d)) and 70% ((e) and (f)).

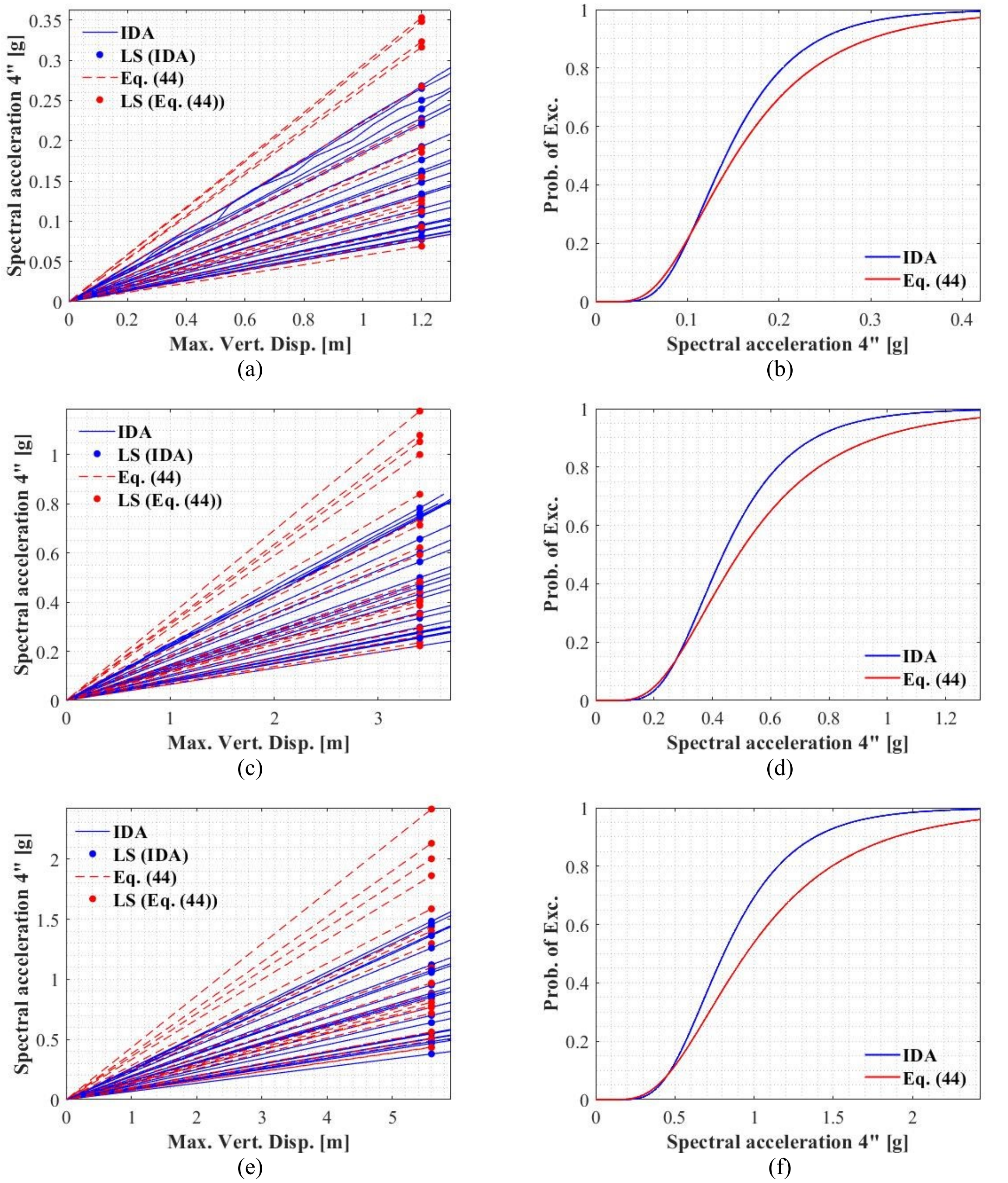

Figure 57: (a) IDA curves and (b) fragility curves for 90% of filling level, (c) IDA curves and (d) fragility curves for 80% of filling level, and (e) IDA curves and (f) fragility curves for 70% of filling level.

Figure 57 revealed that IM causing overtopping was estimated at a particularly high value for some ground motions. Additionally, the IM causing overtopping based on Eq. (44) was overestimated mainly for those ground motions that caused overtopping at the highest IM values. To investigate the reasons behind this particular phenomenon, four ground motions that produced the largest differences in the estimated IMs, which caused overtopping based on the two adopted approaches, were identified. The difference in IDA curves for the tank with 90% filling level and these particular ground motions (i.e. the ground motion 5, 13, 21 and 22) are presented in Figure 58. The values of IM causing overtopping are elaborated in Table 22 together with the percent differences (in %) for the IMs causing overtopping based on IDA or Eq.(44).

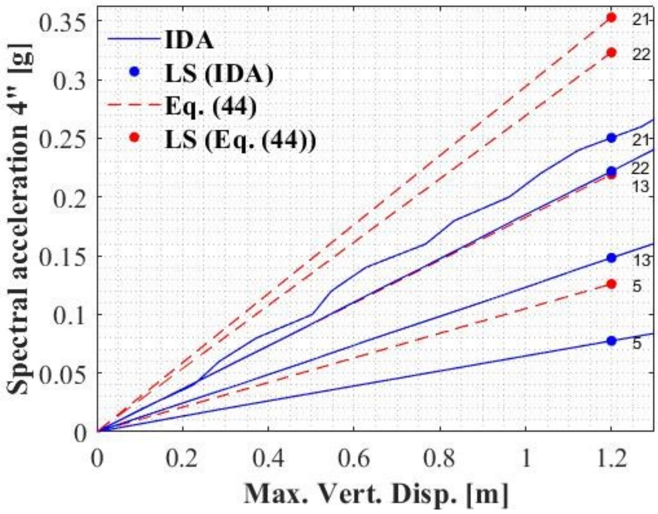

Figure 58: IDA curves for selected ground motions in the case of 90% filling level and approximate linear IDA curve estimated by utilizing Eq.(44).

Table 22: Values of IM causing overtopping for ground motions 5, 13, 21 and 22 based on IDA and by utilizing Eq. (44), and corresponding percent differences for the tank filled with liquid to 90%.

	#5	#13	#21	#22
Eq. (44) [g]	0.1259	0.2193	0.3531	0.3233
IDA [g]	0.0775	0.1482	0.2505	0.222
%	-38%	-32%	-29%	-31%

To investigate what caused the difference in the estimated vertical displacement, the seismic response of the floating roof was further investigated for the four identified ground motions. For this purpose, the ground motions were scaled to 0.02 *g* at period *T*=4 *s*. A single stripe analysis was performed, aiming to investigate the seismic response of the single ground motion. The results in terms of maximum vertical displacement were obtained by a) using Eq. (44), b) the simplified model accounting for one mode and neglecting the presence of the floating roof, c) the simplified model accounting for one mode only and d) the simplified model accounting for eight modes. To exclude the floating roof in the analyses, its mechanical and geometric properties were artificially modified (e.g., extremely low material density, Young's modulus and floating roof thickness).

The results of the analysis are reported in Table 23 and were obtained for a 90% filling level of the tank. The simplified model without the floating roof provided quite similar results as those obtained for case a), whereas for case b), a slight difference in terms of vertical displacement was observed, but only for the ground motion number 5. Case d) showed the higher vertical displacement, demonstrating the influence of the higher modes on the overall response. This phenomenon occurs because spectral accelerations for some ground motions are high at higher modes of the floating roof (see Figure 59). High accelerations associated with higher modes cause an increase of the maximum vertical displacement of the floating roof. This effect cannot be captured by Eurocode formula (Eq. (44)), because it accounts only for the first convective mode and disregards the presence of the floating roof. The effect of higher modes on the average value of maximum vertical displacement may not be large. However, for some specific ground motions, the higher modes effects should not be disregarded as can be observed in Table 23 for ground motion #5, #13, #21 and #22 where the maximum vertical displacement estimated according to the Eurocode formula and by simplified model considering 8 modes are reported. If the higher modes effect is disregarded, the IM causing the exceedance of LS can be overestimated, as demonstrated in Figure 58.

Table 23: Maximum vertical displacements of the roof calculated for the four identified ground motions by means of the four considered approaches.

Approach	Maximum vertical displacement of the roof for different ground motions			
	#5	**#13**	**#21**	**#22**
a) Eq. (44)	0.19	0.11	0.07	0.07
b) Simp. model – 1 mode no roof	0.21	0.11	0.08	0.08
c) Simp. model – 1 mode	0.24	0.12	0.07	0.08
d) Simp. model – 8 modes	0.30	0.16	0.09	0.11

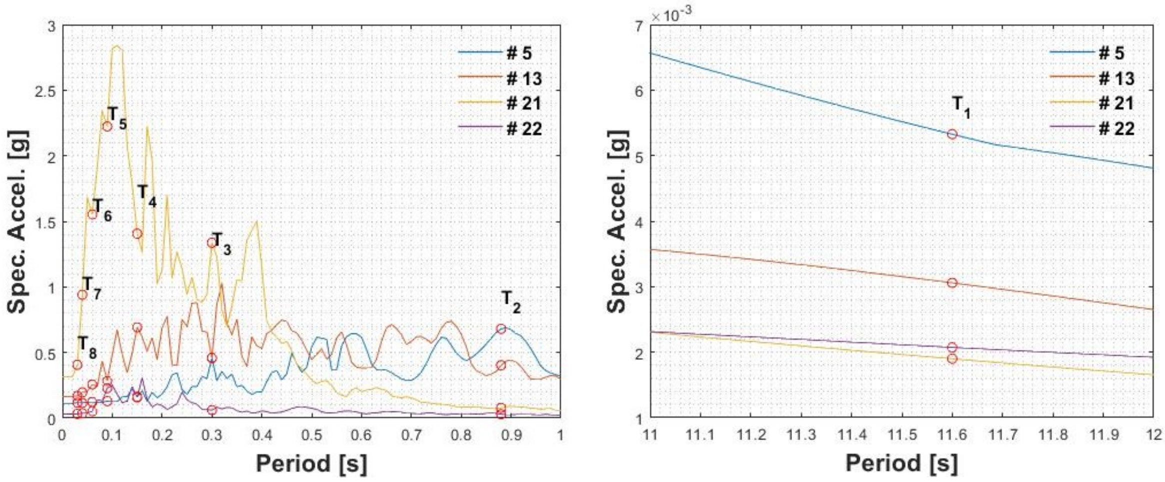

Figure 59: Spectral acceleration for each of the four identified ground motions at the first 8 periods.

However, the above-described phenomenon is observed only for some ground motions with a particular frequency content. By considering the entire set of ground motions, the mean value of IM, which causes the exceedance of the LS, as well as the corresponding dispersion, were slightly overestimated by Eq. (44), as presented in Table 24 for the fragility curves related to 90%, 80% and 70% filling level. The largest differences concern the dispersion β, which resulted in a higher value, in the order of 25%, in the Eurocode formulation (Eq. (44)). Minor differences are related to the median IM causing LS exceedance, denoted as μ. The μ values were observed lower in the IDA approach, in the order of 6%, 10% and 15%, respectively, for a filling level of 90%, 80% and 70%.

Table 24: The median IM causing the liquid overtopping μ and the corresponding dispersion β based on the simplified model and Eq. (44) formulation.

Filling level	**μ [g]**		**β [g]**	
	IDA	**Eq. (44)**	**IDA**	**Eq. (44)**
90%	0.14	0.15	0.43	0.53
80%	0.44	0.49	0.42	0.53
70%	0.81	0.95	0.42	0.54

5.6.2 Steel storage tank wall

Fragility functions were evaluated by means of the incremental dynamic analysis (IDA) (Vamvatsikos & Fragiadakis, 2010), with the set of ground motion presented in section 5.5. The ground motion IM selected was the spectral acceleration at the first impulsive period of the correspondent filling level (see Table 20), and the engineering demand parameter (EDP) was the compressive meridional stress. In this respect, the American code API 650 (American Petroleum Institute, 2012) provides a useful approach for the evaluation of such EDP with respect to of self-anchored tanks. In the code, a preliminary check is required in order to establish if the tank can be considered self-anchored. In Eq. (48) a so-called anchorage ratio (J) formulation, provided in API 650, is presented.

$$J = \frac{M_{rw}}{D^2\,[w_t(1-0.4A_v)+w_a-0.4w_{int}]} \tag{48}$$

where M_{rw} is the overturning moment of the steel storage tank provided by the aforementioned simplified model in the response history response analysis, D is the tank diameter in metres, w_t is the tank and roof weight per unit of circumferential length, A_v is the vertical earthquake acceleration in g, w_a the force uplifting in annular region and w_{int} the calculated design uplift load due to product pressure per unit of circumferential length. According to API 650 w_a can be calculated as in Eq. (49).

$$w_a = 99\;t_a\,\sqrt{F_y H G_e} \leq 201.1\;HDG_e \tag{49}$$

The t_a in Eq. (49) is the thickness of the bottom annulus under the shell in millimetres, F_y is steel yield strength in MPa, H is the maximum design product level in metres and G_e is the effective specific gravity ($G_e = G(1 - 0.4A_v)$ where G is the specific gravity). Finally, depending on the anchorage ratio, three different categories may be defined as in Table 25 provided in the code (American Petroleum Institute, 2012).

Table 25: Anchorage ratio criteria.

Anchorage ratio *J*	**Criteria**
$J \leq 0.785$	The tank is considered self-anchored. The calculation of uplift under the design seismic overturning moment is not required.
$0.785 < J \leq 1.54$	Tank is uplifting, but the tank is stable for the design load providing the shell compression requirements are satisfied. The tank is self-anchored.
$J > 1.54$	Tank is not stable and cannot be considered self-anchored for the design load. Modify the annular ring if $L < 0.035\ D$ is not controlling or add mechanical anchorage.

Where L is defined in Eq. (50) (American Petroleum Institute, 2012) in which each variable has the same meaning as the aforementioned ones.

$$L = 0.1723\ t_a \sqrt{F_y/(HG_e)} \tag{50}$$

Once the anchorage ratio was evaluated, the engineer demand parameter can be evaluated by Eq. (51) if $J < 0.785$ or Eq. (52) if $0.785 < J \leq 1.54$ (American Petroleum Institute, 2012). If J exceeds 1.54 the tank cannot be considered self-anchored. Hence anchorages are needed.

$$\sigma_c = \left[w_t(1 + 0.4A_v) + \frac{1.273 M_{rw}}{D^2}\right]\frac{1}{1000t_s} \tag{51}$$

$$\sigma_c = \left[\frac{w_t(1+A_v)+w_a}{0.607-0.18667\ J^{2.3}} - w_a\right]\frac{1}{1000t_s} \tag{52}$$

The t_s in Eqs. (51) – (52) is the thickness of bottom shell course in millimetres.

Concerning the investigated tank and the considered filling levels, being F_y = 345 MPa, the anchorage ratio values were always below 1.54 which represents the threshold to consider the steel storage tank self-anchored as prescribed by the API 650 and reported in Table 25 (American Petroleum Institute, 2012). In Figure 60 the maximum anchorage ratios are reported for each ground motion adopted in the IDA and filling level considered. All the investigated filling level can be considered self-anchored steel storage tanks because the greatest J never exceeded the maximum allowable value of 1.54. Moreover, in most of the cases, no base uplift was remarkable being J lower than 0.785.

IDA curves and fragility functions for tank wall buckling are presented in Figure 61 for a filling level of 90% ((a) and (b)), 80% ((c) and (d)) and 70% ((e) and (f)).

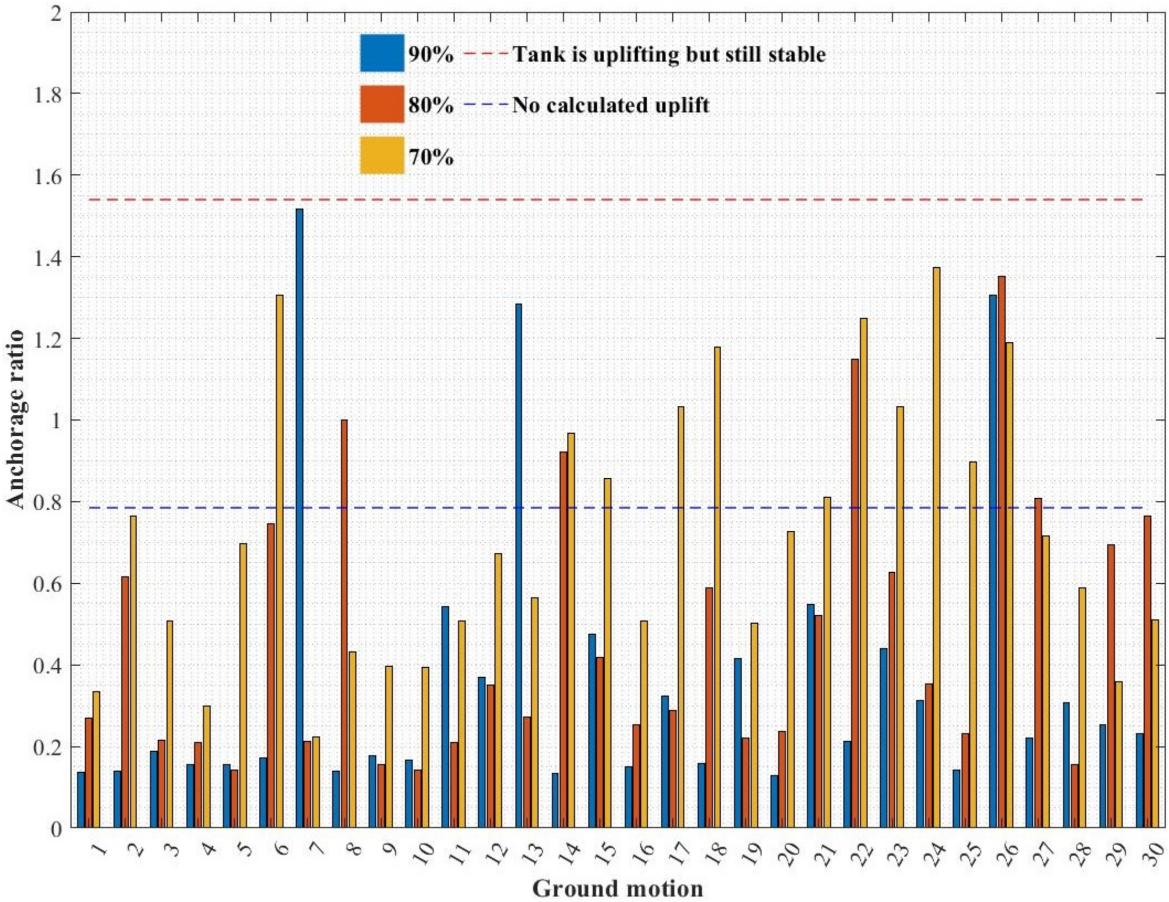

Figure 60: Maximum anchorage ratio provided by each adopted ground motion in the IDA.

Demand curves and fragility functions for tank wall buckling are presented in Figure 61 for a filling level of 90% ((a) and (b)), 80% ((c) and (d)) and 70% ((e) and (f)).

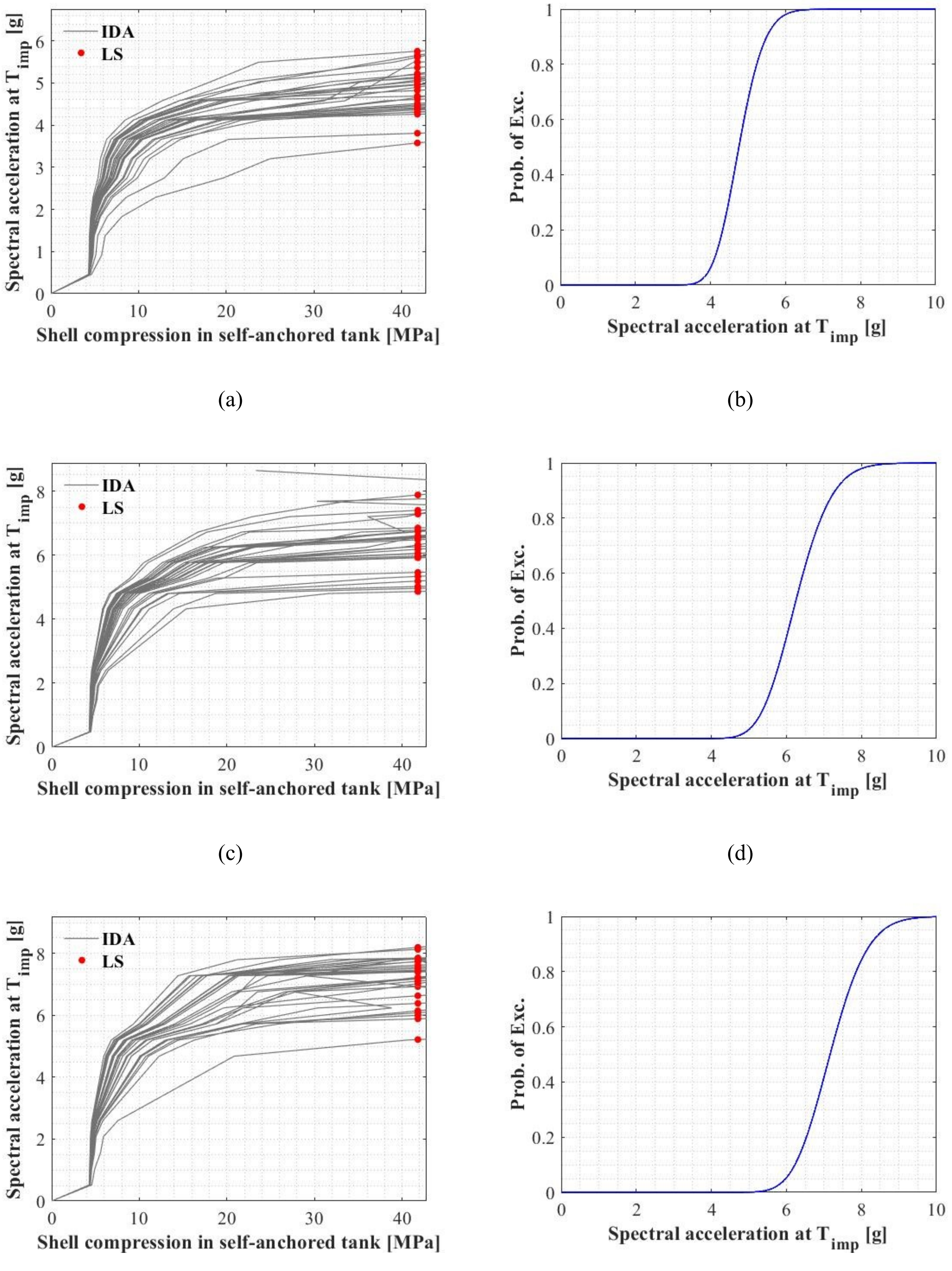

Figure 61: (a) IDA curves and (b) fragility curves for 90% of filling level, (c) IDA curves and (d) fragility curves for 80% of filling level, and (e) IDA curves and (f) fragility curves for 70% of filling level.

The median IM causing the tank wall buckling μ and the corresponding dispersion β for the considered filling levels with respect to maximum stress, which causes the exceedance of the selected LS for tank wall buckling are presented in Table 26.

Table 26: The median IM causing the tank wall buckling μ and the corresponding dispersion β based on the simplified model.

Filling level	μ [g]	β [g]
90%	4.76	0.11
80%	6.25	0.12
70%	7.16	0.11

5.7 Discussion

This Chapter dealt with the seismic vulnerability assessment of liquid overtopping in a storage tank equipped with a floating roof and elephant's foot buckling. For this purpose, simplified and refined FE models were first developed to simulate the response history of the floating roof and tank wall of the tank subjected to ground motion. The simplified model is computationally efficient, but is based several assumptions, which were, for the investigated tank, checked by a refined FE model.

The introduced simplified model has some advantages compared to the refined FE model if the objective is the simulation of the loss of containment due to the fluid overtopping. Firstly, the size of the simplified model, including the results of a single response history analysis, is of an order of megabytes, which is significantly less than that of the refined FE model (i.e. gigabytes). Moreover, the simplified model is computationally efficient and accurate for predicting maximum vertical displacement, which is the key engineering demand parameter for defining the overtopping limit state. Consequently, the simplified model is particularly suitable for fragility analysis because it is capable of providing vertical displacement response history of a liquid in a few minutes compared to hours of the refined FE model. Finally, the simplified model does not require specific licensed FEM software because it can be simply coded even in open-source software (i.e. Python (Van Rossum & Drake Jr, 1995)).

The simplified model adopted in the response history analyses of the tank wall buckling was developed based on the work of Malhotra (Malhotra et al., 2000). Moreover, the capabilities of tank base uplifting and base sliding were provided as suggested, for instance, in (Malhotra & Veletsos, 1994; Vathi & Karamanos, 2017; Phan & Paolacci, 2018), resulting in high computational efficiency, being particularly suitable in the seismic fragility assessment where hundreds of simulations are needed. However, further studies are required to bound the validity of that simplified model.

Particular attention was paid to the selection of ground motion records used in the vulnerability assessment of the vertical displacement of the floating roof, but the spectral acceleration at T=4 s was selected for the intensity measure for risk analysis because the probabilistic seismic hazard analysis is not carried out for spectral acceleration at longer periods, which is the consequence of the limitation of ground motion prediction models. Namely, the most suitable intensity measure for predicting the response of fluid and the floating roof is the spectral acceleration at the first convective motion period T_C, which values are usually in the order from 5 to 15 sec.

To further simplify the vulnerability assessment for liquid overtopping, an alternative approach for the fragility assessment based on the Eurocode formula for the estimation of the maximum free surface wave height was introduced. The alternative approach provided particularly good estimates of the maximum vertical displacement of the floating roof for the majority of ground motions. However, for the limited number of ground motions with a particular frequency content, the alternative approach overestimated the seismic demand because the Eurocode formula neglects the effect of the higher convective modes.

The potential for LOC in the wall of the investigated steel storage tank was observed significantly smaller than that referring to liquid overtopping. Indeed, by comparing the median IM, which causes the exceedance of the LS, the elephant's foot buckling occurs at higher spectral accelerations than the overtopping for each considered filling level with differences of about one order of magnitude. This outcome reflects the higher relevance of the LOC due to the fluid overtopping in the case of the investigated. Moreover, the IM adopted in the elephant's foot buckling vulnerability assessment displayed to be more efficient, producing lower dispersion than in the case of floating vertical roof displacement. Indeed, for each considered filling level, the dispersion for the loss of containment due to the elephant's foot buckling is in the order of 20% of the dispersion of the LOC due to overtopping by using the IDA procedure or 25% by using Eq. (44) (see Table 24 and Table 26).

6 SEISMIC PERFORMANCE ASSESSMENT OF STEEL STORAGE TANK WITH FLOATING ROOF

The steel storage tank equipped with floating roof, presented in Chapter 5, was assessed aiming to evaluate its seismic performance with respect to the content overtopping and tank wall failure due to buckling, which is reffered hereinafter as the loss of containment limit state (LOC LS). The seismic performance assessment comprises conventional performance metric and risk-based performance metric, introduced in Chapter 2 and briefly recalled in the following.

In this Chapter, the aforementioned performance metrics are used in the seismic assessment of the case study presented in Chapter 5 with respect of LOC due to excessive floating roof vertical displacement and to the tank's wall failure due to the buckling. Finally, a results discussion is provided summarizing the findings.

6.1 Conventional performance metric

In section 2.3.1, the conventional performance metric framework was presented, and its workflow described (see Figure 14). Following the same path, concerning the real steel storage tank presented in Chapter 5, its seismic performance was assessed against overtopping due to an excessive sloshing wave height and the tank wall failure due to buckling. In the case of the conventional performance metrics, the performance is considered acceptable when the ratio demand-to-capacity (D/C) is lower than one. Because seven ground motions are used, the demand can be evaluated as the average of the seismic response due to each ground motion (CEN, 2005).

6.1.1 Content overtopping limit state

The overtopping of the content was verified for ground-motion IM corresponding to a returning period of 2475. Based on the seismic hazard (see section 5.4), the corresponding spectral acceleration at T=4 seconds is 0.079 g. Considering all the limitations concerning the record selection and already described in section 5.4, seven ground motion were selected out of the entire set of Table 21 and, later on, scaled to match the target acceleration at T=4 s.

Three filling levels were considered: 90%, 80% and 70%. Capacities, in terms of the freeboard height, were the same as in fragility analysis, in particular, 1.2 m, 3.4 m and 5.6 m for 90%, 80% and 70% of filling level, respectively. Because seven ground motions were used, the seismic demand can be evaluated in the average. In Figure 62, the D/C ratios for the considered filling levels are presented. While the capacity was defined *a priori,* and it only changes as the filling level varies, the demand has been evaluated by means of two different approaches: the simplified model and the Eurocode formulation (Eq. (44)). In this respect the reader may refer to chapter 5. The outcomes of both approaches are presented in Figure 62 for all the aforementioned filling levels.

In Table 27, all the D/C ratios are expressed in terms of percentage to clarify better the seismic performance of the investigated steel storage tank equipped with a single deck floating roof.

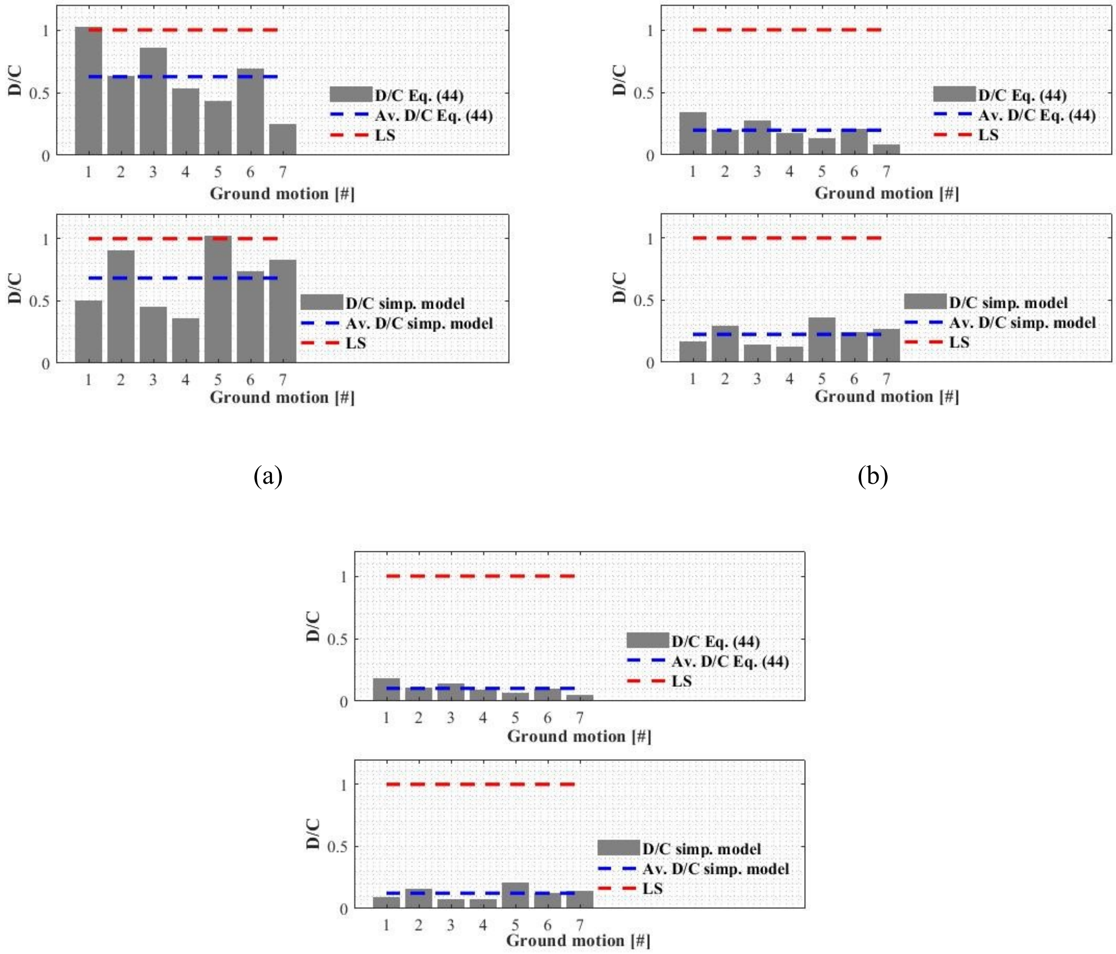

(a) (b)

(c)

Figure 62: Demand-to-capacity ratio for (a) 90%, (b) 80% and (c) 70% of filling level, evaluated by means of simplified model and Eq. (44) both for content overtopping.

Table 27: Overtopping average D/C ratios for the selected filling levels.

	D/C	
Filling level	**Eq. (44)**	**Simplified model**
90%	63%	68%
80%	20%	23%
70%	10%	12%

Based on the results of response history analyses, it was observed that the mean value of the demand-to-capacity ratio of the selected case study was smaller than one for all the considered filling levels. Moreover, the Eurocode formulation resulted in smaller D/C ratios compared to those provided by the simplified model as better comprehensible in Table 27. However, because of the reduced values of the D/C ratios, someone may conclude that the limit state requirements against content overtopping are satisfied and, even more, that the available freeboard may be overdesigned. This conclusion may be even considered true, but if the assessment process in concluded at this stage. Indeed, before taking a definitive opinion concerning the seismic vulnerability of the selected steel storage tank equipped with a single deck floating roof, deeper investigations may be helpful. In this respect, the need for conditional risk-based and risk-based decision models.

6.1.2 Tank wall failure due to buckling phenomenon

The LOC from the tank wall failure due to buckling was also verified for a ground motion corresponding to a return period of 2475 years. From the seismic site hazard curve, the corresponding spectral acceleration for the impulsive period was selected. More in detail, given the three considered filling levels, 90%, 80% and 70%, the spectral accelerations for 2475 years of returning period ($S_{a,2475}$) at impulsive period (T_i) of 0.40, 0.38 and 0.34 s are listed in Table 28, while in Figure 63 the hazard curves calculated for the impulsive periods with the corresponding spectral acceleration at 2475 years of returning period.

Table 28: Impulsive periods and corresponding spectral accelerations for the selected filling levels.

Filling level	$\boldsymbol{T_i}$ **[s]**	$\boldsymbol{S_{a,2475}(T_i)}$ **[g]**
90%	0.40	1.10
80%	0.38	1.14
70%	0.34	1.22

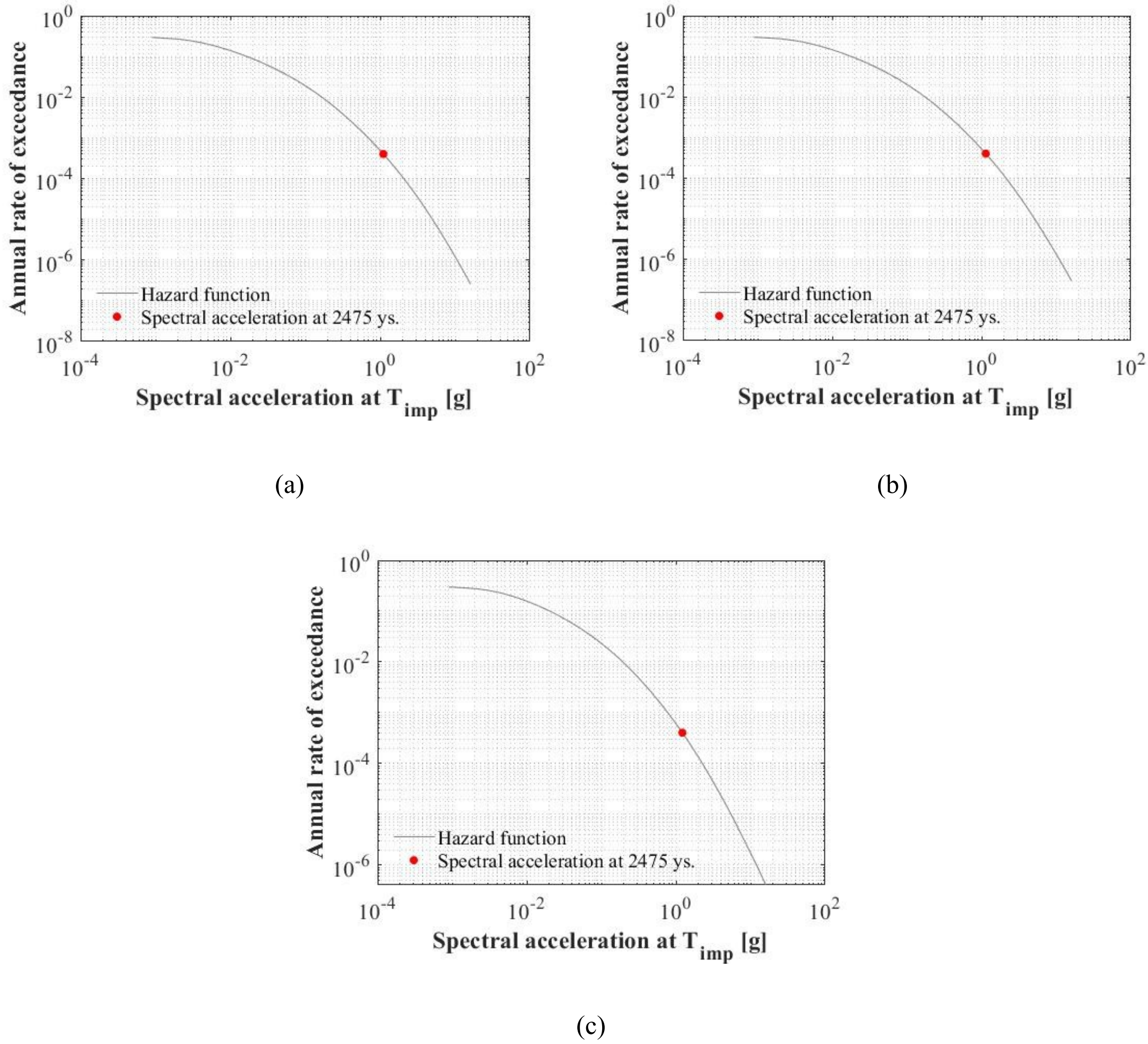

Figure 63: Seismic hazard curves for different impulsive periods related to (a) 90%, (b) 80% and (c) 70% of filling level.

Based on the record selection earlier described in section 5.5, seven ground motion were extracted out of the three selected set, one for each filling level, and, later on, scaled in order to match the target accelerations reported in Table 28.

The capacity of the tank wall was the same as in the case of fragility analysis, in particular, 41.8 N/m^2 for 90%, 80% and 70% of filling level (see in this respect Eqs. (47a) – (47b)). Seven ground motions were used. Thus the seismic demand was evaluated as the average demand based on the seven ground motions. In Figure 64, the D/C ratios for the considered filling levels are presented. While the capacity was defined by means of Eqs. (47a) – (47b) the demand has been evaluated by means of the simplified model presented in section 5.3.

In Table 29 the D/C ratios for each considered filling level. Because the D/C ratios are, in all the considered filling level, lower than 1, the seismic performance of the selected case study can be considered satisfactory.

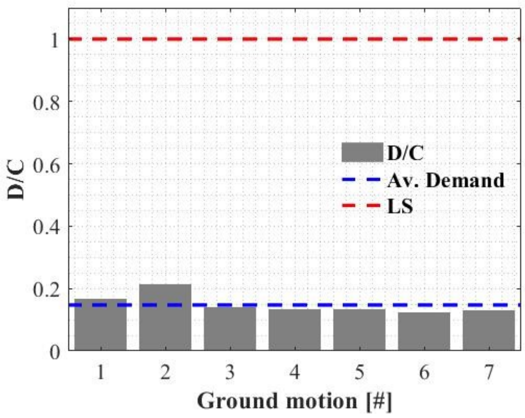

(a)

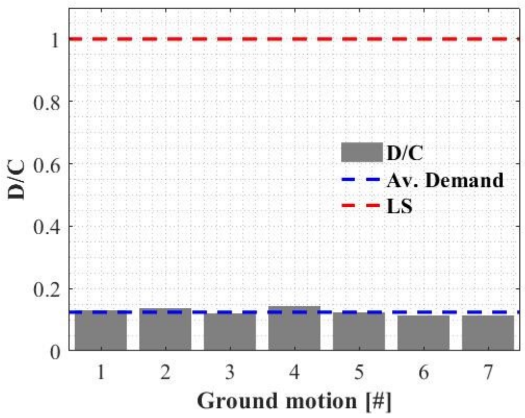

(b)

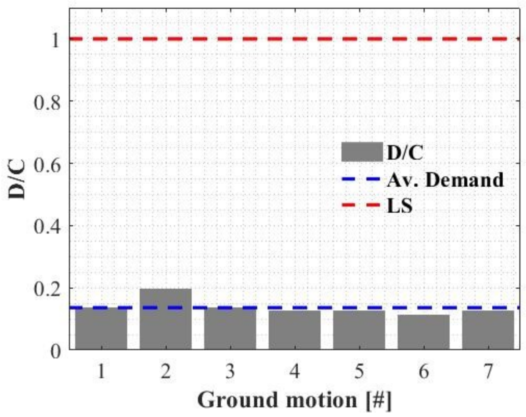

(c)

Figure 64: Demand-to-capacity ratio for (a) 90%, (b) 80% and (c) 70% of filling level, evaluated by means of the simplified model for tank wall failure due to buckling.

Table 29: Tank wall failure average D/C ratios for the selected filling levels.

Filling level	D/C
90%	15%
80%	13%
70%	14%

6.2 Risk-based performance metrics

In this section, two risk-based performance metrics will be investigated: the conditional risk-based decision model, which accounts for the probability of exceeding the designed LS at a certain level of seismic intensity and the risk-based decision model accounts for the probability of exceeding the LS for a fixed period of time. Both of them have been already introduced in section 2.3.1, while in Figure 14, the correspondent workflows are depicted.

6.2.1 Conditional risk-based decision model: the probability of exceedance of a limit state given the design level of seismic intensity

The conditional risk-based decision model is the first to be used and presented. Briefly resuming its step-by-step implementation, the user must first define the target spectrum, select the ground motions, and perform the seismic response history analyses. Up to this point, the performance metric is similar to the conventional one previously presented. From the seismic response history analyses, the user can compute the $P_{f,IM,LS,}$ which can be understood as the demand (similarly to the conventional performance metric). In order to do so, the user has simply to count the amount of ground motion that produced the exceedance of the LS, n_{LS}, and make the ratio with respect to the total amount of selected records, n_{GM}. Later on, by simply comparing $P_{f,IM,LS}$ with the allowable maximum probability corresponding to the selected LS, $P_{ft,IM,LS,}$ the user can make the risk-based decision.

6.2.1.1 Content overtopping limit state

The selection of ground motions has been performed as described in section 5.4. Twenty-two ground motions were selected and scaled to match the spectral acceleration at four seconds of 0.079 g, which corresponds to a return period of 2475 years. Even if, as already discussed in section 2.3, the more ground motions are used, the more accurate the outcome is, the difficulties encountered in ground motion selection did not allow to improve their amount. $P_{ft,IM,LS}$ has been set equal to 10%, following the same considerations as in section 2.3.

The same three filling levels were considered: 90%, 80% and 70% with the correspondent LS of 1.2 m, 3.4 m, and 5.6 m, respectively. In Figure 65, the seismic response analyses outcomes for the considered filling levels are presented. Even in this case, two different approaches were used to estimate the maximum content vertical displacement: the simplified model and the Eurocode formulation (Eq. (44)).

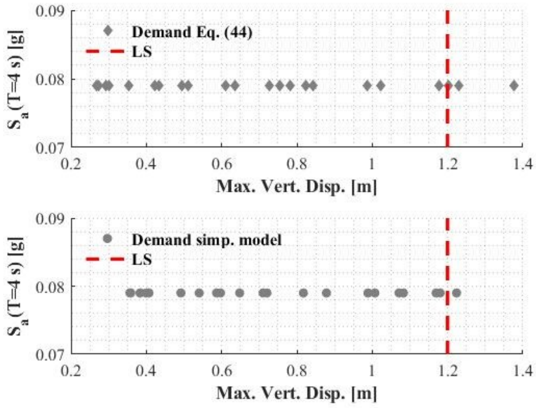

(a)

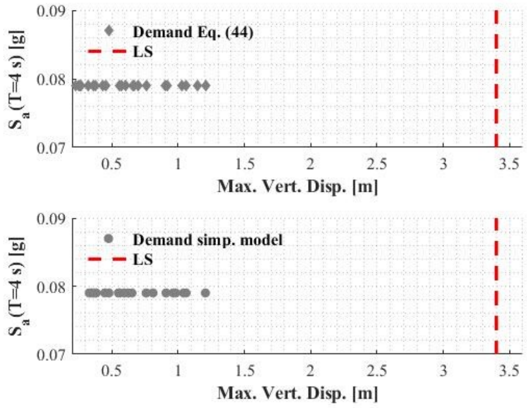

(b)

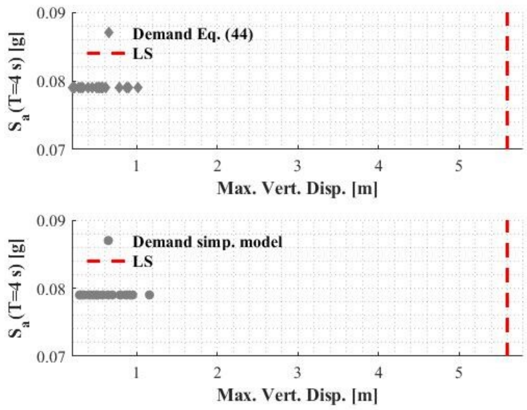

(c)

Figure 65: Single stripe analyses for (a) 90%, (b) 80% and (c) 70% of filling levels for content overtopping calculated using Eq. (44) and simplified model both.

The conditional risk-based decision model, which accounts for the probability of exceeding the LS for a given seismic intensity, displayed an opposite response to the conventional performance metric. Indeed, outcomes presented in Figure 65 and resumed in Table 30, presented an higher vulnerability, hence a non-satisfactory seismic performance ($P_{f,IM,LS}$=14%), if the EC 8-4 approach (Eq. (44)) was used, while the simplified model revealed a satisfactory performance ($P_{f,IM,LS}$=5%) for the 90% of filling level. The remaining considered filling levels did not produce the exceedance of the designed LS neither for Eq. (44) nor the simplified model. Moreover, larger demand dispersion is observable in the EC 8-4 approach as discussed in section 5.6.1 which can be seen in Figure 65 (a), (b) and (c). Moreover, it is worth mentioning that if the ground motions were scaled at T_c the use of EC 8-4 formulation would not have produced any dispersion. However, as earlier mentioned, such normalization is not possible due to the lack of ground motion prediction equations developed for such long periods (e.g. T_c was 11.6 s for the maximum filling level).

Table 30: Probability of exceedance of near-collapse LS for content overtopping for the S_a at 4 s corresponding to a returning period of 2475 years.

	$P_{f,IM,LS}$ [%]	
Filling level	**Eq. (44)**	**Simplified model**
90%	14%	5%
80%	-	-
70%	-	-

6.2.1.2 Tank wall failure due to buckling phenomenon

Ground motions were selected as discussed in section 5.5, and thirty records were firstly extracted from the database. Later on, each ground motion was scaled in order to match the spectral acceleration at 2475 years of returning period for each of the selected filling levels (see Table 28).

$P_{ft,IM,LS}$ as discussed in section 2.3.1, has been set equal to 10%. The same three filling levels were considered: 90%, 80% and 70% with the correspondent LS capacity of 41.8 N/m^2. In Figure 66 the seismic response analyses outcomes for the considered filling levels are presented. Seismic demand was calculated by means of the simplified model presented in section 5.3.

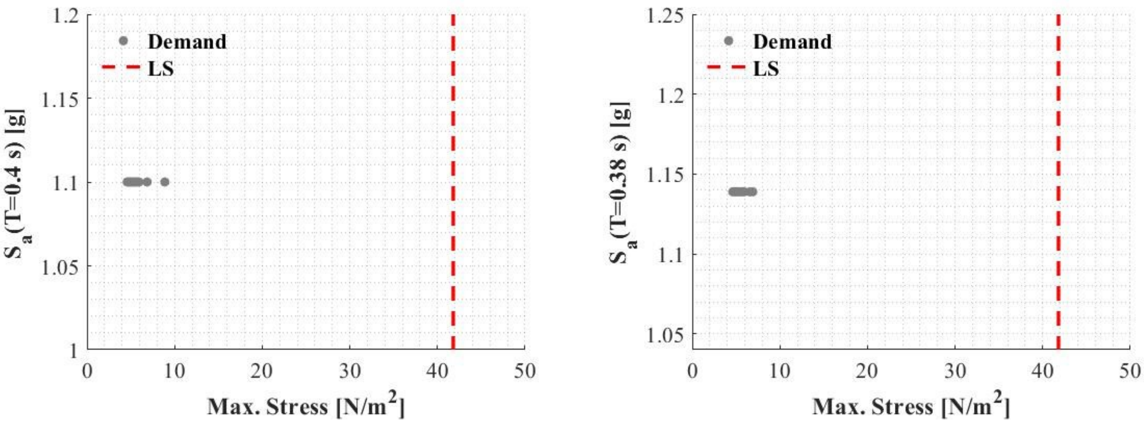

(a) (b)

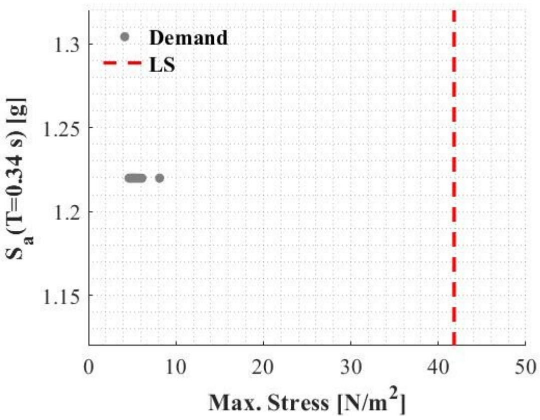

(c)
Figure 66: Single stripe analyses for (a) 90%, (b) 80% and (c) 70% of filling levels for tank wall failure calculated using the simplified model.

The conditional risk-based performance metric, which accounts for the probability of exceedance, the LS for a given seismic intensity provided a satisfactory seismic performance for all the considered filling level, in agreement with what concluded in section 6.1.2 (see Table 29). Moreover, none of the selected ground motion used in the seismic time-history analyses produced demand exceeding the selected LS.

6.2.2 Risk-based decision model: the probability of exceedance of LS for a given period

The second performance metric used was the risk-based decision model accounts for all possible earthquakes that can occur in a given period of time. In this respect, the decision model can account for the probability of exceedance of the designed LS for a given period of time ($P_{f,LS}$).

In the step-by-step procedure for the decision model (see section 2.3.1), the user first defines the site seismic hazard, selects the ground motion, performs the response history analyses, and evaluate the fragility function and, later on, the $P_{f,LS}$. Finally, the decision-making process can be concluded by comparing the $P_{f,LS}$ with the acceptable (target) probability of exceedance the selected LS, $P_{ft,LS}$ resulting in satisfactory performance if $P_{f,LS} < P_{ft,LS}$ *vice versa* not. The $P_{ft,LS}$ has been set equal to $2 \cdot 10^{-4}$, following the same consideration of section 2.3.1.

However, the filling level of a steel storage tank may vary during the lifetime according to the industrial needs being the latter not constantly at 90%. Consequently, this parameter may have a particular influence on the overtopping risk assessment. In this respect, the probabilities of occurrence of this phenomenon were evaluated for the several considered filling levels and combined by using the total probability theorem, assuming the events as being mutually exclusive (Kokoska & Zwillinger, 2000).

The total probability of occurrence of the overtopping event B, $P[B]$, given the annual probabilities of having the filling level (A_i) $P[A_i] \neq 0$ with $i = 1,2,\dots,n$, reads

$$P[B] = \sum_{i=1}^{n} P[B \mid A_i, IM = im] \times P[A_i] \tag{53}$$

where $P[B|A_i, IM = im]$ in Eq. (53) is the probability of exceeding the designated limit state B for the *i-th* filling level A_i, and the seismic intensity $IM = im$, which is the fragility function.

The probability of exceedance the designed LS for a given period of time ($P_{f,LS}$), which means the risk of overtopping or tank wall failure, is then obtained by coupling the seismic fragility and risk function:

$$P_{f,LS} = \int_0^{\infty} P[B|IM = im] \left|\frac{dH(im)}{d(im)}\right| d(im) \tag{54}$$

where $P_{f,LS}$ is the annual rate of exceeding the LS, im is the ground motion intensity, and $H(im)$ is the seismic hazard function that expresses the annual rate of exceedance of im.

In this respect, substituting right-hand side of Eq. (53) in Eq. (54), the latter becomes:

$$P_{f,LS} = \int_0^{\infty} \sum_{i=1}^{n} P[B \,|A_i, IM = im] \times P[A_i] \left|\frac{dH(im)}{d(im)}\right| d(im) \tag{55}$$

Because $P[A_i]$ does not depend on IM, the risk equation can be further simplified:

$$P_{f,LS} = \sum_{i=1}^{n} P[A_i] \int_0^{\infty} P[B \mid A_i, IM = im] \left|\frac{dH(im)}{d(im)}\right| d(im) \tag{56}$$

The previous equation represents the conventional risk equation with the exception to have combined the risk of the single filling levels. The integrals of Eq. (56) can be conveniently considered as weights of the probability of occurrence of the filling levels A_i and Eq. (56) re-written as

$$P_{f,LS} = \sum_{i=1}^{n} P[A_i] \, P_{fi,LS} \tag{57}$$

where P_{fi} represents the annual rate of exceeding the LS of *i-th* considered filling level A_i, as in Eq. (58):

$$P_{fi,LS} = \int_0^{\infty} P[B \mid A_i, IM = im] \left|\frac{dH(im)}{d(im)}\right| d(im). \tag{58}$$

Because of the scarcity of available data describing the time-dependent variation of the filling level during one year, a discrete probability mass function was assumed, Table 31, mainly focusing, deliberately, on steel storage tanks with a large amount of content and then with the increased probabilities of high filling levels.

Table 31 Probability mass function for discrete probability distribution per year.

Filling level [%]	90	80	70	60	50	40	30	20
$\boldsymbol{P[A_i]}$ **[%]**	70	12	4	4	3	3	2	2

Based on the theoretical background for risk estimation, the fragility analysis should be performed for many different filling levels. However, in the present work, the fragility analysis was performed only for 90%, 80% and 70% filling levels. The reason for this choice, as already presented in Chapter 5, relies on several aspects, herein briefly recalled, mainly related to the content overtopping, which displayed to be the most relevant source of LOC:

- lowering the filling level corresponds to a linear increase of the available height for attaining overtopping, which means that the risk for overtopping is automatically reduced because of that;
- the lower the filling level is (lower γ), the higher T_c (e.g. at 20% of filling level, T_c is 23 s) is, hence relevant difficulties in the ground motion selection;
- low filling levels were assumed to be less probable than higher ones, which results in a negligible influence on risk (Eq. (57)).

In Table 32, the mean and the dispersion resulted from the fragility analyses of section 5.6.1 and the $P_{fi,LS}$ for the *i-th* filling levels with respect of content overtopping due to convective motion. Moreover, the probability of exceedance, the LS is given for a period of 50 years ($P_{fi,LS,50}$). In Table 33, the same but with respect to tank wall failure due to buckling.

Table 32: Median spectral acceleration causing overtopping and the corresponding dispersion from fragility analysis and probability of exceedance of LS for one year and 50 years.

Filling level	μ **[g]**		β **[g]**		$P_{fi,LS}$		$P_{fi,LS,50}$	
	IDA	**Eq.(44)**	**IDA**	**Eq.(44)**	**IDA**	**Eq.(44)**	**IDA**	**Eq.(44)**
90%	0.14	0.15	0.43	0.53	$2{\cdot}10^{-4}$	$1.9{\cdot}10^{-4}$	1%	0.9%
80%	0.44	0.49	0.42	0.53	$2.6{\cdot}10^{-5}$	$2.5{\cdot}10^{-5}$	0.1%	0.1%
70%	0.81	0.95	0.42	0.54	$6.9{\cdot}10^{-6}$	$6.2{\cdot}10^{-6}$	0.03%	0.03%

Table 33: Median spectral acceleration causing tank wall failure and the corresponding dispersion from fragility analysis and probability of exceedance of LS for one and 50 years.

Filling level	μ [g]	β [g]	$P_{fi,LS}$	$P_{fi,LS,50}$
90%	4.76	0.11	$1.2\cdot10^{-5}$	0.06%
80%	6.25	0.12	$5.9\cdot10^{-6}$	0.03%
70%	7.16	0.11	$4.8\cdot10^{-6}$	0.02%

The annual frequency of occurrence of LS (Table 32) appears to be almost insensitive to the procedure adopted (IDA or Eq. (44)) for all the considered filling levels, with differences of the order of 5%, 4% and 11% for the filling level of 90%, 80% and 70% respectively. This insensitivity is mainly due to the antithetic influence of β and μ on the risk, in the sense that a large β produces a higher risk, and a higher μ reduces the risk. Moreover, the mean annual frequency of occurrence of tank wall failure due to buckling resulted in very low values with high median accelerations which can cause the exceedance of the selected LS (Table 33).

Seismic performances may be considered acceptable for all the filling levels disregarding the adopted approach, either concerning the content overtopping or the tank wall failure, because risk values ($P_{f,LS}$) are lower than the target one ($P_{ft,LS}$). However, quite relevant $P_{f,LS}$ was observed for the 90% of filling level considering the content overtopping (Table 32). Indeed, both analysis approaches provided $P_{f,LS}$ values very close to the maximum allowable probability of failure ($P_{ft,LS}$) of 2·10-4.

Accounting for the probabilities of having different filling levels (Eq. (57)), probabilities of failure can be recalculated for both of the LOC sources and presented in Table 34.

Table 34: Probability of exceedance of LS given a period of time in the case of content overtopping and tank wall failure.

Probability of failure	**Content overtopping**		**Tank wall failure**
	IDA	**Eq. (44)**	
$P_{f,LS}$	$1.43\cdot10^{-4}$	$1.36\cdot10^{-4}$	$9.3\cdot10^{-6}$
$P_{f,LS,50}$	0.71%	0.68%	0.05%

Concerning the content overtopping the differences between the two adopted approaches become almost negligible. In particular, $P_{f,LS}$ equals $1.43\cdot10^{-4}$ and $1.36\cdot10^{-4}$ when the IDA approach and Eq. (44) are used, which correspond to $P_{f,LS,50}$ equals to 0.71% and 0.68% respectively, as presented in Table 34. However, the value of risk decreases by approximately 20% - 30% if only the maximum filling level condition was considered with respect to the tank wall failure and content overtopping respectively.

6.3 Discussion

Chapter 6 dealt with the seismic performance assessment of a real steel storage tank equipped with a floating roof, emphasising the loss of content due to the overtopping induced by excessive sloshing and tank wall failure due to the buckling. The conventional performance metric was extremely user-friendly because the reduced amount of simulations, however, may be not so exhaustive. By focusing on the content overtopping, according to the findings presented in Figure 62 and Table 27, one may conclude that the freeboard is overdesigned because of the low D/C ratio, even if some differences between the two adopted approach are evident (in particular, the simplified model provided slightly greater D/C if compared to those provided by Eurocode formulation). Moreover, the totally negligible influence of lower filling levels than 90% was demonstrated. The tank wall failure was observed as very unlikely because of the extremely low D/C ratio, even in the maximum filling level.

The conditional risk-based decision model that accounts for the probability of exceedance of a limit state given the design level of seismic intensity regarding the overtopping displayed opposite performances with respect to the conventional performance metric. Firstly, the Eurocode formulation provides greater seismic demands than the simplified model (see Figure 65 and Table 30), which is the opposite case of the conventional performance metric. In this respect, it is worthy of highlighting the non-satisfactory seismic performance of the 90% filling level if the Eurocode approach was used, which is in full disagreement with the simplified model results. Lower filling levels displayed satisfactory performance for both considered approaches with no exceedance of designated LS. In the tank wall failure case, none of the response history analyses exceeded the LS (Figure 66).

In the case of content overtopping, the risk-based decision model which accounts for the probability of exceedance of LS for a given period, was in agreement with the conventional performance metric regarding worst seismic performances provided by the simplified model compared to those of the Eurocode formulation (see Table 34) for all the considered filling levels. It was found that the risk ($P_{f,LS,50}$) for overtopping in the case of a 90% filled tank is approximately 1% in 50 years for both of the considered approaches, which may not be tolerable for all stakeholders exposed to that risk even if slightly lower than the maximum allowable value. Different the case of LOC due to the tank wall failure which probabilities of failure are lower than 1% in 50 years of one order of magnitude in the case of 90% of filling level. By considering the risk-based performance metrics, even if some peculiarities are relevant, both of them disproved the assumed overdesigned freeboard as suggested by the conventional performance metric in the case of overtopping. All three decision models proved the steel storage tank to have satisfactory performances concerning the tank wall failure due to the buckling.

Finally, because the tank is not full all of the time, it was shown that risk could be overestimated by disregarding the variation of filling level during the year. In particular, a risk reduction in the order of 30% and 20% was observed for the overtopping and tank wall failure, respectively. Tank wall satisfactory seismic performance is not surprising concerning the present case study. Indeed, it is worth highlighting how the EDP is affected by tank diameter and bottom course shell thickness (extremely large in both cases, 86 m and 43 mm respectively) as presented in Eqs. (51) – (52), in which the larger diameter and tank wall thickness are, the lower is the vertical stresses acting on the tank wall itself. Moreover, the anchorage ratio (*J*) in the most part of the response history analyses resulted lower than 0.785 (Figure 60), indicating the scarce presence of uplifting hence of buckling phenomena on the tank wall.

The risk reduction resulting from the variation of the filling level in the reference period, may represent a crucial aspect in the risk mitigation by simply adopting, as a risk reduction strategy, the limitation of the filling level, if possible. Based on the results obtained by accounting for the probability of having different filling levels, the seismic performance of the selected case study can be considered satisfactory regardless of the adopted approach, performance metric and the selected LS.

7 CONCLUSIONS

In Chapter 2, the seismic performance assessment of the code-non-conforming and code-conforming elevated steel storage tanks was performed by using simplified models and three performance metrics. At that stage of the research, the presence of the roof was neglected because the main objective was to evaluate the available performance metrics. By considering Kocaeli ground motion for the seismic response history analysis of the non-code-conforming, the simplified nonlinear model provided the same observations as observed during the Kocaeli earthquake in the case of almost full and almost empty tank configuration. Namely, the almost full non-code-conforming tank collapse while the almost empty tank was undamaged. Such observation provided some trusts in the simplified nonlinear models of the investigated elevated tanks, which were then assessed by the three performance metrics. It was shown that regardless of the considered performance metric, the seismic performance of the investigated non-code-conforming elevated tank is not acceptable. The opposite was observed for the code conforming elevated tanks, with one exception. In the case of the full tank and the conditional risk-based performance metric, the seismic performance assessment of the code-conforming tank was not acceptable. Such an outcome may be a consequence of the calculation of the probability of exceedance of the LS by considering the limited number of ground motions. If the probability of exceedance of LS given the design level of ground-motion intensity was obtained from the fragility function, then the performance of the code-conforming tank was satisfactory even with respect to the conditional risk-based performance metric.

The above-described observations were not surprising. However, suppose only the conventional performance metric is used. In that case, one may conclude that the elevated tank's supporting structure was overdesigned because the demand-to-capacity ratio was significantly less than one, which is the maximum allowable value. Indeed, risk-based decision model results provided a probability of failure slightly less than the target one. Thus, the conventional performance metric appeared to be not well calibrated in this case. The preliminary research outcome, presented in Chapter 2, revealed that the design could be significantly affected by the performance metrics used to decide on the satisfactory design. Risk-based performance metrics are more general, but it requires numerous simulation of the structure's seismic response.

Nevertheless, it could be concluded that the risk-based performance metrics should be used at least in the next generation of the standards regardless of the computational effort. A reasonable alternative to the risk-based performance metrics presented would be the so-called 3R method introduced by Dolšek et al. in (Dolšek & Brozovič, 2016), which allows risk-based decision utilizing only single-stripe analysis. However, it requires to assume the dispersion of the ground-motion intensity, which is not a critical assumption if the ground-motion intensity for stripe analysis refers to a low percentile of the target fragility function, as discussed by Dolšek & Brozovič (2016). Finally, it is worth mentioning that the results presented in Chapter 2 were based on several assumptions (e.g. LS definition, target performances and modelling choices).

Because numerous seismic response history analyses are needed in the risk-based seismic performance assessment, and the Thesis addresses storage tanks with floating roofs, Chapter 3 focuses on a mathematical background of the simplified model, which is capable of simulating, the vertical displacement response history of a floating roof under seismic loading. The simplified model is based on Hamilton's variational principle, and it requires the definition of several input data that have to be carefully selected. The simplified modal was coded in Matlab environment, being, in this way, easily suitable for the seismic performance assessment analyses. However, before its usage in the performance assessment, it was validated by means of experimental data and numerical outcomes of a refined FE model.

Along these lines, the first part of Chapter 4 briefly introduces a shaking table test performed on a scaled steel storage tank equipped with a floating roof. This test provided useful experimental data about the vertical displacement histories of floating roofs subject to seismic loading. Subsequently, a simplified model and a refined finite element model aimed at simulating the shaking table test program were developed. Relevant experimental and numerical outcomes were then presented and discussed. Finally, a parametric study related to the simplified model was performed to highlight the most relevant parameters involved. It was shown that both the refined finite element model and the simplified model were capable of simulating the roof vertical displacement histories observed in the shaking table test. The former model has higher fidelity but appears to be excessively time-consuming, whilst the latter is more suitable for risk assessment purposes. Furthermore, in the parametric study concerning the parameters involved in the simplified model, it was realized that the greatest influence on the maximum vertical floating roof displacement has the ratio between the fluid height and the tank radius. Moreover, it appeared that roof's Young's modulus did not significantly affect the vertical displacement, while the only tangible influence was observed in a large response variation, mainly in the free vibration range. The other investigated parameters, the fluid density and the floating roof material density, did not affect the overall response. Furthermore, it was found that the Eurocode's formula for the maximum vertical displacement of free-surface fluid was sufficiently accurate in the prediction of the peak vertical displacement of the floating roof of the investigated tank, as discussed in Chapter 5.

In Chapter 5, the seismic fragility assessment of a real steel storage tank equipped with a single deck floating roof was performed. The seismic fragility analysis focused on the loss of content due to overtopping and the tank wall failure due to buckling. Concerning the first one, fragility analyses were conducted using two different approaches: the closed-form equation for the maximum vertical displacement of free-surface fluid provided by Eurocode 8 and the simplified model coded in Matlab. Both approaches produced similar results, revealing a quite relevant seismic fragility of the investigated tank. The Eurocode formulation provided a higher mean value of IM. Consequently, the exceedance of the loss of containment LS in comparison to that based on the simplified model was underestimated by 7%, 11% and 17%, respectively, for filling levels of 90%, 80% and, 70%, even though the corresponding dispersion was greater in the order of 20% regardless of the filling level. Furthermore, the Eurocode approach revealed to be particularly sensitive to some ground motions frequency content. For some specific ground motion characterized by particular frequencies, the maximum vertical fluid displacement was underestimated by Eurocode formula, which resulted in larger scaling factors to reach the exceedance of the LS. This happened because Eurocode's closed-form solution only accounts for the first convective mode to calculate the displacement. Usually, this assumption ensures a reasonable accuracy, as demonstrated for most of the selected ground motions. However, in some cases where higher modes are relevant, differences appear. However, besides these particular cases, the Eurocode formulation appeared to be quite suitable for the investigated liquid storage tank's fragility analysis. Fragility analyses of the tank wall were conducted using a simplified stick model including the capability of simulating the base uplifting and sliding, and they revealed a negligible vulnerability with respect to tank wall failure due to buckling phenomena thanks to the broadness of the steel storage tank and the elevated thickness of the bottom courses (in the order of 4 cm) which ensures safety against buckling.

In Chapter 6, the performance metrics presented in Chapter 2 were applied to assess the seismic performance of the liquid storage tank introduced in Chapter 5. In this case, the loss of containment with respect to content overtopping and tank wall failures were also investigated. The conventional performance metric revealed the lower seismic performances of the investigated case study in the case of content overtopping rather than tank wall failure. However, the tank's performance against loss of containment was observed acceptable. Even in the case of maximum filling level, the D/C ratio was lower than one. In particular, the floating roof assessment provided maximum D/C ratios of 68% and 63%, respectively, if the simplified model and the Eurocode formula was used. The maximum D/C ratio concerning the tank wall failure was way far from the maximum allowable 15%.

The second performance metric adopted in the assessment of the selected case study was the conditional risk-based metrics. Even in this case, for the content overtopping, both the Eurocode formulation and the simplified model were used. Also, this performance metric revealed that the overtopping of content is the most probable, as remarked by the conventional performance metric, but, on the contrary, it appeared that the performance against overtopping is not acceptable if the Eurocode formula was used. Indeed, the probability of overtopping calculated using the Eurocode formula was 14% which is greater than the maximum allowable set to 10%. However, if the simplified model was used instead of the Eurocode formulation, the probability of experience an overtopping was 5% maximum. It can be concluded that even if the first convective mode is the most relevant, neglecting the higher ones may lead to an underestimation of the response, as in the case of the Eurocode formulation. No probability of exceedance of the LS was observed in the case of the tank wall.

Finally, the third performance metric used was the risk-based metrics. The probability of failure for the content overtopping in the case of the maximum filling level was almost 1% in 50 years for both models adopted (Eurocode formula and simplified model). In the tank wall failure case, this probability decreased up to 0.06% in 50 years for the same content level. According to the adopted performance metric and the observed results, the investigated case study's seismic performances cannot be considered acceptable with respect to the content overtopping for all stakeholders exposed to that risk. Vice versa it can be concluded for the tank wall. However, in this performance metric, the variation of the filling level among one year of the lifetime of the storage tank was also taken into account. In this respect, an approach that can be seen as a risk-mitigation strategy is represented by the consideration of the probability of having different filling levels, being unrealistic assuming to have always the maximum capacity stored. In this respect, the probability of failure decreased from 1% in 50 years up to 0.7% in the case of overtopping being, in this way, a satisfactory performance. The introduced methodology for seismic risk assessment, if applied for the determination of the risk-based tolerable tank's filling level of the storage tanks, is an efficient tool for loss-of-containment risk management.

8 RAZŠIRJENI POVZETEK

V tem poglavju je predstavljen povzetek celotne doktorske disertacije v slovenskem jeziku. Vsako podpoglavje povzetka je skladno s poglavjem doktorske disertacije. S tem želimo, da bralec dobi čim boljši vpogled v celotno disertacijo. Naslovi posameznih podpoglavji povzetka so zato usklajeni z naslovi poglavji doktorske disertacije.

8.1 Uvod

Industrijski objekti so izjemno pomembni z vidika zagotavljanja funkcionalnosti grajenega okolja in socialne blaginje, vendar so nekateri nedavni potresi, cunamiji in poplave sprožili naravno-tehnološke dogodke (angl. *Natech events*), ki poudarjajo ranljivost industrijskih objektov (Lanzano et al., 2015). Poleg tega sta večja skrb za okolje in negotovosti, povezane s prihodnjimi gospodarskimi izgubami, privedla do potrebe po izboljšanju znanja o varnosti kompleksnih industrijskih sistemov. Krepi se tudi zavedanje, da je treba posebno pozornost posvetiti redkim dogodkom, na primer močnejšim potresom, za katere deležniki ne morejo razviti dojemanja tveganja na podlagi izkušenj. Problem se lahko reši z razvojem ustreznih postopkov in metod za nepristransko oceno tveganja in odpornosti.

Industrijski objekti in jekleni rezervoarji, ki vsebujejo okolju in človeku nevarne snovi, so bili med potresi večkrat močno poškodovani (Lindell & Perry, 1996; Young et al., 2004). Natech nesreče, ki so posledica potresnih dogodkov, pa lahko sprožijo še dodatne nezažele ne pojave, kot so eksplozijski valovi, strupene emisije, požar, sevanje, razlitje nevarne vsebine ali puščanje. Zato je bilo potresno obnašanje industrijskih obratov v zadnjem času predmet številnih raziskav (Kalemi et al., 2019; Karagiannakis et al., 2020; Celano 2020; Celano & Dolšek, 2021). Boljše poznavanje potresnega odziva industrijskih obratov namreč prispeva k natančnejši in enostavnejši oceni tveganja, ki je bistvenega pomena za ozaveščeno odločanje (Antonioni et al., 2007), saj rezervoarji za hranjenje tekočin zagotovo niso imuni na naravno-tehnološke nesreče. V izogib okoljskim katastrofam, telesnim poškodbam in za zagotovitev ustrezne stopnje odpornosti grajenega okolja, je treba uhajanje nevarnih vsebin rezervoarjev za hranjenje tekočin preprečiti na osnovi toleriranega tveganja, s katerim se zagotavlja ustrezno odpornost sistema, podjetja in družbe.

Najbolj pogoste poškodbe jeklenih rezervoarjev se pojavijo na stenah rezervoarja (tj. pojav plastičnega uklona v obliki »slonove noge« ali diamantna oblika uklona), sidriščih, podpornih konstrukcijah in plavajočih strehah (Hatayama et al., 2004), ki so še posebej ranljive. Obnašanje rezervoarjev je bilo raziskano s številnimi različnimi modeli (Malhotra & Veletsos, 1994; Malhotra, 1995; Malhotra et al., 2000; Bakalis et al., 2017). Le nekaj študij je obravnavalo potresni odziv strehe rezervoarja, pri čemer je šlo pretežno za pritrjene strehe (Fan et al., 2018; Kummari et al., 2018; Taniguchi et al., 2018). V večini dejanskih primerov streha ni pritrjena na rezervoar, zaradi česar pride med močnim gibanjem tal do interakcije med prosto površino tekočine in spodnjo površino plavajoče strehe. Pojavi se vertikalni pomik tekočine, ki ni enakomerno porazdeljen po celotni površini strehe. Pride lahko tudi do plastifikacije strehe ali do velikega relativnega premika med robom strehe in steno rezervoarja. Glavni vzrok za uhajanje tekočine iz rezervoarja je verjetno prenehanje tesnjenja plavajoče strehe (Shabani & Golzar, 2012). Interakcija med streho, steno rezervoarja in tekočino med potresno obtežbo še ni dovolj dobro raziskan problem (Matsui, 2007; Matsui, 2017), zato je za kvantificiranje te interakcije potrebno razviti ustrezna orodja. Dandanes je z uporabo metode končnih elementov omogočena detajlna analiza konstrukcij, vendar je tak pristop za analizo gradbenih konstrukcij računsko zelo zahteven (Fabbrocino et al., 2005). Zahtevnost analize se v primeru rezervoarjev za tekočine dodatno poveča, v kolikor se takšne simulacije uporablja za celoten terminal rezervoarjev naftne rafinerije. Simulacije potresnega odziva jeklenih rezervoarjev pa so še bolj zapletene v primeru ocene tveganja, ki zahteva na stotine simulacij za različne stopnje potresnih vplivov (Corritore et al., 2017). Zaradi navedenih dejstev je treba razviti poenostavljene modele rezervoarjev za hranjenje tekočine, s katerimi bi omogočili enostavno in hitro oceno potresnega tveganja.

Poleg ustreznih modelov za potresno analizo objektov, je treba za dobro ozaveščen postopek odločanja uporabiti primerne mere za ovrednotenje potresne zmogljivosti objektov in razviti ustrezne odločitvene modele. Konvencionalni kazalniki potresne zmogljivosti objekta temeljijo zgolj na inženirskih parametrih potresnih zahtev, ki so določeni z upoštevanjem izbranega potresnega scenarija (CEN, 2004). Posledice vseh drugih možnih potresov, ki se lahko pojavijo na lokaciji konstrukcije tekom njene življenjske dobe, so torej pri projektiranju eksplicitno ne preverja. Na primer, Vathi et al., (2017) so s konvencionalnimi pristopom ocenili potresno zmogljivost rezervoarjev za hranjenje tekočine. Podoben pristop za oceno objektov po potresu v Izmitu sta uporabila (Sezen & Whittaker, 2006). V splošnem pa so za oceno potresne varnosti bolj primerni odločitveni modeli, ki temeljijo na analizi tveganja. Ena od možnosti je, da se ciljno zmogljivost objekta opredeli s sprejemljivo verjetnostjo prekoračitve določenega mejnega stanja (angl. *limit state*, *LS*) pri pogoju izbranega potresnega scenarija. Še bolj splošno pa je, če se ciljno zmogljivost objekta opredeli s sprejemljivo verjetnostjo prekoračitve določenega mejnega stanja v izbranem časovnem obdobju, kot je predlagano v novem osnutku Evrokoda 8 (CEN, 2019) in v standardu ANS 2.26 (American Nuclear Society et al., 2004). Podoben pristop je bil uporabljen tudi pri projektiranju stavb na osnovi potresnega tveganja (Lazar Sinković et al., 2016). V teh primerih je treba izvesti analizo potresne ranljivosti konstrukcije, ki se že pogosto uporablja za oceno potresne zmogljivosti stavb (Salzano et al., 2003; Phan et al., 2016), ne pa tudi za jeklene rezervoarje s plavajočo streho.

Opisanega kompleksnega problema ni možno rešiti v okviru ene doktorske disertacije. Zato je bilo izbranih več podproblemov, ki so bili nato obravnavani v disertaciji. V prvem delu je bila raziskava usmerjena v preučevanje potresnega odziva dvignjenih rezervoarjev za hranjenje tekočine. Obravnavan je obstoječ dvignjeni rezervoar, ki je bil poškodovan med potresom v Izmitu, ter njegova različica, ki je bila projektirana po obstoječih standardih. Rezultati študije omogočajo primerjavo potresnega odziva rezervoarjev, v kolikor je ta ovrednoten s konvencionalnimi merami potresne zmogljivosti objekta ali z merami potresnega tveganja. V tej fazi študije so bili uporabljeni poenostavljeni modeli rezervoarjev, vpliv plavajoče strehe pa je bil zanemarjen.

Naslednji korak raziskave je bil namenjen preučevanju potresnega odziva rezervoarjev s plavajočimi strehami. Z uporabo metode končnih elementov sta bila razvita podroben numerični model in poenostavljen numerični model, ki sta bila validirana z odzivom plavajoče strehe rezervoarja med testom na potresni mizi, ki je bil izvedeni v okviru projekta INDUSE-2-SAFETY (CEA, 2017). Poenostavljen model jeklenega rezervoarja za hranjenje tekočine, ki upoštevajo učinke plavajoče strehe, je bil nato uporabljeni še za raziskovanje potresne ranljivosti in potresnega tveganja jeklenih rezervoarjev, opremljenih s plavajočo streho.

Z omenjenimi raziskavami smo preverjali naslednji hipotezi:

– Potresni odziv rezervoarjev s plavajočo streho je mogoče z zadostno natančnostjo simulirati z uporabo poenostavljenega modela, ki upošteva učinke dinamične interakcije strehe in vsebine rezervoarja ter učinke vsebine na sam rezervoar.

– Trenutni sistemi plavajočih streh ne zagotavljajo zadostne potresne varnosti pred izgubo vsebine zaradi poškodb strehe, saj se pojavljajo poškodbe kot so potopitev strehe zaradi razpok na krovu ali velikih pomikov, uklon plavajoče strehe zaradi učinkov teorije drugega reda.

Prva hipoteza je bila preizkušena s poenostavljenim modelom in podrobnim numeričnim modelom rezervoarja, ki je bil preizkušen na potresni mizi. V poglavju 3 je predstavljen poenostavljeni model plavajoče strehe in rezervoarja. Za poenostavljeni model jeklenega rezervoarja je bil uporabljen že razpoložljivi linijski model, ki ga sestavljajo koncentrirane mase in konzole s katerimi simuliramo impulzivne in konvekcijske komponente odziva vsebine rezervoarja. Model je bil uporabljen za simulacijo impulzivnega odziva tekočine v rezervoarju, dinamično obnašanje plavajoče strehe pa je bilo ocenjeno na podlagi analitičnega modela, ki je podrobno predstavljen v poglavju 3. Slednji temelji na Hamiltonovem variacijskim principu ob upoštevanju učinkov teorije drugega reda (Shabani & Golzar, 2012). Poenostavljeni model je bil validiran z uporabo podrobnega numeričnega modela, ki je bil razvit v programu Abaqus (Dassault Systemes, 2019). Podroben model upošteva vpliv trenja med dnom in potresno mizo, dinamično viskoznost tekočine, interakcijo jeklo-tekočina in z enačbo stanja, odvisnost tlakom, temperaturo in prostornino tekočine. Natančnost obeh numeričnih modelov za simulacijo odziva plavajoče strehe je bila potrjena na osnovi eksperimentalnih rezultatov (poglavje 4) (CEA, 2017).

Druga hipoteza je bila preizkušena z analizami potresnega tveganja (poglavje 5 in 6), vendar so bile najprej preučevane različne mere za oceno potresne zmogljivosti konstrukcij (poglavje 2). Za oceno potresne ranljivosti in zmogljivosti izbranih rezervoarjev s plavajočo streho je bil uporabljen le poenostavljeni model.

Poleg opisanih hipotez so bili v temi doktorske disertacije predvideni naslednji rezultati in izvirni prispevki k znanosti:

1. Razvoj poenostavljenega modela rezervoarjev za hranjenje tekočine, ki upošteva vpliv plavajoče strehe. Model mora omogočati izvedbo številnih simulacij, ki so potrebne za oceno tveganja.

2. Izboljšano znanje o potresni zmogljivosti rezervoarjev za tekočine s poudarkom na numeričnem modeliranju interakcije med površino tekočine in plavajočo streho ter z validacijo modela na osnovi eksperimentalnih rezultatov.

3. Preučeni bodo načini porušitve plavajoče strehe in podani predlogi za ustrezna mejna stanja.

4. Predlagana bo metoda za analizo potresne ranljivosti in tveganja rezervoarjev za tekočine s plavajočo streho.

5. Ocenjena bo potresna varnost obstoječih sistemov plavajoče strehe.

Točki 1) in 2) sta naslovljeni v poglavjih 3 in 4. Poglavje 3 obravnava poenostavljeni model rezervoarja, ki je nadalje preverjen v poglavju 4. Poleg tega je v poglavju 4 predstavljen in preverjen tudi podroben numerični model rezervoarja.

Poglavje 5 obravnava glavne vzroke za izlitje vsebine iz jeklenih rezervoarjev. Neprimerna plavajoča streha je eden izmed najnevarnejših vzrokov za izlitje oziroma prelitje tekočine, na kar se osredotoča tudi doktorska disertacija. Nato je analiziran dejanski jekleni rezervoar s plavajočo streho z enojno ploščo in pontonom na robu strehe. Poleg opisa konstrukcije, poglavje 5 vsebuje razpravo o opredelitvi ustreznega mejnega stanja. Upošteva se prelitje tekočine preko roba stene in, na približen način, tudi izlitje zaradi pretrga stene rezervoarja. S tem pristopom je naslovljena točka 3) predvidenih rezultatov disertacije. Definirano mejno stanje se nato uporabi v nadaljnjih analizah.

V poglavju 5 in nato še v poglavju 6 sta naslovljeni točki 4) in 5) predvidenih rezultatov. V zadnjem delu poglavja 5 je podrobneje obravnavana analiza ranljivosti jeklene stene rezervoarja in plavajoče strehe, kjer je poseben trud vložen v raziskavo o praktičnosti poenostavljenega modela rezervoarja. V poglavju 6 je predstavljen primer jeklenega rezervoarja s plavajočo streho, za katerega sta potresna zmogljivost in varnost ocenjena s konvencionalnimi kazalniki potresne zmogljivosti objektov ter z dvema kazalnikoma potresnega tveganja. Poleg tega je v poglavju 6 predstavljena enostavna, vendar na tveganju osnovana strategija za zmanjšanje tveganja za prelitje tekočine iz rezervoarja.

8.2 Vrednotenje mer potresne zmogljivosti na primeru jeklenih rezervoarjev

V prikazanem primeru je bila preučena potresna zmogljivost dejanskega dvignjenega rezervoarja, ki ni skladen s standardom Evrokod 8 in se je porušil med potresom v provinci Kocaeli, ter njegove različice, ki je skladna z veljavnim standardom Evrokod 8. Raziskava se osredotoča le na potresno obnašanje podporne konstrukcije pri mejnem stanju blizu porušitve, ki je, v obravnavanem primeru, kritična. Zato lahko na opažanja in zaključke raziskave delno vplivata opredelitev mejnih stanj in pripadajoče ciljne verjetnosti prekoračitve, katere določitev je trenutno tema razprav (npr. (CEN, 2019)).

Rezultati raziskave so pokazali, da je potresna nosilnost podporne konstrukcije dvignjenega rezervoarja, ki je neskladen s standardi, nesprejemljiva ne glede na uporabljen odločitveni model za preverjanje potresne zmogljivosti. Tak izid je nakazal na nujno potrebo po zamenjavi podobnih konstrukcij, ki prav tako ne ustrezajo standardu.

Za rezervoar, ki je skladen s standardi, je ocenjeni potresni odziv sprejemljiv, razen v primeru polnega rezervoarja in ob uporabi odločitvenega modela na osnovi tveganja pri pogoju potresnega scenarija. V tem primeru je bila verjetnost prekoračitve mejnega stanja blizu porušitve nekoliko večja kot ciljna verjetnost. Slednje je lahko posledica relativno enostavne ocene verjetnosti prekoračitve mejnega stanja blizu porušitve ob pogoju izbrane intenzitete gibanja tal. V kolikor bi bila ta verjetnost ocenjena iz funkcije ranljivosti, bi bilo potresno tveganje za obravnavan rezervoar, ki je skladen s standardi, prav tako sprejemljivo.

Primerjava rezultatov vseh treh odločitvenih modelov je za rezervoar, ki je skladen s standardi, pokazala, da konvencionalni odločitveni model ni najbolj primeren. Delež med potresno zahtvo in kapaciteto (D/C) je bil precej manjši od ena, kar, glede na konvencionalni odločitveni model, nakazuje na predimenzionirano podporno konstrukcijo. Rezultati ocene tveganja so pokazali, da je obravnavana konstrukcija spremenljiva, vendar je bila ocenjena verjetnost porušitve rezervoarja, ki je skladen s standardi, le nekoliko nižja od ciljne vrednosti, ki znaša 1% v 50 letih. Odločitveni modeli na osnovi potresnega tveganja so splošnejši, vendar so računsko zahtevnejši in zato terjajo uporabo poenostavljenih nelinearnih modelov.

8.3 Poenostavljeni model za simulacijo potresnega odziva plavajoče strehe rezervoarjev

Poenostavljeni model za potresno analizo plavajoče strehe sta predhodno predlagala Shabani & Golzar, (2012). Avtorja sta splošno nelinearno enačbo gibanja povezanega sistema plavajoče strehe in tekočine izpeljala v skladu s Hamiltonovim variacijskim principom, ki upošteva vpliv konservativnih sil. Za opis plavajoče strehe in Lagrangev opis tekočine so bile narejene naslednje predpostavke:

- dno in stene rezervoarja se toge,
- predpostavi se, da je tekočina neviskozna, nestisljiva in irotacijska,
- zibanje togega rezervoarja ni mogoče,
- upošteva se popoln stik med tekočino in streho,
- plavajoča streha se obravnava kot linearno elastična.

Posledično, Lagrangev opis problema privzame naslednjo obliko (glej En. (4) v disertaciji):

$$\int_{t_1}^{t_2} L\, dt = \int_{t_1}^{t_2} (T - U + F)\, dt$$

kjer so T kinetična energija plavajoče strehe, U deformacijska energija plavajoče strehe in F Lagrangev opis tekočine. Z iskanjem minimuma enačbe En. (4) dobimo splošno enačbo gibanja En. (38):

$$\boldsymbol{M}\ddot{\boldsymbol{B}} + \boldsymbol{K}\boldsymbol{B} + \boldsymbol{\chi}\boldsymbol{B}^{\mathbf{3}} = \rho\boldsymbol{G}\ddot{x}_g$$

kjer sta M in K:

$$\boldsymbol{M} = \boldsymbol{P} + \rho\boldsymbol{T}\boldsymbol{S}^{-\mathbf{1}}\boldsymbol{T}^{\boldsymbol{t}}$$

$$\boldsymbol{K} = \boldsymbol{Q} + \rho g\boldsymbol{U}$$

Spremenljivke v enačbah so bolj podrobno pojasnjene v disertaciji. Ker je bil pri izpeljavi enačb uporabljen Hamiltonov variacijski princip, se učinek nekonservativnih sil ne upošteva v splošni nelinearni enačbi gibanja (En. (38)). To pomanjkljivost se lahko odpravi z upoštevanjem učinka viskoznega dušenja z Rayleighevim modelom dušenja (Shabani, 2013). Posledično je matrika dušenja $\boldsymbol{C}$ (En. (41)) definirana kot linearna kombinacija matrik $\boldsymbol{M}$ in $\boldsymbol{K}$:

$$\boldsymbol{C} = \alpha\boldsymbol{M} + \beta\boldsymbol{K}$$

kjer se koeficienta α in β določita v skladu z Rayleighevim modelom dušenja in uporabo koeficienta dušenja ζ. Enačba (38) se torej lahko izrazi kot:

$$\boldsymbol{M}\ddot{\boldsymbol{B}} + \boldsymbol{C}\dot{\boldsymbol{B}} + \boldsymbol{K}\boldsymbol{B} + \chi\boldsymbol{B}^{3} = \rho\boldsymbol{G}\ddot{x}_g$$

Enačba (42) je diferencialna enačba gibanja, ki se lahko uporabi za simulacijo potresnega obnašanja plavajoče strehe v posplošenih koordinatah $\boldsymbol{B}$.

Enačba (42) je bila vgrajena v programsko orodje, ki je bilo pripravljeno v Matlabu (MathWorks, 2012) in je bilo uporabljeno za določitev vertikalnih pomikov plavajoče strehe pri potresni obtežbi. Podrobnejše informacije o matematične ozadju programskega orodja so predstavljene v poglavje 3.

8.4 Validacija poenostavljenega modela s podrobnim numeričnim modelom in preizkusom na potresni mizi

Predstavljen je eksperiment na potresni mizi, ki je vključeval jekleni rezervoar s plavajočo streho v pomanjšanem merilu (CEA, 2017). Med eksperimentom je bil merjen tudi vertikalni pomik plavajoče strehe, kar je bilo v okviru doktorske disertacije naknadno obdelano in analizirano. Izmerjeni pomiki so bili simulirani s podrobnim numeričnim modelom, ki je bil v ta namen razvit. V nadaljevanju so izmerjeni pomiki uporabljeni za validacijo poenostavljenega modela in podrobnega numeričnega modela rezervoarja plavajočo streho. Na poenostavljenem modelu rezervoarja je dodatno izvedena parametrična študija, z namenom določitve najvplivnejših parametrov.

Podroben tridimenzionalni model jeklenega rezervoarja s plavajočo streho v pomanjšanem merilu je bil z metodo končnih elementov razvit v programu Abaqus. Kot alternativni pristop je bil razvit tudi poenostavljen numerični model, ki omogoča računsko učinkovito simulacijo časovnega odziva plavajoče strehe. Kljub temu, da je analiza podrobnega modela podala natančne rezultate, je računsko zelo zamudna, modeliranje pa izjemno zahtevno. Po drugi strani je poenostavljeni model zahteval posebno pozornost pri določanju vhodnih podatkov, zlasti zaradi obodnega obroča, ki lahko vpliva na dinamiko vertikalnega pomika plavajoče strehe. Kljub temu sta tako podrobni kot poenostavljeni numerični model zagotovila precej podobne časovne odzive vertikalnega pomika strehe na robu stene rezervoarja. Pri podrobnem numeričnem modelu je bilo opaziti le rahlo odstopanje med dnom plavajoče strehe in površino vsebine rezervoarja. Slednje je za preiskovani rezervoar pravzaprav potrdilo predpostavko poenostavljenega modela o popolnem stiku med dnom plavajoče strehe in površino tekočine.

Iz preizkusa na potresni mizi je bilo razvidno, da že sorazmerno šibko premikanje tal povzroči prelivanje tekočine iz rezervoarja. Ta pojav sta primerno simulirala tako podrobni kot poenostavljeni numerični model, zaradi česar je poenostavljeni model atraktiven za študije potresnega tveganja, ki upoštevajo naključne potresne zapise.

Kljub temu, da se rezultati obeh modelov ujemajo z eksperimentalnimi rezultati, so za nadaljnjo validacijo predlaganih modelov in boljše razumevanje omejitev in potresne učinkovitosti plavajočih streh potrebne dodatne raziskave tako z eksperimenti kot tudi z bolj podrobnimi numeričnimi modeli. Poleg tega so potrebne dodatne raziskave s katerimi bi bolj podrobno validirali območje poenostavljenega modela za analizo vertikalnih pomikov plavajočih streh pri potresni obtežbi. Z enostavno parametrično študijo je bil že pokazan velik vpliv parametra γ na največje vertikalne pomike plavajoče strehe, predvsem v primerjavi z drugimi opazovanimi parametri. Spreminjanje Youngovega modula plavajoče strehe je imelo zanemarljiv vpliv na največje vertikalne pomike, vpliv pa ni zanemarljiv v analizi lastnega nihanja. Ugotovljeno je bilo, da je lahko poenostavljena enačba v zaključeni obliki za največji vertikalni pomik dovolj natančna, vendar je treba to ugotovitev potrditi s časovno analizo odziva plavajočih streh za mnogo različnih potresnih zapisov in različnih primerov rezervoarjev s plavajočimi strehami.

8.5 Analiza potresne ranljivosti jeklenega rezervoarja s plavajočo streho

Pričujoče poglavje obravnava oceno potresne ranljivosti rezervoarja s plavajočo streho z upoštevanjem prelivanje tekočine in pojava slonove noge. Za ta namen so bili uporabljeni poenostavljeni in podrobni numerični modeli, ki simulirajo časovni odziv plavajoče strehe in stene rezervoarja pri gibanju tal. Izkazalo se je, da je poenostavljeni model, ki je osnovan na Hamiltonovem variacijskem principu, računsko učinkovit. Za poenostavljen model je bilo pokazano, da predpostavka o preprečitvi zibanja in popolnega stika med streho in tekočino nista kritični za obravnavam rezervoar s plavajočo streho.

Predstavljen poenostavljeni model ima določene prednosti pred podrobnim numeričnim modelom, v kolikor je cilj simulacije usmerjen v preučevanje izgub vsebine rezervoarja zaradi prelivanja tekočine. Velikost poenostavljenega modela je skupaj z rezultati analize časovnega odziva velikostnega reda nekaj megabajtov, kar je občutno manj kot pri podrobnem numeričnem modelu, kjer govorimo o gigabajtih podatkov. Poleg tega je poenostavljeni model računsko zelo učinkovit in natančen pri napovedi največjega vertikalnega pomika, ki je ključni inženirski parameter potresnih zahtev na osnovi katerega se definira mejno stanje prelivanja. Posledično je bil poenostavljeni model zlasti primeren za analizo ranljivosti, saj se lahko vertikalni odziv izračuna v nekaj minutah in ne urah, kot v primeru podrobnega numeričnega modela. Končno pa za poenostavljeni model ni potrebno zaganjati licenčne programske opreme, saj ga lahko razvijemo v odprtokodnem programu, na primer v Pythonu (Van Rossum & Drake Jr, 1995).

Poenostavljeni model, ki je bil uporabljen za analizo sten rezervoarja, je bil razvit na osnovi raziskav (Malhotra et al., 2000). Sposobnost dviga in zdrsa pa je bila upoštevana v skladu s predhodno razvitimi modeli, npr. Malhotra & Veletsos, (1994), Vathi & Karamanos, (2017) ali Phan & Paolacci, (2018).

Posebna pozornost je bila posvečena izbiri potresnih zapisov za oceno občutljivosti vertikalnega pomika plavajoče strehe. Spektralni pospešek pri T = 4 s je bil izbran kot mera za intenziteto gibanja tal pri analizi tveganja, saj analiza potresne nevarnosti ni bila izvedena za spektralne pospeške pri nihajnih časih, ki so daljši od 4 s, kar je posledica omejitev modelov gibanja tal. Najbolj primerna mera za intenziteto gibanja tal za napoved odziva tekočine in plavajoče strehe je spektralni pospešek pri prvem nihajnem času konvekcijskega gibanja T_C, ki je običajno velikostnega reda od 5 s do 15 s.

Za nadaljnjo poenostavitev ocene ranljivosti za prelivanje tekočine je bil uveden alternativni pristop, ki temelji na enostavni Evrokodovi formuli za določitev največjega dviga tekočine na prosti površini. Alternativni pristop je za večino potresnih zapisov podal zelo dobre ocene največjega vertikalnega pomika plavajoče strehe. Za nekaj potresnih zapisov z določenim frekvenčnim sestavom, pa je alternativni pristop podcenil zahtevo potresa, saj Evrokodova enačba zanemari vpliv višjih konvekcijskih oblik nihanja tekočine in plavajoče strehe.

Izkazalo se je, da je opazovani jekleni rezervoar bistveno manj ranljiv na uklon v obliki slonove noge kot na prelivanje vsebine rezervoarja. Tudi primerjava mediane pospeška, ki povzroči prekoračitev mejnega stanja, pokaže, da do uklona pride pri višjih spektralnih pospeških kot so pospeški, ki povzročijo prelivanje vsebine rezervoarja. Prenehanje zadrževanja vsebine zaradi prelivanja tekočine je v tem primeru torej bolj kritično kot odpoved stene rezervoarja kot posledica uklona stene. Uporabljena mera za intenziteto gibanja tal se je pokazala za bolj učinkovito pri oceni ranljivosti rezervoarja na pojav slonove noge, saj standardna deviacija logaritemskih vrednosti mejnih pospeškov znaša približno 0.1, medtem ko pripadajoča standardna deviacija za mejno stanje prelivanje tekočine preko roba rezervoarja znaša med približno 0.4 in 0.5.

8.6 Ocena potresne zmogljivosti jeklenega rezervoarja s plavajočo streho

Poglavje obravnava oceno potresne zmogljivosti dejanskega jeklenega rezervoarja s plavajočo streho z upoštevanjem izgube vsebine zaradi prelivanja preko stene rezervoarja, kar je posledica prekomernega vertikalnega pomika strehe, in z upoštevanjem odpovedi stene rezervoarja zaradi uklona. Zaradi manjšega števila potrebnih simulacij se je ocena potresne zmogljivosti na osnovi konvencionalnega pristopa projektiranja izkazala praktično uporabna, vendar necelovita. Na osnovi ugotovitev, ki izhajajo iz konvencionalnega postopka projektiranja, je moč sklepati, da je prosti rob rezervoarja predimenzioniran, saj je razmerje med potresno zahtevo in kapaciteto (D/C) nizek.

Poleg tega je bilo pokazano, da je D/C zanemarljivo majhen, če je bil nivo polnjenja nižji od 90%. Odpoved stene rezervoarja je prav tako malo verjetna, saj je bil pripadajoč D/C izredno nizek tudi v primeru najvišjega nivoja polnjenja.

Odločitveni model na osnovi tveganja pri pogoju izbranega potresnega scenarija, ki upošteva verjetnost prekoračitve mejnega stanja glede na projektno intenziteto gibanja tal, je nakazal, da bi bil lahko zaključek glede potresne zmogljivosti obravnavanega rezervoarja drugačen od zaključka, ki izhaja iz konvencionalnega projektiranja. Verjetnost prelivanja z uporabo Evrokodove enačbe je znašala 14%, kar je več od 10%, kar je dovoljena vrednost za primer, ko projektni potres ustreza povratni dobi 2475 let. Ob uporabi poenostavljenega modela pa je bila verjetnost prelivanja zgolj 5%. Takšen izid je lahko posledica izračuna verjetnosti preseganja mejnega stanja zaradi omejenega števila uporabljenih akcelerogramov. V primeru nižjih nivojev polnjenja je bila potresna zmogljivost sprejemljiva pri obeh obravnavanih pristopih ne glede na izbrano mejno stanje. Pri nobeni analizi časovnega odziva pa ni bilo preseženo mejno stanje, ki je povezano z odpovedjo stene rezervoarja (slika 66).

Pri oceni potresne tveganja za prelivanje vsebine rezervoarja se je izkazalo, da je bilo ocenjeno tveganje podobno, če je bil uporabljen poenostavljen numerični model ali pa Evrokodova formula, ne glede na nivo polnjenja. Verjetnost prelivanja ($P_{f,\ LS,\ 50}$) 90% polnega rezervoarja je pri obeh pristopih znašalo približno 1% v dobi 50 let, kar morda ni sprejemljivo za vse deležnike, ki so izpostavljeni tveganju, četudi je nekoliko nižje od največje dovoljene vrednosti. V primeru prenehanja zadrževanja vsebine zaradi odpovedi stene rezervoarja je verjetnost porušitve v dobi 50 let za en red velikosti nižja. Odločitvena modela, ki temeljita na tveganju in pogojnem tveganju, sta, kljub nekaterim pomembnim razlikam, oba ovrgla predpostavko, da je prosti rob rezervoarja precej predimenzioniran, kot je nakazoval konvencionalni odločitveni model v primeru verifikacije prelivanja. Vsi trije odločitveni modeli so pokazali, da ima jekleni rezervoar zadovoljiv potresni odziv glede odpovedi stene rezervoarja zaradi uklona.

Izkazalo se je, da je potresno tveganje mogoče zmanjšati z upoštevanjem sprememb nivoja polnjenja tekom leta, saj rezervoarji niso ves čas polni. Tveganje se je tako zmanjšalo za približno 30% za primer prelivanja in 20% za odpoved stene rezervoarja. Zadovoljiv potresni odziv stene rezervoarja v tej študiji ni presenetljiv ker obravnavamo širok rezervoar (premer znaša 86 m), kjer je verjetnost zibanja zelo majhna, poleg tega pa je stena rezervoarja precej debela (43 mm).

Znižanje tveganja, ki je posledica nihanja nivoja polnjenja v referenčnem obdobju, lahko predstavlja ključni vidik pri zmanjševanju tveganja s preprostim sprejetjem strategije za zmanjševanje tveganja, ki predvideva omejitev nivoja polnjenja, v kolikor je ta mogoča. Na osnovi rezultatov, ki upoštevajo verjetnost različnih nivojev polnjenja, lahko potresni odziv izbranega primera označimo kot zadovoljiv, ne glede na uporabljen pristop za določitev pomika, mejnega stanja in odločitvenega modela.

8.7 Zaključki

V okviru preučevanja treh mer potresne zmogljivosti objektov (poglavje 2) je bilo ugotovljeno, da je poenostavljeni nelinearni model zagotovil enak potresni odziv obstoječega dvignjenega rezervoarja med potresom Kocaeli. Namreč, skoraj poln rezervoar, ki ni skladen s standardom Evrokod 8, se je porušil, medtem ko je skoraj prazen rezervoar ostal praktično nepoškodovan. Takšna opazovanja so zagotovila zaupanje v poenostavljene nelinearne modele rezervoarjev.

Na osnovi ocene potresne zmogljivosti dvignjenih rezervoarjev je bilo ugotovljeno, da je potresna zmogljivost dvignjenega rezervoarja, ki ni skladen z Evrokod 8, nesprejemljivo, potresna zmogljivost njegove različice, ki je skladna s standardom, pa je sprejemljiva za dve izmed treh preučevanih mer potresne zmogljivosti. V primeru polnega rezervoarja, ki je skladen s standardom, z upoštevanjem tveganja pri pogoju potresnega scenarija, se je izkazalo, da potresna zmogljivost rezervoarja ni sprejemljiva. Takšen izid je lahko posledica izračuna verjetnosti preseganja mejnega stanja zaradi omejenega števila uporabljenih akcelerogramov. Če je bila verjetnost preseganja mejnega stanja dobljena iz funkcije potresne ranljivosti, je bila zmogljivost rezervoarja, ki ustreza standardu Evrokod 8, prav tako zadovoljiva. Takšni zaključki niso presenetljivi, vendar se kaže precejšnja razlika med uporabljenimi odločitvenimi modeli, saj je izkoriščenost projektiranja v smislu med potresno zahtevo in kapaciteto zelo različna glede na uporabljen odločitveni model. Na osnovi konvencionalnega projektiranja je bilo moč zaključiti, da je konstrukcija predimenzionirana, kar pa ni moč trditi z uporabo odločitvenih modelov na osnovi tveganja. Zato je izbira mer za oceno potresne zmogljivosti in pripadajočih odločitvenih modelov pomembna. Mere potresnega tveganja so bolj splošne, vendar zahtevajo številne simulacije potresnega odziva konstrukcije.

Ker so pri oceni potresne zmogljivosti na podlagi tveganj potrebne številne simulacije potresnega odziva objekta, je bilo precej truda vloženega v razvoj programa za potresno analizo plavajoče strehe rezervoarja z uporabo poenostavljenega modela (poglavje 3). Poenostavljeni model temelji na Hamiltonovem variacijskem principu in potrebuje kar nekaj pozorno izbranih vhodnih podatkov. Model, ki je bil sprogramiran v okolje Matlab, je tako primeren za analizo potresnega odziva. Pred uporabo je bil model validiran s pomočjo eksperimentalnih rezultatov in analize po metodi končnih elementov podrobnega numeričnega modela. Poenostavljen model in program sta bila preverjena s podrobnim numeričnim modelom in z uporabo meritev, ki so bile opravljene v okviru eksperimenta na potresni mizi. Pokazano je bilo, da sta tako poenostavljeni model kot podrobni numerični model sposobna simulirati časovni odziv vertikalnega pomika strehe iz preiskave na potresni mizi. Podrobni model je bolj zanesljiv, a hkrati časovno potraten, zato je poenostavljeni model bolj primeren za oceno tveganja. V okviru parametrične študije je bilo ugotovljeno, da ima razmerje med višino tekočine in premerom rezervoarja največji vpliv na vertikalni pomik tekočine. Pokazano pa je bilo tudi, da je Evrokodova enačba za določitev največjih vertikalnih pomikov gladine proste tekočine dovolj natančna za oceno povprečne vrednosti največjih vertikalnih pomikov plavajoče strehe.

V 5. poglavju je bila izvedena ocena potresne ranljivosti dejanskega jeklenega rezervoarja, opremljenega z enojno plavajočo streho. Analizirana je bila ranljivost za prelivanje tekočine preko stene rezervoarja in na približen način tudi za odpoved stene rezervoarja zaradi uklona. Prvo mejno stanje je bilo analizirano s predhodno razvitim poenostavljenim modelom in Evrokodovo enačbo za največji vertikalni premik tekočine na prosti površini. Oba pristopa sta podala podobne rezultate, ki nakazujejo na precejšno potresno ranljivost za prelivanje tekočine preko roba stene rezervoarja.. Evrokodova enačba je podala višje vrednosti mediane mere za intenziteto pri prekoračitvi izbranega mejnega stanja kot poenostavljeni model, vendar razlike niso velike in znašajo med 7%, 11% in 17% za nivoje polnjenja 90%, 80% in 70%. Z uporabo Evrokodove enačbe se je povečala tudi standarda deviacija mejnih pospeškov za približno 20%, ne glede na nivo polnjenja. Poleg tega se je Evrokodov pristop izkazal kot zelo občutljiv na frekvenčni sestav nekaterih gibanj tal. Pri nekaterih zapisih je bil največji vertikalni pomik tekočine podcenjen. Do tega je prišlo, ker Evrokodova enačba pri določanju pomika upošteva le vpliv prve nihajne oblike. Za večino potresnih zapisov ta predpostavka nudi zadovoljivo natančnost, do razlik pa lahko pride v primerih, ko višje nihajne oblike vplivajo na rezultat. Analize ranljivosti stene rezervoarja so bile izvedene z linijskim modelom rezervoarja, ki lahko simulira tudi dvig in zdrs. Za obravnavam primer se je pokazalo, da uklon stene rezervoarja ni kritičen, in sicer zaradi velikega premera samega jeklenega rezervoarja in precejšnje debeline stene (okoli 4 cm).

V poglavju 6 so mere potresne zmogljivosti iz poglavja 2 uporabljene za oceno potresne zmogljivosti dejanskega rezervoarja (poglavje 5) in sicer za primer prelivanja vsebine in odpovedi stene rezervoarja. Konvencionalni pristop je pokazal, da je prelivanje preko stene rezervoarja bolj kritično, vendar je bilo moč zaključiti, da je potresna zmogljivost napram prelivanju vsebine preko stene rezervoarja sprejemljiva. Tudi pri največjih nivojih polnjenja rezervoarja, je bilo razmerje med potresno zahtevo in kapaciteto (D/C) manjše od ena. Pri analizi plavajoče strehe s poenostavljenim modelom je D/C znašal 68%, pri uporabi Evrokodove enačbe pa 63%, kar je majhna razlika. Največja vrednost D/C za odpoved stene rezervoarja je znašala le 15%, kar je daleč od največje dovoljene vrednosti.

Odločitveni model na osnovi sprejemljive verjetnosti za odpoved funkcije, pri pogoju potresnega scenarija (tj. določene vrednosti mere za gibanje tal), je ravno tako pokazal, da je prelivanje vsebine verjetneje kot odpoved stene, vendar je bila v tem primeru potresna zmogljivost nezadovoljiva, če je bila verjetnost prekoračitve mejnega stanja pri izbrani vrednosti mere za gibanje tal določena z uporabo Evrokodove enačbe. Verjetnost prelivanja z uporabo Evrokodove enačbe je znašala 14%, kar je več od 10%, kar je dovoljena vrednost za primer, ko projektni potres ustreza povratni dobi 2475 let. Ob uporabi poenostavljenega modela pa je bila verjetnost prelivanja zgolj 5%. Za steno rezervoarja v nobenem primeru ni prišlo do prekoračitve mejnega stanja.

Tudi ocena tveganja za izbrano dobo 50 let je pokazala, da je plavajoča streha bolj izpostavljena kot stena rezervoarja. Verjetnost prelivanja vsebine je bila za največji nivo polnjenja skoraj 1% v dobi 50 let in sicer v primeru ocene pomika s poenostavljenim modelom ali z Evrokodovo enačbo. Ocenjena verjetnost uklona stene rezervoarja pa je znašala le 0.06% v dobi 50 let. Na podlagi teh rezultatov se potresni odziv obravnavanega primera ne more upoštevati kot sprejemljiv z vidika prelivanja vsebine. Z vidika odpovedi stene rezervoarja pa je odziv sprejemljiv, saj je verjetnost prekoračitve mejnega stanja bistveno nižja od dovoljene. Pri oceni potresnega tveganja se je izkazalo, da je treba pri oceni tveganja upoštevati tudi vpliv spreminjanja nivoja polnjenja rezervoarja tekom enega leta, saj na ta način tveganje zmanjša za približno 30%.

Uvedena metodologija za oceno potresnega tveganja z upoštevanjem vpliva letne spremembe polnjenja rezervoarja je tudi učinkovito orodje za obvladovanje tveganja za izgube zadrževanja tekočine, če se uporabi za določitev sprejemljive stopnje napolnjenosti rezervoarjev ob upoštevanju ciljnega tveganja.

BIBLIOGRAPHY

Abrahamson, N.A., Silva, W.J. 1997. Empirical response spectral attenuation relations for shallow crustal earthquakes. Seismological Research Letters 68, 1: 94–109.

Akkar, S., Sandikkaya, M. a., Şenyurt, M., Azari Sisi, A., Ay, B.O., Traversa, P., Douglas, J., Cotton, F., Luzi, L., Hernandez, B., Godey, S. 2014. Reference database for seismic ground-motion in Europe (RESORCE). Bulletin Of Earthquake Engineering 12, 1: 311–339.

Alessandri, S., Caputo, A.C., Corritore, D., Giannini, R., Paolacci, F., Phan, H.N. 2018. Probabilistic risk analysis of process plants under seismic loading based on Monte Carlo simulations. Journal Of Loss Prevention In The Process Industries 53, December 2017: 136–148.

American Nuclear Society, Committee, S., ANS-2.26, W.G. 2004.

American Petroleum Institute. 2012.

Ancheta, T.D., Darragh, R.B., Stewart, J.P., Seyhan, E., Silva, W.J., Chiou, B.S.J., Wooddell, K.E., Graves, R.W., Kottke, A.R., Boore, D.M., Kishida, T., Donahue, J.L. 2014. NGA-West2 database. Earthquake Spectra 30, 3: 989–1005.

De Angelis, M., Giannini, R., Paolacci, F. 2010. Experimental investigation on the seismic response of a steel liquid storage tank equipped with floating roof by shaking table tests. Earthquake Engineering And Structural Dynamics 39: 377–396.

Antonioni, G., Spadoni, G., Cozzani, V. 2007. A methodology for the quantitative risk assessment of major accidents triggered by seismic events. Journal Of Hazardous Materials 147, 1–2: 48–59.

ASCE 7-10 .ASCE/SEI 7-10. Minimum Design Loads for Buildings and Other Structures. American Society of Civil Engineers.

ASCE 43-05 .ASCE/SEI 43-05. Seismic Design Criteria for Structures, Systems, and Components in Nuclear Facilities. American Society of Civil Engineers.

Atkinson, G.M., Boore, D.M. 2003. Empirical ground-motion relations for subduction-zone earthquakes and their application to Cascadia and other regions. Bulletin Of The Seismological Society Of America 93, 4: 1703–1729.

Bakalis, K. 2017. Seismic risk assessment of liquid storage tanks via a nonlinear surrogate model. , December 2016: 2851–2868.

Bakalis, K., Fragiadakis, M., Vamvatsikos, D. 2017. Surrogate Modeling for the Seismic Performance

Assessment of Liquid Storage Tanks. Journal Of Structural Engineering 143, 4: 04016199.

Bakalis, K., Vamvatsikos, D. 2018. Seismic Vulnerability Assessment for Liquid Storage. : 1–10.

Baker, J.W. 2010. Conditional Mean Spectrum: Tool for Ground-Motion Selection. Journal Of Structural Engineering 137, 3: 322–331.

Baker, J.W. 2015. Efficient Analytical Fragility Function Fitting Using Dynamic Structural Analysis. Earthquake Spectra 31, 1: 579–599.

Baker, J.W., Cornell, C.A. 2005. A vector-valued ground motion intensity measure consisting of spectral acceleration and epsilon. Earthquake Engineering And Structural Dynamics 34, 10: 1193–1217.

Bentz, E.C. 2000. Sectional analysis of reinforced concrete members. : 316.

Bernier, C., Padgett, J.E. 2019. Buckling of aboveground storage tanks subjected to storm surge and wave loads. Engineering Structures 197, July 2018: 109388.

Boore, D.M., Bommer, J.J. 2005. Processing of strong-motion accelerograms: needs, options and consequences. Soil Dynamics And Earthquake Engineering 25, 2: 93–115.

Buratti, N., Tavano, M. 2013. Dynamic buckling and seismic fragility of anchored steel tanks by the added mass method. Earthquake Engineering And Structural Dynamics.

Campbell, K.W., Bozorgnia, Y. 2008. NGA ground motion model for the geometric mean horizontal component of PGA, PGV, PGD and 5% damped linear elastic response spectra for periods ranging from 0.01 to 10 s. Earthquake Spectra 24, 1: 139–171.

CEA. 2017. Component Fragility Evaluation, Seismic Safety Assessment And Design Of Petrochemical Plants Under Design-Basis And Beyond-Design-Basis Accident Conditions (INDUSE-2-SAFETY). Commissariat a L'energie Atomique et Aux Energies Alternatives. Saclay, France

Celano, F., Dolšek, M. 2021. Fatality risk estimation for industrialized urban areas considering multi-hazard domino effects triggered by earthquakes. Reliability Engineering And System Safety 206, October 2020.

CEN. 2019, EN 1998-1-1. CEN/TC 250/SC 8 Eurocode 8: - Design of structures for earthquake resistance — Part 1-1: General rules and seismic action. Brussels, European Committee for Standardisation.

CEN. 2004a, EN 1992-1-1:2004 Eurocode 2: Design of concrete structures - Part 1-1: General rules and rules for buildings. Brussels, European Committee for Standardisation.

CEN. 2004, EN 1998–1:2004 Eurocode 8: Design of structures for earthquake resistance - Part 1: General rules, seismic actions and rules for buildings. Brussels, European Committee for Standardisation.

CEN. 2005, EN 1998–3:2005 Eurocode 8: Design of structures for earthquake resistance - Part 3: Assessment and retrofitting of buildings. Brussels, European Committee for Standardisation.

CEN. 2006, EN 1998-4 Eurocode 8 - Design of structures for earthquake resistance - Part 4: Silos, tanks and pipelines.

Chiou, B., Darragh, R., Gregor, N., Silva, W. 2008. NGA project strong-motion database. Earthquake Spectra 24, 1: 23–44.

Chiou, B.S.-J., Youngs, R.R. 2008. An NGA Model for the average horizontal component of peak ground motion and response spectra. Earthquake Spectra 24, 1: 173–215.

Constantinescu, A., Alaoui, A.E.M., Nême, A., Jacques, N., Rigo, P. 2011. Numerical and experimental studies of simple geometries in slamming. International Journal Of Offshore And Polar Engineering 21, 3: 216–224.

Corritore, D., Alessandri, S., Giannini, R., Paolacci, F. 2017. PRIAMUS : A new tool for the probabilistic risk assessment with Monte Carlo simulations of Process Plants under Seismic Loading PRIAMUS : A new tool for the probabilistic risk assessment with Monte Carlo simulations of Process Plants under Seismic Loading. , November: 19–20.

Cozzani, V., Salzano, E. 2004. The quantitative assessment of domino effects caused by overpressure: Part I. Probit models. Journal Of Hazardous Materials 107, 3: 67–80.

Crittenden, J.C., Trussell, R.R., Hand, D.W., Howe, K.J., Tchobanoglous, G. 2012. MWH's Water Treatment: Principles and Design: Third Edition.

Crowley, H., Polidoro, B., Pinho, R., Van Elk, J. 2017. Framework for developing fragility and consequence models for local personal risk. Earthquake Spectra 33, 4: 1325–1345.

Crowley, H., Silva, V., Martins, L. 2018. Seismic Design Code Calibration Based on Individual and Societal Risk. V: 16th European Conference on Earthquake Engineering. Thessaloniki, Greece: 173–222 pp.

CSI. 2011. SAP2000 Integrated Software for Structural Analysis and Design.

Cutnell, J.D., Johnson, K.W. 2009. Physics. 8. izd. JOHN WILEY & SONS, I. (ur.), . Danvers, MA

Dassault Systemes. 2019.

Dolšek, M., Brozovič, M. 2016. Seismic response analysis using characteristic ground motion records for risk-based decision-making (3R method). Earthquake Engineering & Structural Dynamics 45, 3: 401–420.

Dormand, J.R., Prince, P.J. 1986. A reconsideration of some embedded Runge-Kutta formulae. Journal Of Computational And Applied Mathematics 15, 2: 203–211.

Dorogoy, A., Rittel, D., Brill, A. 2011. Experimentation and modeling of inclined ballistic impact in thick polycarbonate plates. International Journal Of Impact Engineering 38, 10: 804–814.

El-Samanody, A.P.M., Ghorab, A., Noaman, A.S. 2016. Design and Study of Floating Roofs for Oil Storage Tanks. 4, 4: 1–12.

Elwood, K.J., Moehle, J.P. 2005. Axial capacity model for shear-damaged columns. ACI Structural Journal 102, 4: 578–587.

Fabbrocino, G., Iervolino, I., Orlando, F., Salzano, E. 2005. Quantitative risk analysis of oil storage facilities in seismic areas. Journal Of Hazardous Materials 123, 1–3: 61–69.

Fan, H., Wang, Z., Yan, K. 2018. Buckling of Tanks With a Conical Roof Under Harmonic Settlement. : V01BT01A020.

Filippou, F.C., Popov, E.P., Bertero, V. V. 1983. Effects of Bond Deterioration on Hysteretic Behavior of Reinforced Concrete Joints. Report EERC 83-19. Earthquake Engineering Research Center, University of California, Berkeley:

Girgin, S. 2011. The natech events during the 17 August 1999 Kocaeli earthquake: Aftermath and lessons learned. Natural Hazards And Earth System Science 11, 4: 1129–1140.

Google Earth. 2020. Priolo Gargallo, Sicily, Italy.https://www.google.com/maps/@37.15786,15.1837,6701m/data=!3m1!1e3

Goudarzi, M.A. 2015. Seismic Design of a Double Deck Floating Roof Type Used for Liquid Storage Tanks. Journal Of Pressure Vessel Technology, Transactions Of The ASME 137, 4: 1–7.

Hatayama, K., Zama, S., Nishi, H., Yamada, M., Hirokawa, Y. 2004. Long-period Strong Ground Motion and Damage to Oil Storage Tanks Due to the 2003 Tokachi-oki Earthquak. Journal Of The Seismological Society Of Japan 57: 83–103.

Hosseini, M., Soroor, A., Sardar, A., Jafarieh, F. 2011. A simplified method for seismic analysis of tanks with floating roof by using finite element method: Case study of Kharg (Southern Iran) island tanks. Procedia Engineering 14: 2884–2890.

Huston, R., Josephs, H. 2008. Practical stress analysis in engineering design, third edition. Practical Stress Analysis In Engineering Design, Third Edition: 1–635.

Iervolino, I., Galasso, C., Cosenza, E. 2010. REXEL: computer aided record selection for code-based seismic structural analysis. Bulletin Of Earthquake Engineering 8, 2: 339–362.

Iervolino, I., Maddaloni, G., Cosenza, E. 2009. A note on selection of time-histories for seismic analysis of bridges in Eurocode 8. Journal Of Earthquake Engineering 13, 8: 1125–1152.

Itao, K., Crandall, S.H. 1979. Natural Modes and Natural Frequencies of Uniform, Circular, Free-Edge Plates. Journal Of Applied Mechanics 46, June 1979: 448–453.

Jalayer, F., Cornell, C.A. 2009. Alternative non-linear demand estimation methods for probability-based seismic assessments. Earthquake Engineering & Structural Dynamics 38, 8: 951–972.

Jankovic, S., Stojadinovic, B. 2004. Probabilistic Performance-Based Seismic Demand Model For R/C Frame Buildings. 13th World Conference On Earthquake Engineering , 2120.

Jayaram, N., Lin, T., Baker, J.W. 2011. A computationally efficient ground-motion selection algorithm for matching a target response spectrum mean and variance. Earthquake Spectra 27, 3: 797–815.

Kalemi, B., Caputo, A.C., Paolacci, F. 2019. Resilience calculation of process plants under seismic loading: A case study. American Society Of Mechanical Engineers, Pressure Vessels And Piping Division (Publication) PVP 5: 1–10.

Karagiannakis, G., Wenzel, M., Kowalczyk, P., Farhan, M. 2020. Seismic Risk and Resilience Assessment of Industrial Facilities : Seismic Risk and Resilience Assessment of Industrial Facilities : Case Study on a Black Carbon Plant. V: 17th World Conference on Earthquake Engineering. Sendai, Japan

Kazantzi, A.K., Vamvatsikos, D. 2015. Intensity measure selection for vulnerability studies of building classes. International Association For Earthquake Engineering 44, 15 July: 2677–2694.

Kokoska, S., Zwillinger, D. 2000. Standard Probability and Statistics Tables and Formulae. CRC Press (ur.), .

Kozak, A., Cacciatore, P.J., Gustafsson, L.M. 2010. Seismic response of floating roof liquid storage tanks part II. Contact pressure approach. V: ASME 2010 Pressure Vessels & Piping Division / K-PVP Conference. Bellevue, Washington, USA

Krausmann, E., Cruz, A.M., Salzano, E. 2017. Natech Risk Assessment and Management: Reducing the Risk of Natural-Hazard Impact on Hazardous Installations. Elsevier:

Ktenidou, O.-J., Abrahamson, N.A., Darragh, R.B., Silva, W.J. 2016. A Methodology for the Estimation of Kappa from Large Datasets : Example Application to Rock Sites in the NGA-East Database and Implications on Design Motions. PEER Report No. 2016/01 , April 2016.

Kummari, S.R., Prueter, P.E., Bifano, M.F.P. 2018. Evaluating Large Aboveground Storage Tanks Subject to Seismic Loading: Part II — Explicit Dynamic Analysis With Liquid Sloshing Effects. : V008T08A010.

Lanzano, G., Santucci de Magistris, F., Fabbrocino, G., Salzano, E. 2015. Seismic damage to pipelines in the framework of Na-Tech risk assessment. Journal Of Loss Prevention In The Process Industries 33: 159–172.

Lazar, N., Dolšek, M. 2014. Incorporating intensity bounds for assessing the seismic safety of structures: Does it matter? Earthquake Engineering & Structural Dynamics 43, 5: 717–738.

Lazar Sinković, N., Brozovič, M., Dolšek, M. 2016. Risk-based seismic design for collapse safety. Earthquake Engineering & Structural Dynamics 45, 9: 1451–1471.

Lazar Sinković, N., Dolšek, M. 2020. Fatality risk and its application to the seismic performance assessment of a building. Engineering Structures 205, April 2019.

Lindell, M.K., Perry, R.W. 1996. Identifying and managing conjoint threats: Earthquake-induced hazardous materials releases in the US. Journal Of Hazardous Materials 50, 1: 31–46.

Luco, N., Ellingwood, B.R., Hamburger, R.O., Hooper, J.D., Kimball, J.K., Kircher, C.A. 2007. Risk-targeted versus current seismic design maps for the conterminous United States. V: SEAOC 2007 Convention proceedings. Squaw Creek, California, USA, 27-28 September2007: 1–13 pp.

Malhotra, P.K. 1995. Base uplifting analysis of flexibly supported liquid-storage tanks. Earthquake Engineering & Structural Dynamics 24, 12: 1591–1607.

Malhotra, P.K., Veletsos, A.S. 1994. Uplifting Response Of Unancored Liquid-Storage Tanks. Journal Of S 120, 12: 3525–3547.

Malhotra, P.K., Wenk, T., Wieland, M. 2000. Simple procedure for seismic analysis of liquid-storage tanks. Structural Engineering International: Journal Of The International Association For Bridge

And Structural Engineering (IABSE) 10, 3: 197–201.

Manos, G.C., Clough, R.A.Y.W. 1985. Tank Damage During The May 1983 Coalinga Earthquake. 13, October 1984: 449–466.

MathWorks. 2012. MATLAB the Language of Technical Computing.

Matsui, T. 2007. Sloshing in a Cylindrical Liquid Storage Tank With a Floating Roof Under Seismic Excitation. Journal Of Pressure Vessel Technology 129, 4: 557.

Matsui, T. 2017. Sloshing in a Cylindrical Liquid Storage Tank With a Single-Deck Type Floating Roof Under Seismic Excitation. Journal Of Structural And Construction Engineering (Transactions Of AIJ) 71, 607: 101–108.

McGuire, R.K. 2004. Seismic Hazard And Risk Analysis. Earthquake Engineering Research Institute (ur.), . Oakland

McKenna, F., Fenves, G.L. 2010. Open System for Earthquake Engineering Simulation (OpenSees). Pacific Earthquake Engineering Research Center: http://opensees.berkeley.edu

Morita, H., Takata, T., Madokoro, H., Sago, H., Murakami, H., Yokoi, S., Yamamoto, T. 2018. Study On The Predictive Evaluation Method Of Nonlinear Sloshing Wave Height Of Cylindrical Tanks (Part 1 : Shaking Table Test Results And Verification Results Of Analytical Method For Nonlinear Sloshing). : 1–8.

Nishi, H., Yamada, M., Zama, S., Hatayama, K., Sekine, K. 2008. Experimental Study on the Sloshing Behavior of the Floating Roof using a Real Tank. Journal Of High Pressure Institute Of Japan 46, 1: 4–17.

NIST. 1995. A study of the performance of petroleum storage tanks during earthquakes, 1993-1995. National Institute of Standard and Technology. Gaithersburg, Maryland

OpenSees. 2017. MultiLinear Material. Pacific Earthquake Engineering Research Center: http://opensees.berkeley.edu/wiki/index.php/MultiLinear_Material

Özmen, B. 2000. Isoseismal Map , Human Casualty And Building Damage Statistics Of The Izmit Earthquake Of August 17, 1999. V: Third Japan-Turkey Workshop on Earthquake Engineering. : 1–11 pp.

Pantusheva, M. 2017. Seismic Analysis of Steel Storage Tanks: Overview of Design Codes Used in Practice. International Jubilee Scientific Conference “75th Anniversary Of UACEG” UNIVERSITY OF ARCHITECTURE, CIVIL ENGINEERING AND GEODESY i, November:

15.

Paolacci, F., Corritore, D., Caputo, A.C., Bursi, O.S., Kalemi, B. 2018a. A Probabilistic Approach for the Assessment of LOC Events in Steel Storage Tanks Under Seismic Loading.: 1–7 pp.

Paolacci, F., Corritore, D., Caputo, A.C., Bursi, O.S., Kalemi, B. 2018b.

Paolacci, F., Reza, M.S., Bursi, O.S. 2011. Seismic analysis and component design of refinery piping systems. V: COMPDYN 2011, 3rd ECCOMAS Thematic Conference on Computational Methods in Structural Dynamics and Earthquake Engineering. Corfu, Greece

Petersen, M.D., Harmsen, S.C., Jaiswal, K.S., Rukstales, K.S., Luco, N., Haller, K.M., Mueller, C.S., Shumway, A.M. 2018. Seismic hazard, risk, and design for south america. Bulletin Of The Seismological Society Of America 108, 2: 781–800.

Phan, H.N., Paolacci, F. 2016. Efficient Intensity Measures For Probabilistic Seismic Response Analysis Of Anchored Above-Ground Liquid Steel Storage Tanks. V: ASME 2016 Pressure Vessels and Piping Conference. Vancouver, British Columbia, Canada: 1–10 pp.

Phan, H.N., Paolacci, F. 2018. Fluid-Structure Interaction Problems: an Application To Anchored and Unanchored Steel Storage Tanks Subjected To Seismic Loadings. European Conference On Earthquake Engineering: 1–10.

Phan, H.N., Paolacci, F., Alessandri, S. 2016. Fragility Analysis Methods for Steel Storage Tanks in Seismic Prone Areas. Volume 8: Seismic Engineering 00032, July: V008T08A023.

Phan, H.N., Paolacci, F., Bursi, O.S., Tondini, N. 2017. Seismic fragility analysis of elevated steel storage tanks supported by reinforced concrete columns. Journal Of Loss Prevention In The Process Industries 47: 57–65.

Razzaghi, M.S., Eshghi, S. 2004. Behavior Of Steel Oil Tanks Due To Near-Fault Ground Motion. V: 13th World Conference on Earthquake Engineering. : 1–6 pp.

Van Rossum, G., Drake Jr, F.L. 1995. Python reference manual. Centrum voor Wiskunde en Informatica Amsterdam:

Sago, H., Morita, H., Takata, T., Madokoro, H., Murakami, H., Yokoi, S., Yamamoto, T. 2018. Study On The Predictive Evaluation Method Of Nonlinear Sloshing Wave Height Of Cylindrical Tanks (Part 2: Proposal And Examination Of Applicability Of The Predictive Evaluation Method). : 1–8.

Sakai, F., Nishimura, M., Ogawa, H. 1984. Sloshing behavior of floating-roof oil storage tanks.

Computers And Structures 19, 1–2: 183–192.

Salzano, E., Iervolino, I., Fabbrocino, G. 2003. Seismic risk of atmospheric storage tanks in the framework of quantitative risk analysis. Journal Of Loss Prevention In The Process Industries 16, 5: 403–409.

Scott, B.D., Park, R., Priestley, M.J.N. 1982. Stress-Strain Behavior of Concrete Confined by Overlapping Hoops at Low and High Strain Rates. ACI Journal Proceedings 79, 1.

Šebenik, Ž., Dolšek, M. 2016. Strong ground motion database. Ljubljana, University of Ljubljana, Faculty of Civil and Geodetic Engineering, IKPIR:

Setzler, E.J., Sezen, H. 2008. Model for the lateral behavior of reinforced concrete columns including shear deformations. Earthquake Spectra 24, 2: 493–511.

Sezen, H., Whittaker, A.S. 2006. Seismic Performance of Industrial Facilities Affected by the 1999 Turkey Earthquake. Journal Of Performance Of Constructed Facilities 20, 1: 28–36.

Shabani, R. 2013. Stress Patterns in Single Deck Floating Roofs Subjected to Ground Motion Accelerations. International Journal Of Engineering J 26, 12: 1495–1504.

Shabani, R., Golzar, F.G. 2012. Large deflection analysis of floating roofs subjected to earthquake ground motions. Nonlinear Analysis: Real World Applications 13, 5: 2034–2048.

Shampine, L.F., Reichelt, M.W. 1998. The Matlab ODE Suite. SIAM Journal On Scientific Computing 18, 1: 1–22.

Sivý, M., Musil, M., Chlebo, O., Havelka, R. 2017. Sloshing effects in tanks containing liquid. MATEC Web Of Conferences 107: 1–7.

Taniguchi, T., Yoshida, Y., Hatayama, K. 2018. Applicability of the Simplified Analysis and Relevant Calculations to Evaluating Uplift Displacement of Unanchored Tanks. : V008T08A012.

Tornabene, F. 2012. Mechanics of Shell Structures in Composite Material. The Generalized Method of Differential Quadrature (in Italian). Società Editrice Esculapio:

Tsang, H.H., Daniell, J.E., Wenzel, F., Werner, A.C. 2018. A semi-probabilistic procedure for developing societal risk function. Natural Hazards 92, 2: 943–969.

Tsang, H.H., Wenzel, F. 2016. Setting structural safety requirement for controlling earthquake mortality risk. Safety Science 86: 174–183.

Vamvatsikos, D., Fragiadakis, M. 2010. Incremental dynamic analysis for estimating seismic performance sensitivity and uncertainty. Earthquake Engineering & Structural Dynamics 39, 2: 141–163.

Vathi, M., Karamanos, S.A. 2017. A simple and efficient model for seismic response and low-cycle fatigue assessment of uplifting liquid storage tanks. Journal Of Loss Prevention In The Process Industries 53: 29–44.

Vathi, M., Karamanos, S.A., Kapogiannis, I.A., Spiliopoulos, K. V. 2017. Performance Criteria for Liquid Storage Tanks and Piping Systems Subjected To Seismic Loading. Journal Of Pressure Vessel Technology: 1–12.

Virella, J.C., Godoy, L.A., Suárez, L.E. 2006. Dynamic buckling of anchored steel tanks subjected to horizontal earthquake excitation. Journal Of Constructional Steel Research 62, 6: 521–531.

Woessner, J., Laurentiu, D., Giardini, D., Crowley, H., Cotton, F., Grünthal, G., Valensise, G., Arvidsson, R., Basili, R., Demircioglu, M.B., Hiemer, S., Meletti, C., Musson, R.W., Rovida, A.N., Sesetyan, K., Stucchi, M. 2015. The 2013 European Seismic Hazard Model: key components and results. Bulletin Of Earthquake Engineering 13, 12: 3553–3596.

Yamauchi, Y., Kamei, A., Zama, S., Uchida, Y. 2006. Seismic design of floating roof of oil storage tanks under liquid sloshing. V: ASME Pressure Vessels and Piping Division Conference. Vancoucer, BC, Canada: 1–9 pp.

Young, S., Balluz, L., Malilay, J. 2004. Natural and technologic hazardous material releases during and after natural disasters: A review. Science Of The Total Environment 322, 1–3: 3–20.